The Relationship Between Active Galactic Nuclei and Metal-enriched Outflows in Galaxy Clusters

by

Charles Kirkpatrick

A thesis
presented to the University of Waterloo
in fulfillment of the
thesis requirement for the degree of
Doctor of Philosophy
in
Physics

Waterloo, Ontario, Canada, 2011

I hereby declare that I am the sole author of this thesis. This is a true copy of the thesis, including any required final revisions, as accepted by my examiners.

I understand that my thesis may be made electronically available to the public.

Abstract

Clusters of galaxies are host to powerful Active Galactic Nuclei (AGN) that greatly affect the thermal history of clusters. By keeping X-ray emitting gas from cooling, massive, run away star formation does not occur in the brightest cluster galaxy (BCG). This is achieved through radio jets displacing large quantities of metal-rich gas and carving out cavities in the intracluster medium (ICM). This metal-rich gas was originally formed within the BCG and ejected through type Ia supernovae. The current distribution of the ejecta suggests an extra source of energy has spread the material far out into the ICM. Currently, it is unclear what mechanisms are responsible. In this thesis, I present evidence, in the form of X-ray imaging and spectra, that establishes a link between AGN and the observed distribution of metal-rich gas.

First, the BCG in the Abell 1664 cluster is unusually blue and is forming stars at a rate of $\sim 23\ M_{\odot}\ \mathrm{yr}^{-1}$. The BCG is located within 5 kpc of the X-ray peak, where the cooling time of $3.5{\times}10^8$ yr and entropy of 10.4 keV cm^2 are consistent with other star-forming BCGs in cooling flow clusters. The cooling rate in this region is roughly consistent with the star formation rate, suggesting that the hot gas is condensing onto the BCG. We use the scaling relations of Bîrzan et al. (2008) to show that the AGN is underpowered compared to the central X-ray cooling luminosity by roughly a factor of three. We suggest that A1664 is experiencing rapid cooling and star formation during a low-state of an AGN feedback cycle that regulates the rates of cooling and star formation. Modeling the emission as a single temperature plasma, we find that the metallicity peaks 100 kpc from the X-ray center, resulting in a central metallicity dip. However, a multi-temperature cooling flow model improves the fit to the X-ray emission and is able to recover the expected, centrally-peaked metallicity profile.

Next, using deep *Chandra* observations of the Hydra A galaxy cluster, we examine the metallicity structure near the central galaxy and along its powerful radio source. We show that the metallicity of the ICM is enhanced by up to 0.2 dex along the radio jets and lobes compared to the metallicity of the undisturbed gas. The enhancements extend from a radius of 20 kpc from the central galaxy to a distance of $\sim$ 120 kpc. We estimate the total iron mass that has been transported out of the central galaxy to be between $2{\times}10^7$ $\mathrm{M}_{\odot}$ and $7{\times}10^7$ $\mathrm{M}_{\odot}$ which represents 10% - 30% of the iron mass within the central galaxy. The energy required to lift this gas is roughly 1% to 5% of the total energetic output of the AGN. Evidently, Hydra A's powerful radio source is able to redistribute metal-enriched, low entropy gas throughout the core of the galaxy cluster. The short re-enrichment timescale $< 10^9$ yr implies that the metals lost from the central galaxy will be quickly replenished.

Finally, we present an analysis of the spatial distribution of metal-rich gas in 29 galaxy clusters using deep observations from the *Chandra X-ray Observatory*. The BCGs have experienced recent active galactic nucleus activity in the forms of bright radio emission, cavities, and shock fronts embedded in the hot atmospheres. The heavy elements are distributed anisotropically and are aligned with the large-scale radio and cavity axes. They are apparently being transported from the halo of the BCG into the ICM along large-scale outflows driven by the radio jets. The radial ranges of the metal-enriched outflows are found to scale with jet power as $R_{\rm Fe} \propto P_{\rm jet}^{0.43}$, with a scatter of only 0.42 dex. The heavy elements are transported beyond the extent of the inner cavities in all clusters, suggesting this is a long lasting effect sustained over multiple generations of outbursts. Black holes in BCGs will likely have difficulty ejecting metal enriched gas beyond 1 Mpc unless their masses substantially exceed 10^9 $M_\odot$. It is likely however for these black holes to output enough energy to uplift all the peaked, metal-rich gas beyond the BCG to the currently observed widespread distribution.

Acknowledgements

I would like to thank my supervisor, Brian McNamara, for the support and guidance he has given me these last six years. I would also like to thank Michael Balogh and Mike Hudson for their role as thesis committee members and for all the after work conversations and beer.

Over the years I have had many great officemates to share in my experiences as a graduate student. A special thanks go out to Steve Allanson, Somali Basu, Ken Cavagnolo, Chad Greene, Mike Hillier, Farnoud Kazemzadeh, Ting Lu, Sean McGee, Helen Russell, Joel Vaughn, and Anton Wiranata. When I needed a break from work, I thank Dan, Gandhi, Jeff, Kevin, Michael, Mike, Ravi, and Steve for all the great times we had together.

None of this would have been possible without the support from my parents. I will never be able to stop thanking them for what they have done for me. To the rest of my family, Justin, Megan, Cameron, and especially Collum, thank you for the inspiration needed to finally get this thesis finished.

Dedication

I dedicate this thesis to my grandparents, Charles & Janice Kirkpatrick and Edward & Doris Ker.

Table of Contents

List of Tables

List of Figures

Chapter 1

Introduction

1.1 Galaxy Clusters

The observable Universe is made up of a complex hierarchical ladder of structures. A single star like our own Sun is the basic unit in this ladder. Thousands of stars make up a star cluster. Billions of stars make up a galaxy like the Milky Way. Galaxies also form into their own set of structures. A galaxy group is a gravitationally bound system of somewhere between 10 to 50 galaxies. Galaxy clusters are the largest gravitationally bound structures with up to thousands of galaxies. Red, elliptical galaxies are the most common variety of galaxy in a cluster, while spirals are more commonly found in the field (Sarazin, 1988). A rich cluster will normally host a dominant galaxy at the center, referred to as the brightest cluster galaxy (BCG). BCGs are massive ellipticals known to host some ongoing star formation.

Galaxies are far from the dominant component of a galaxy cluster. They are not even the most dominant form of baryonic matter. On average, only 3% of the total mass of a cluster is in the form of stars. The dominant baryonic component is in the form of a hot, diffuse plasma known as the intracluster medium (ICM). The ICM consists primarily of ionized hydrogen and accounts for approximately 16% of the total cluster mass. The rest of a cluster is composed of non-baryonic particles known as dark matter. We cannot directly observe dark matter, but its effects on baryonic matter during massive cluster mergers has proven its existence (Clowe et al., 2006).

A typical galaxy cluster has a mass of 10^{14} - 10^{15} $M_{\odot}$. The temperature of the ICM is determined by the depth of the potential well it occupies. Converting potential energy into

kinetic energy in a gravitational well of this size results in temperatures of approximately 10^7 K. At these temperatures, the ICM cooling mechanism is dominated by bremsstrahlung radiation above 1 keV, and line emission at cooler temperatures. The average density is 10^{-3} cm^{-3}, with the most dense regions reaching as much as 10^{-1} cm^{-3}. With a range in luminosity between 10^{43} - 10^{46} erg s^{-1}, galaxy clusters are the brightest X-ray sources in the sky after quasars (for a review, see Sarazin, 2003).

X-ray photons are impossible to observe on Earth. At those energies, the atmosphere is entirely opaque. In order to capture X-ray photons, we must use space telescopes such as the *Chandra X-ray Observatory*. Unlike optical telescopes, X-ray photons are collected at a much slower rate of around just a few to tens of counts per second. On board instruments include the Advanced CCD Imaging Spectrometer (ACIS) that allows for simultaneous acquiring of high-resolution imaging and spectra. With spectra, it is possible to constrain properties such as density and temperature. Imaging allows for the analysis of how the ICM is interacting with its surrounding environment.

What makes galaxy clusters interesting objects for study are the fact they are almost a perfect "closed box". Due to the massive gravitational potential, clusters hang on to all the material they acquire. The cooling times in the outskirts of a cluster are long enough that they will never drop out of hydrostatic equilibrium and form cold gas clouds, thus trapping in the thermal history of the cluster. This makes them perfect for studying the history of processes such as active galactic nuclei (AGN) and supernovae feedback, mergers, and gas stripping.

1.2 Cool Cores

In the center of some clusters, the cooling time is short enough for the hot plasma to cool and form gas clouds. The cool clouds would then sink to down into the potential starting an inflow of gas to the cluster center. This has been known as the cooling flow model (Fabian, 1994). A cooling flow cluster is associated with a massive BCG at the center of its potential well, a significant peak in X-ray emission and a decreasing inward temperature gradient. Due to the high density, ROSAT measurements predicted gas should be cooling out at rates of 100 - 1000 $M_\odot$ yr^{-1}. Observations of star formation rates and cold gas masses implied rates should be 1 - 10 $M_\odot$ yr^{-1} (McNamara, 1997; Edge, 2001). Coined "the cooling flow problem", later generations of X-ray telescopes, *Chanrda* and *XMM-Newton*, were unable to find the characteristic recombination lines expected to be present in condensing gas (Peterson et al., 2003; Peterson & Fabian, 2006).

The answer to this problem is the gas is being heated. Two leading mechanisms to balance cooling with heating are through conduction (Zakamska & Narayan, 2003; Voigt & Fabian, 2004) or AGN (Bîrzan et al., 2004; Dunn & Fabian, 2006; Rafferty et al., 2006, 2008). Evidence has since mounted in favor of AGN due to star formation and molecular gas being in better agreement with the new revised condensation rates (McNamara, 2002; Hicks & Mushotzky, 2005; Rafferty et al., 2006; O'Dea et al., 2008). Work done by Rafferty et al. (2008) demonstrates the cyclical nature of the process. Cooling increases the fuel supply to feed the SMBH that eventually heats the gas and stops cooling, which then cuts off the fuel supply and allows cooling to set in again. Though it appears cooling flows do exist, but not on the scale as originally predicted, the preferred nomenclature has changed to "cool core" clusters.

1.3 Active Galactic Nuclei

The actual process of depositing heat into the cores of rapidly cooling clusters comes in the form of the AGN physically carving out cavities in the ICM with associated shock fronts (for a review, see McNamara & Nulsen, 2007). The gravitational potential energy of the cool gas accreted onto the black hole is partially converted into kinetic energy. This forms a jet which radiates in radio wavebands through the process of synchrotron radiation. This radiation is closely related to the jet power (Bîrzan et al., 2008; Cavagnolo et al., 2010). The actual mechanical energy expended by a radio jet can be determined by the equilibrium pressure reached between itself and the ICM, and the volume of the cavities filled by relativistic particles (McNamara et al., 2000). The mechanical energy can range between 10^{55} - 10^{62} erg.

With large quantities of energy being dumped into the gas through radio jets, the ICM is in a constant state of turmoil. Clusters such as Perseus, M87, and Hydra A show multiple generations of cavities, suggesting that this process is periodic and long lasting. The cavities themselves may be rising by buoyant forces (Churazov et al., 2002), which work to directly entrain cold material allowing it to mix with hotter gas. The cooler and hotter gas in cool core clusters have different metallicities, which can act as a tracer of mixing. It has been shown that this mixing can have a significant effect on the chemical evolution of galaxy clusters (Rebusco et al., 2005, 2006; David & Nulsen, 2008; Simionescu et al., 2008, 2009; Kirkpatrick et al., 2009a; Kirkpatrick, McNamara & Cavagnolo, 2011).

1.4 Chemical Composition of the ICM

Cool core clusters differ in metallicity from non-cool core clusters. While all clusters on average are enriched to 1/3 solar, cool core cluster centers can be enriched up to and beyond the solar value (Allen & Fabian, 1998; Dupke & White, 2000; De Grandi & Molendi, 2001). This is due to the different processes involved with enriching the ICM. Supernovae (SNe) are responsible for creating and distributing most of all elements heavier than hydrogen and helium. SN II are what initially enriched the ICM to its average level (Mushotzky et al., 1996; Mushotzky & Loewenstein, 1997). This process is very rich in α-elements, but poor in iron. BCGs at the center of cool core clusters will contribute even more enriched material through SN Ia, a process rich in iron but poor in most α-elements. This creates a difference in chemical make between the inner and outer regions, plus an inward increasing metallicity gradient.

Because the abundance peak originates from the BCG, it is expected the abundance profile would follow the stellar light profile of the BCG, but the reality is the abundance profile is much more extended (Rebusco et al., 2005, 2006; David & Nulsen, 2008). A great source of energy is required to accomplish this large scale movement of material. Mechanisms such as mergers or AGN could potential provide the energy needed. The cyclic nature and ubiquity within cool core clusters make AGN the leading candidate for uplifting the material.

1.5 Goals of this Thesis

It is the goal of this thesis to explore the link between cluster metallicity and AGN activity, as well as the inherent properties of the gas involved. Only a few previous studies have studied this phenomenon for individual objects. This thesis intends to be a comprehensive study of a wide range of clusters and what trends emerge from a large sample. We do this through analysis of archival *Chandra* data, and optical and radio catalogues. We have assembled the most comprehensive sample of cluster metallicity maps and profiles. Clusters in this sample range in power between 10^{42} - 10^{46} erg s^{-1} over a redshift range of 0.0043 - 0.54. With this sample we will quantify the amount of mixing taking place in the ICM and correlate that with the output of the AGN.

A second project included in this thesis, which also informs the analysis procedures followed in the AGN mixing portion of the thesis, is a detailed study of the cool core cluster A1664. This multi-wavelength analysis covers topics such as whether the rate of cooling

and star formation are consistent with a standard cooling flow model. We also consider the effects multi-temperature gas has on the outcome of metallicity measurements and when its important to use single and multi-temperature spectral fitting models. Finally, we test the feasibility of whether in-falling galaxies can contribute significantly to the cold gas reservoir in the BCG.

Chapter 2 is our analysis of A1664. This chapter is based on previously published work in the Astrophysical Journal (ApJ) (Kirkpatrick et al., 2009b).

Chapter 3 is our analysis of Hydra A. Hydra A was the test case for the feasibility of the entire project. We successfully showed that the measurements can be performed to the degree of significance required to distinguish metal enhanced regions. This chapter is based on previously published work in ApJ Letters (Kirkpatrick et al., 2009a).

Chapter 4 is our initial analysis of a small subset of clusters on whether or not there is any relationship between the extent to which material can be uplifted and jet power. This chapter is based on previously published work in ApJ Letters (Kirkpatrick, McNamara & Cavagnolo, 2011).

Chapter 5 is the main body of this thesis where we analyze the entire sample as a whole and test the ultimate question, described above, of this dissertation. This chapter is comprised of work intended to be submitted to ApJ.

Chapter 6 is the concluding chapter of this thesis. Future work will also be discussed.

Chapter 2

Cooling, Feedback, and Star Formation in Abell 1664

2.1 Introduction

The fate of hundreds to thousands of solar masses per year of gas thought to be condensing out of the X-ray atmospheres of galaxy clusters is a problem that has puzzled astronomers for more than three decades (Fabian, 1994). New *Chandra* and XMM-*Newton* observations have recast the problem in terms that have significant consequences for understanding the formation of galaxies and super-massive black holes. First, high resolution spectra of the thermal emission from cooling flows failed to show the characteristic recombination lines from highly ionized metals in the condensing gas (for a review, see Peterson et al., 2003; Peterson & Fabian, 2006). The XMM-*Newton* observations did not rule out cooling altogether (eg., Sanders et al., 2008), but they were the first to show convincingly that the condensation rates must lie far below the levels predicted by pure cooling models. Second, images of cluster atmospheres revealed large-scale cavities and shock fronts associated with powerful AGN outbursts in central dominant galaxies (see McNamara & Nulsen, 2007, for a review). Measurements of cavity sizes and their surrounding pressures provide a convenient and reliable gauge of the mechanical pV work (energy) expended by radio jets as they inflated cavities against the surrounding gas pressure (McNamara et al., 2000). Assuming the cavities are driven to their current locations primarily by buoyant forces (eg., Churazov et al., 2002), the mean jet power is comparable on average to the power required to quench cooling in the cores of galaxies and clusters (Bîrzan et al., 2004; Dunn & Fabian, 2006; Rafferty et al., 2006). Apparently, the supermassive black holes located

in the nuclei of BCGs combined with abundant fuel accreting onto them provide a natural and powerful feedback mechanism that is energetically able to maintain most (but not all) of the cooling gas above a few keV (Brüggen & Kaiser, 2002; Reynolds et al., 2002; Dalla Vecchia et al., 2004; Ruszkowski et al., 2004a,b; Brüggen et al., 2005; Heinz et al., 2006; Vernaleo & Reynolds, 2006). Thus the failure of XMM-*Newton* to find strong cooling lines can be attributed largely to AGN feedback. How this jet power heats the gas and the extent to which other heating mechanisms such as thermal conduction, galaxy mergers, etc. are aiding it is poorly understood, and remains an outstanding issue (Zakamska & Narayan, 2003; Dolag et al., 2004; Voigt & Fabian, 2004; Dennis & Chandran, 2005; Poole et al., 2008).

Evidence for residual cooling can be inferred by the unusually high star formation rates and reservoirs of cold gas found in BCGs. Although this star formation is frequently attributed to stripping from the occasional gas-rich galaxy (eg., Holtzman et al., 1996), several surveys undertaken over the last few decades have tied the presence of nebular line emission, molecular gas, and star formation to cooling flows (Johnstone et al., 1987; McNamara & O'Connell, 1989; Crawford et al., 1995, 1999; Cardiel et al., 1998; Edge et al., 2002; Salomé & Combes, 2003; Rafferty et al., 2006; Donahue et al., 2007; Edwards et al., 2007; Bildfell et al., 2008; O'Dea et al., 2008; Rafferty et al., 2008). Despite these ties, the enormous gap between the cooling and star formation rates raised very serious issues. This situation again changed dramatically when XMM-*Newton*'s downward-revised condensation rates were shown to be in near agreement with the star formation rates in many, but not all, systems (McNamara, 2002; Hicks & Mushotzky, 2005; Rafferty et al., 2006; O'Dea et al., 2008).

Recently, evidence tying the cooling of hot halos to star formation was found by Rafferty et al. (2008), who showed that star formation ensues when the central cooling time falls below a remarkably sharp threshold value of $\sim 5{\times}10^8$ yr or equivalently a central entropy of 30 keV cm^2. This and two other criteria: the X-ray and galaxy centroids lie within ~ 20 kpc of each other, and the X-ray cooling luminosity exceeds the jet (cavity) power, appear to govern the onset of star formation in cooling flows. Cavagnolo et al. (2008) found a similar threshold for the onset of Hα and radio emission (see also Hu et al., 1985). The Hα threshold is certainly related to but not identical to the star formation threshold, as we show in this paper. These new results are difficult to understand in the context of mergers or stripping, but instead they tie the presence of star formation and AGN activity closely to cooling instabilities in the hot atmospheres (Rafferty et al., 2008; Voit et al., 2008; Soker, 2008).

These developments have broad implications for understanding the formation and evolution of galaxies. Outflows driven by gas accretion onto massive black holes may have

regulated the growth of bulges giving rise to the observed correlation between bulge mass and super-massive black hole mass in nearby galaxies (Ferrarese & Merritt, 2000; Gebhardt et al., 2000; Häring & Rix, 2004). In simulations, AGN feedback at late times in the so-called "radio mode," of which feedback in cooling flows is thought to be the archetype, is able to suppress cooling and star formation in the hot halos of giant elliptical galaxies and BCGs (Bower et al., 2006; Croton et al., 2006). This process may explain the turnover at the bright end of the galaxy luminosity function and the lack of bright blue galaxies expected in standard ΛCDM models. Cooling flows permit study of this process in detail.

Abell 1664 is a good candidate for studying star formation and cooling in galaxy cluster cores. It is a cooling flow cluster (Allen et al., 1995) located at redshift $z = 0.128$ (Allen et al., 1992) and has an Abell richness class of 2 (Abell et al., 1989). Based on ROSAT data, the X-ray luminosity in the 0.1-2.4 keV band is $4.1{\times}10^{44}$ erg s^{-1} (Allen et al., 1992). A1664 hosts a BCG known to be a very bright Hα emitter with a luminosity of at least $1.6{\times}10^{42}$ erg s^{-1}, and forming stars at a rate of 14-23 $M_{\odot}$ yr^{-1} (Wilman et al., 2006; O'Dea et al., 2008). In the X-ray waveband, the cluster is regular in shape on large scales. The core shows signs of a surface brightness break along the eastern edge at a radius of 30″ from the center and an elongated surface brightness peak at the center.

In this chapter, we present our analysis of the recent *Chandra* observations and deep U- and R-band images of the cluster and its core. Section 2.2 describes the data set and reduction process. In Section 2.3, we describe our analysis of the X-ray and optical data. In Section 2.4 we interpret the data. Finally, we summarize in Section 2.5. Throughout the paper we assume a ΛCDM cosmology with $H_0 = 70$ km s^{-1} Mpc^{-1}, $\Omega_M = 0.3$, and $\Omega_\Lambda = 0.7$. The angular scale is 2.29 kpc arcsec^{-1} at the redshift of the cluster. All uncertainties quoted are 90% confidence intervals.

2.2 Observations & Data Reduction

Abell 1664 was observed for 37 ks on 2006 December 4 (ObsID 7901) using the ACIS-S3 CCD on-board the *Chandra X-ray Observatory*. The focal plane temperature during the observation was kept at -120° C. CIAO version 3.4 was used for all data reduction and preparation with version 3.4 of the calibration database. Standard filtering was applied to eliminate background flares, producing a loss of 0.4 ks from the total exposure time. Point sources have been identified and removed using *wavedetect* and confirmed by eye. Time-dependent gain and charge transfer inefficiency corrections have been applied. Blank-sky background files used for background subtraction were normalized to the source image

count rate in the $9.5 - 12$ keV band. When extracting spectra from a region, a background spectrum is extracted from the equivalent region of the blank-sky background event file.

Optical images of the cluster's BCG were obtained with the Kitt Peak National Observatory's 4 m telescope on 1995 February 2 using the T2KB CCD camera. The seeing at the time was approximately $1.3''$. Images were taken through U and Gunn R filters with total exposure times of 2400 s and 800 s, respectively. These filters were chosen to avoid contamination by emission lines from [OII] 3272 and Hα 6563 at the redshift of the cluster. Additional imaging was done using an R-band filter that includes Hα emission with a total exposure time of 800 s. The individual images have the bias level subtracted and have been flat-fielded using twilight sky exposures. Finally, the images for each band were combined into single U and R images and color corrected for use in our analysis. An Hα+[NII] emission map was created by taking the scaled difference between the normalized R- and Gunn R-band images.

2.3 Data Analysis

In the following sections, we present our analysis of the *Chandra* observation of A1664. Our purpose is to obtain the mean properties of the cluster including the gas temperature, density, metallicity, cooling rate, and how these properties vary with radius.

2.3.1 Images

We present in Figure 2.1 the R-band DSS image of A1664. Overlaid are the X-ray contours spanning the entire ACIS-S3 CCD ($8' \times 8'$). On large scales, the X-ray emission is fairly regular, but with asymmetries to the south and east. The inner region is more complex. The cluster core image in the 0.4 - 7.0 keV band is presented in the upper left panel of Figure 2.2. A bar-like structure is shown as the dark region approximately $22.5'' \times 10''$ (52×23 kpc) in size associated with the BCG, marked A. To the east, a brightness edge, marked B, is seen at a radius of $30''$ from the cluster center. In the upper right panel of Figure 2.2, Hα emission is aligned with the "bar" region, though the bar is more extended than both the Hα and star forming region. The feature marked C is thought to be a disturbance created by a neighboring galaxy (Wilman et al., 2006). In the bottom left and right panels of Figure 2.2 we present the R- and U-band images, respectively. The R-band shows that the BCG's core does not share the same position angle on the sky as the outer envelope. In the U-band, there is more structure. There are two distinct clumps north

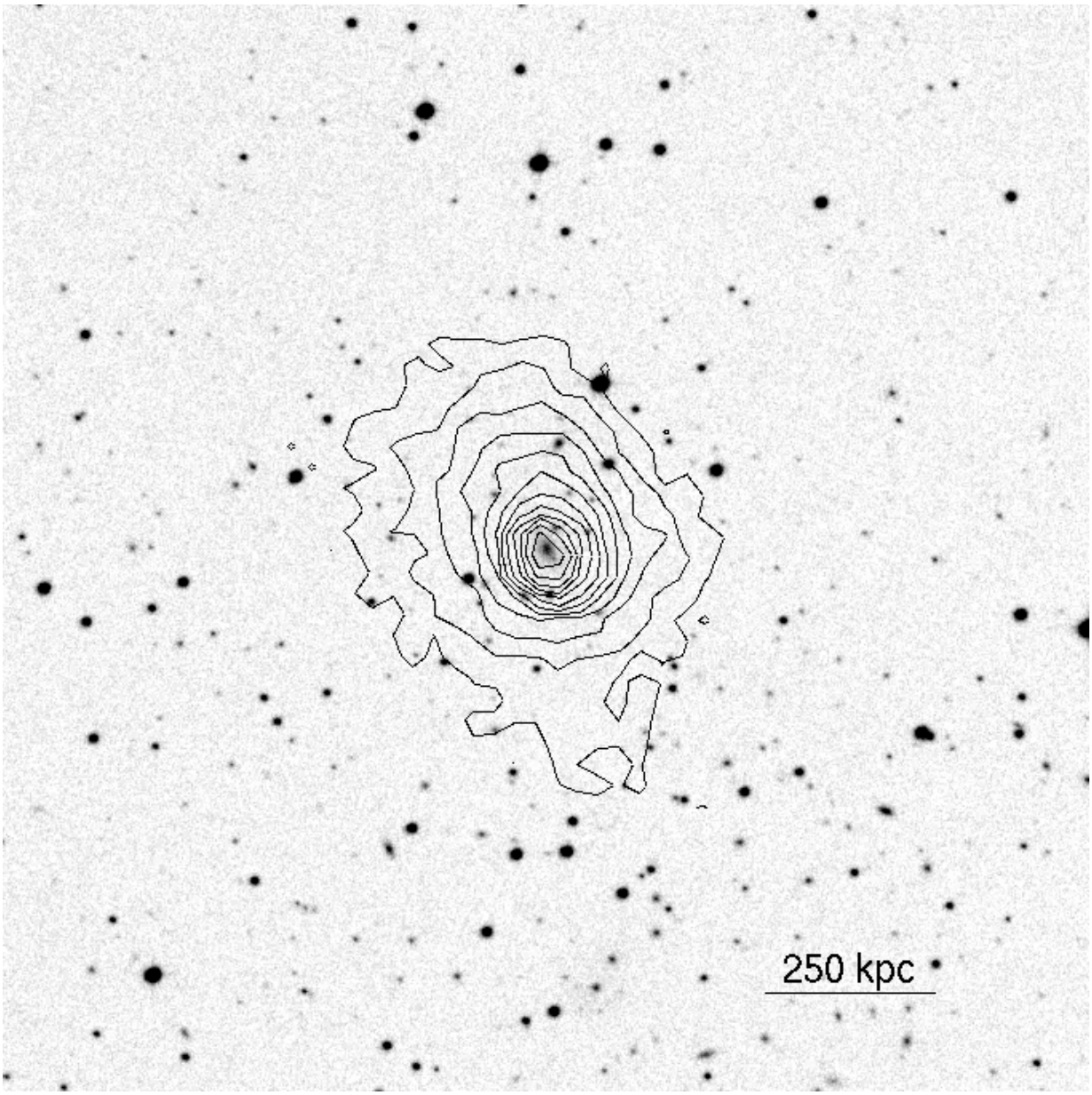

Figure 2.1: DSS R-band image of A1664. The X-ray contours show the emission spanning the entire ACIS-S3 chip. North is towards the top; East is towards the left.

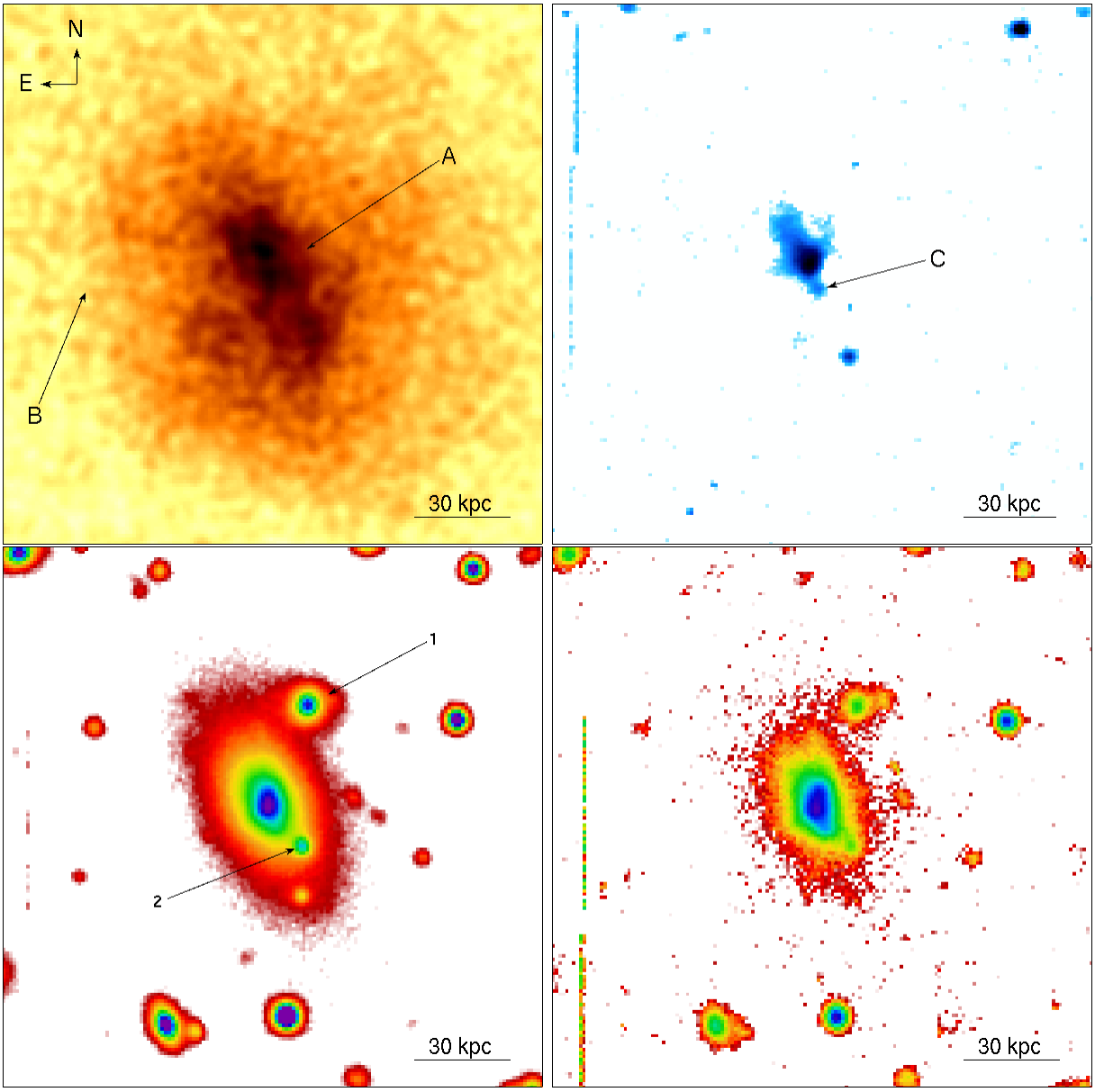

Figure 2.2: *Upper left*: Inner 74″×74″ region in the 0.4 - 7.0 keV band adaptively smooth using CIAO tool *aconvolve*. *Upper right*: Hα map of the same region. *Lower left*: R-band image of the same region in false color to show structural detail. *Lower right*: U-band image of the same region in false color. The labels are as follow: Point A is the X-ray bar, point B is the surface brightness edge, and point C is Hα disruption being caused by a neighboring galaxy. Points 1 and 2 are clusters members that may be interacting with the cD.

and south of the center. We will discuss possible origins of these features in the following sections.

2.3.2 Surface Brightness Analysis

We determined the center, ellipticity and position angle of A1664 on the sky by fitting a two-dimensional Lorentzian surface (Wise et al., 2004). The centroid is found at R.A. = $13^h03^m42^s.5$, DEC = $-24°14'43''.96$. This centroid is offset from the cluster emission peak by $3.6''$ to the NE. The average ellipticity was found to be 0.22 with a position angle of 25°. Both are consistent with values found by Allen et al. (1995). When dividing the data into annular regions for measuring radial trends, the centroid, ellipticity, and postion angle derived here were used.

An exposure map created using *mkexpmap* was divided into the image. The surface brightness was calculated by measuring the flux through annuli $5''$ in width. We fit the surface brightness profile with a beta model using the Sherpa model *beta1d*. A single beta model does not adequately fit the cluster surface brightness. The model adequately fits the outer regions of the profile, but not the elevated brightness of the core. Adding a second component to fit the cooling cusp improves the fit. The form for the double-beta model is

$$I(r) = I_1(1 + \frac{r^2}{r_1^2})^{-3\beta_1+\frac{1}{2}} + I_2(1 + \frac{r^2}{r_2^2})^{-3\beta_2+\frac{1}{2}} + I_B, \tag{2.1}$$

where I_i and r_i are the amplitudes and core radii. The constant compontent, I_B, was added to represent the background. All parameters from the fit can be found in Table 2.1. The surface brightness profile presented in Figure 2.3 includes the fit from the double-beta model. The smooth model does not fit the central region well, which is most likely due to the complicated structure of the core.

The residual map formed by subtracting the double-beta model is presented in Figure 2.4. A spiral pattern is apparent near the center. Similar spiral patterns have been seen in other clusters (Sanders & Fabian, 2002; Clarke et al., 2004). The spiral is commonly attributed to the angular momentum of stripped gas from galaxies or groups. Other explanations involve merging dark matter halos with trapped gas (Clarke et al., 2004; Dupke et al., 2007).

The spiral feature is common in systems with cold fronts (see Markevitch & Vikhlinin, 2007, for a review). Most cold fronts are likely due to oscillations of the dark matter or gas in the cluster core (Tittley & Henriksen, 2005). This "sloshing" can be triggered by a tidal or pressure disturbance caused by an infalling subcluster or possibly a powerful AGN

Table 2.1: Double beta-model fit for A1664.

Parameter	Value
$r_1{}^a$	$89.83^{+2.39}_{-2.36}$
β_1	$0.78^{+0.02}_{-0.02}$
$I_1{}^b$	$75.7^{+1.3}_{-1.4}$
$r_2{}^a$	$23.65^{+0.34}_{-0.36}$
β_2	$0.91^{+0.01}_{-0.01}$
$I_2{}^b$	1220^{+16}_{-17}
$I_B{}^b$	$6.93^{+0.09}_{-0.09}$
χ^2_{norm}	2.57
χ^2	228.48
$d.o.f.$	89

[a]Units of arc seconds.
[b]Units of 10^{-9} phot s^{-1} cm^{-2} $arcsec^{-2}$.

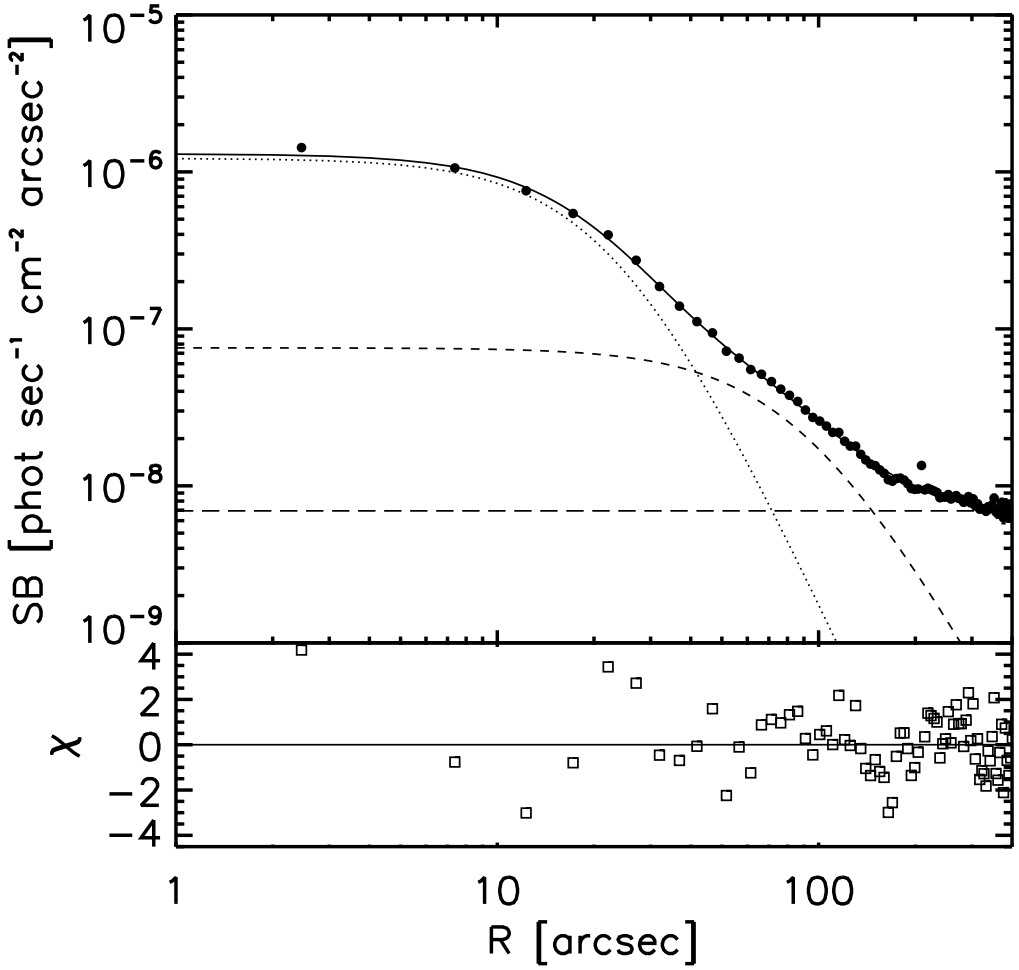

Figure 2.3: Radial surface brightness profile in the 0.4 - 7.0 keV band. The fit shown represents the two components of the double-beta model and the best fit background value. The panel below shows the residual deviation from the fit.

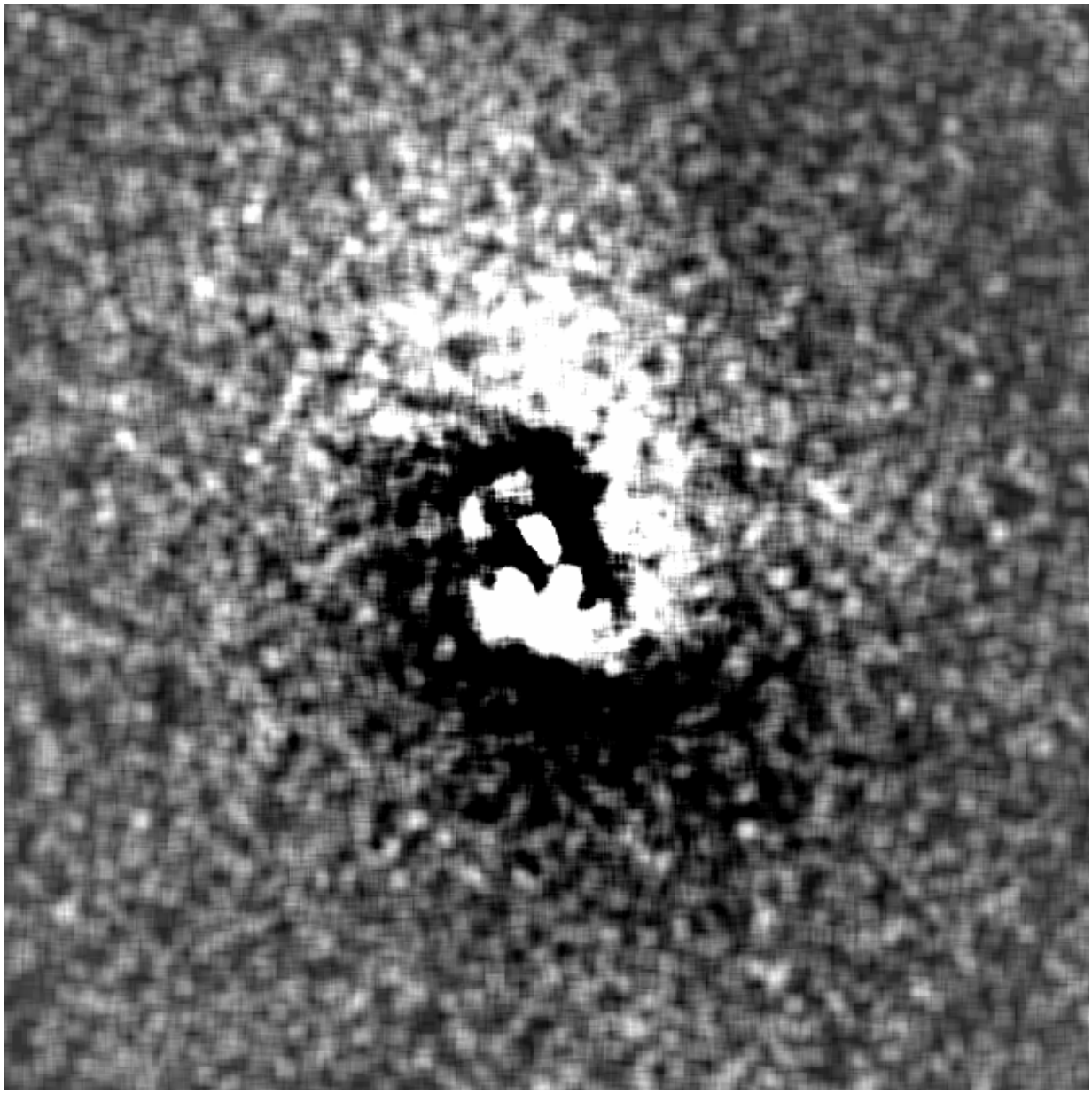

Figure 2.4: A $5' \times 5'$ residual map of the double-beta model subtracted image. The image was adaptively smooth using CIAO tool *aconvolve* and then subtracted.

outburst. The sloshing gas can acquire angular momentum, which is why the spiral feature is associated with many cold fronts (Ascasibar & Markevitch, 2006). We present evidence that A1664 contains a cold front in Section 2.3.6.

2.3.3 Integrated Spectral Analysis

For our spectral analysis, we begin by extracting the total spectrum of the cluster core using *dmextract*. The elliptical region used in the extraction was chosen with semi-major axis of 161″ to stay within the edge of the ACIS-S3 CCD's footprint. Weighted response files were created for the extracted regions using *mkacisrmf* and *mkwarf*. Four different models were used to fit the properties of the X-ray gas over the energy range 0.4 keV to 7 keV with the data grouped with a minimum of 20 counts per bin. Each model type was fit twice, once with the column density (N_H) as a free parameter and once with column density set at the Galactic value of 8.95×10^{20} cm^{-2} (Dickey & Lockman, 1990). All models allowed temperature, abundance, and normalization to vary. The simplest model used was a single temperature (1T) plasma with absorption (WABS×MEKAL). To test for multi-phase gas, a two temperature (2T) model was used by adding a second MEKAL component to the 1T model while tying the abundance parameters together.

We have also tested whether a cooling flow fits the spectrum by adding a cooling flow component to the single temperature model (WABS×(MEKAL+MKCFLOW)). The temperature of the thermal component was tied to the upper temperature of the cooling flow component. Two separate fits were found by testing different scenarios based on the MKCFLOW model temperatures. For the first scenario, we allowed both upper and lower temperatures to vary (VC), as well as abundance and normalization. In the second case, we set the lower temperature, kT_{low}, to 0.1 keV (e.g., Wise et al., 2004), allowing the gas to cool fully (FC), i.e., to below the temperature range detectable by Chandra. From this we found an upper limit on the mass condensation rate for the cluster within in the ACIS-S3 chip to be 137 $M_\odot$ yr^{-1}.

The results are in Table 2.2. The fits found for each model range in reduced χ^2 values from 1.1 to 1.5. Multiple temperature models are favored over the single temperature model, which is expected in a cooling-flow cluster. The temperature variations will be examined more closely in Section 2.3.6. All models with N_H allowed to vary proved better fits than the models set to the Galactic value, suggesting an error in the interpolation of the foreground value or error in the calculation of the buildup of hydrocarbons on the optical filter. The latter possibility is unlikely. A detailed CXC memo by Vikhlinin[1] claims the

[1]See `http://hea-www.harvard.edu/$\sim$alexey/acis/memos/`.

Table 2.2: Integrated spectral fits.

Model	kT (keV)	$kT_{\rm low}$ (keV)	Z	$N_{\rm H}$ ($10^{22}{\rm cm}^{-2}$)	$\dot{M}_{\rm X}$	$\chi^2/d.o.f$
1T	$3.65^{+0.05}_{-0.05}$	—	$0.46^{+0.03}_{-0.03}$	$0.116^{+0.003}_{-0.003}$	—	481.26/368
1T	$4.11^{+0.06}_{-0.06}$	—	$0.54^{+0.03}_{-0.03}$	0.0895	—	564.01/369
2T	$5.17^{+0.87}_{-0.32}$	$1.69^{+0.12}_{-0.10}$	$0.37^{+0.03}_{-0.04}$	$0.120^{+0.004}_{-0.003}$	—	402.25/366
2T	$5.25^{+0.34}_{-0.36}$	$1.65^{+0.11}_{-0.22}$	$0.49^{+0.03}_{-0.03}$	0.0895	—	503.93/367
VC	$4.31^{+0.11}_{-0.11}$	$0.37^{+0.04}_{-0.04}$	$0.46^{+0.03}_{-0.03}$	$0.129^{+0.003}_{-0.004}$	145^{+16}_{-18}	397.59/366
VC	$8.53^{+0.52}_{-3.01}$	$1.33^{+0.08}_{-0.09}$	$0.51^{+0.03}_{-0.03}$	0.0895	367^{+21}_{-83}	503.19/367
FC	$4.23^{+0.11}_{-0.11}$	0.1	$0.47^{+0.03}_{-0.03}$	$0.132^{+0.004}_{-0.004}$	137^{+17}_{-17}	400.63/367
FC	$4.30^{+0.09}_{-0.09}$	0.1	$0.56^{+0.03}_{-0.03}$	0.0895	29^{+10}_{-10}	556.21/368

calibration of the buildup is known to better than 5% at low energies.

To understand how this absorption is distributed across the field of view, we created elliptical annuli containing about 5000 net counts. Fitting each of these regions with a single temperature model over the same energy range as before, we produced the N_H radial profile shown in Figure 2.5. The dotted line indicates the Galactic value for hydrogen column density. The profile shows no radial trend, but overall the column density is above the Galactic value in all regions. The average column density for this region is better fit with the value 1.22×10^{21} cm^{-2}. This value is in agreement with the fitted values for the integrated spectrum. For all models used in this analysis, a significantly better fit is found using this average column density rather than the Galactic value. Therefore, we have adopted it for the remainder of this paper.

2.3.4 The X-ray Bar

The bar region, indicated in Figure 2.2 (point A), stands out as a strong peak in surface brightness. We determined its dimensions from its average surface brightness profiles in the directions perpendicular and parallel to its major axis. Using the full-width at half-maximum of the average peaks found in Figure 2.6, the length is 22.5″ and width is 10″. These dimensions were used to isolate its spectrum. A total of 3350 net counts were detected in the extracted region. The center of a cluster suffers the most from projection effects, so contributions from four annular regions outside of the bar containing 15,000 net counts each were fitted for deprojection. The resulting fit of the PROJCT(WABS×MEKAL) model for the bar is presented in Table 2.3. The electron density of the region is 0.066 cm^{-3}, corresponding to a total mass of 3.21×10^{10} $M_\odot$. If the gas in the bar was all cooling to low temperatures on its cooling timescale, it would be depositing about 91 $M_\odot$ yr^{-1}. The density, pressure, entropy, and cooling time are all consistent with the values fit for the central region of the radial analysis, found later in Section 2.3.6.

We will now consider the possibility that the bar is actually shaped more like an edge-on disk. Before we assumed that the bar is prolate, with its major axis in the plane of the sky. The edge-on disk is oblate, with its minor axis assumed to lie in the plane of the sky. With a larger volume because of the oblate geometry, a lower density will be measured. These differences are presented in Table 2.3. With these assumptions the density and pressure decrease to 0.0443 cm^{-3} and 2.42×10^{-10} erg cm^{-3}, respectively. The entropy and cooling time rise to 13.6 keV cm^2 and 5.3×10^8 yr, respectively. The mass increases to 7.22×10^{10}

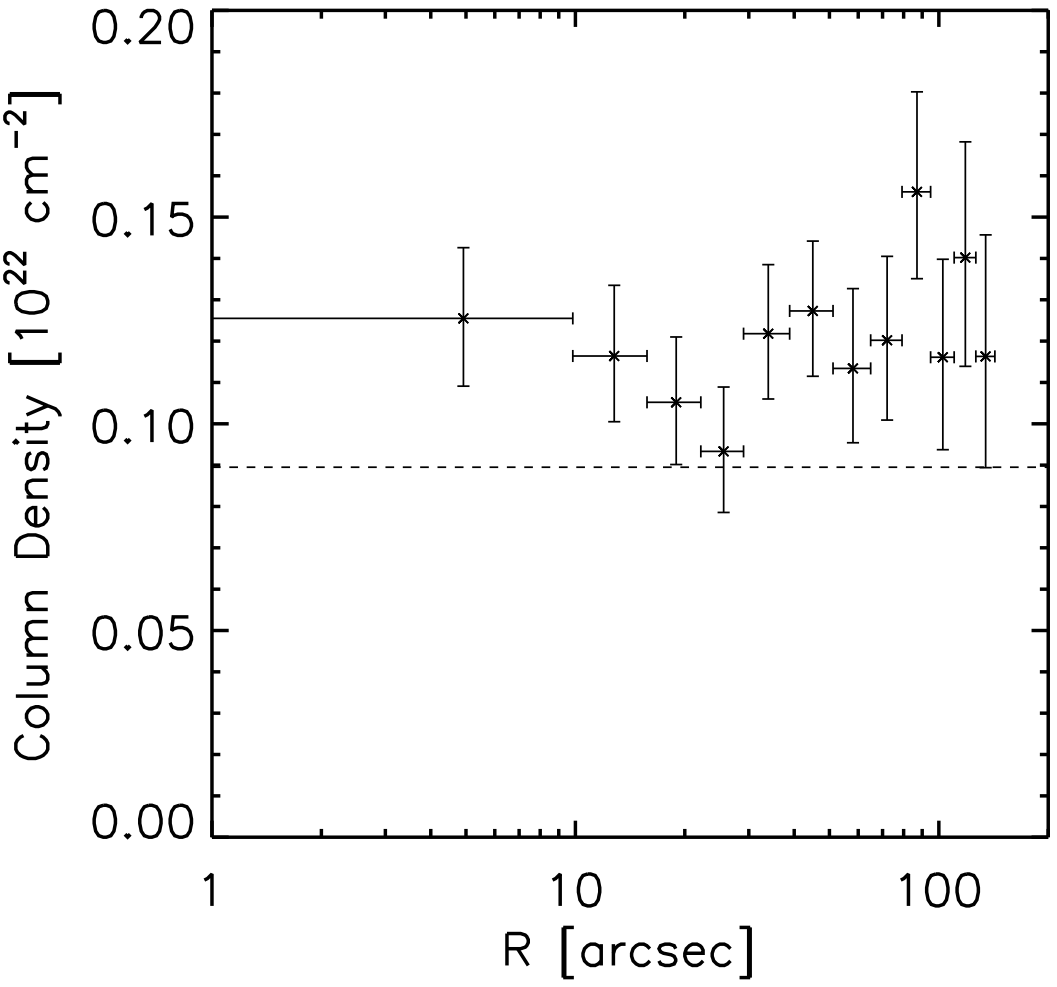

Figure 2.5: Hydrogen column density profile (projected). The dashed line represents the Galactic value.

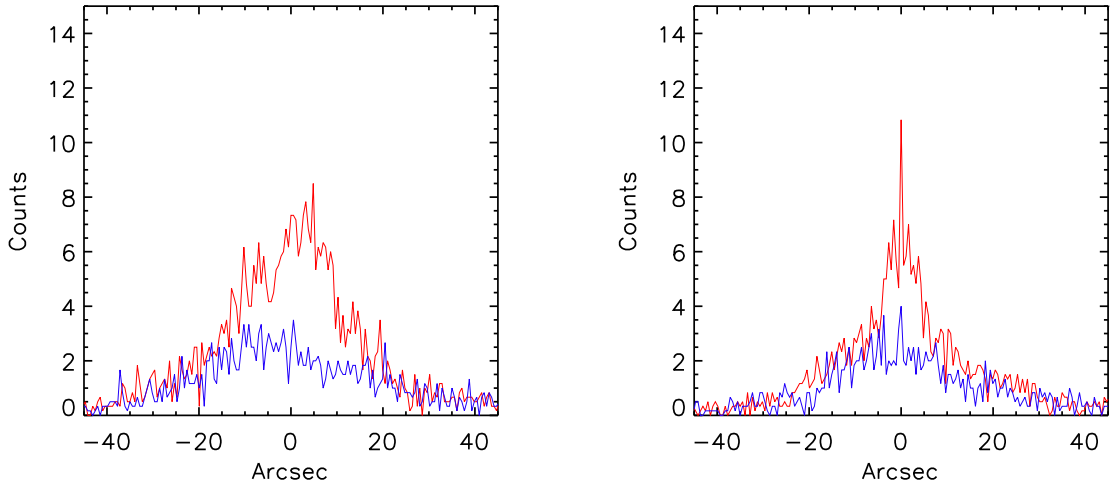

Figure 2.6: *Left*: Average surface brightness (in total counts) parallel to the length of the bar. *Right*: Average surface brightness (in total counts) parallel to the width of the bar. The red lines indicates the profile directly through the bar. The blue line is the average profile of the region immediately outside of the bar for comparison.

Table 2.3: Physical properties of the central region of A1664.

Geometry	n_e (10^{-2} cm^{-3})	P (10^{-10} erg cm^{-3})	S (keV cm^2)	t_{cool} (10^8 yrs)	M (10^{10} $M_\odot$)	$\dot{M}_X$
Bar	$6.64^{+0.27}_{-0.28}$	$3.63^{+0.21}_{-0.23}$	$10.4^{+0.5}_{-0.6}$	$3.5^{+0.4}_{-0.4}$	$3.21^{+0.12}_{-0.14}$	91^{+11}_{-11}
Disk	$4.43^{+0.17}_{-0.19}$	$2.42^{+0.14}_{-0.15}$	$13.6^{+0.7}_{-0.7}$	$5.3^{+0.6}_{-0.6}$	$7.22^{+0.28}_{-0.30}$	140^{+16}_{-16}

$M_\odot$, more than double the mass contained within the bar geometry. The assumed geometry does not affect our conclusions.

The CO-derived molecular gas mass for A1664 is 4.4×10^{10} $M_\odot$ (Edge, 2001). The total mass of the X-ray emitting gas in the bar is comparable to the cold molecular gas that resides at the same location. A study by Wilman et al. (2006) has shown that the CO and Hα emission are tracing the same gas, which is shown in the upper right panel of Figure 2.2. The X-ray bar structure is associated with this same disturbed region.

2.3.5 Metal Abundances

The metallicity analysis was carried out by creating adaptively sized regions containing an average 5000 net counts out to the edge of the CCD ($161''$). All regions have their own weighted response files created using *mkacisrmf* and *mkwarf*. After the spectrum for each region was extracted, each was modeled as a single temperature plasma (MEKAL) with an absorption component (WABS). The model was fit over the energy range 0.4 to 7.0 keV, with N_H set to our adopted value. Temperature, metallicity, and normalization were allowed to vary. The abundance ratios used in this analysis are from the most current photospheric data of Grevesse & Sauval (1998).

The projected metallicity profile is presented in the left panel of Figure 2.7 represented by the solid points. The abundance rises from the center of the cluster at 0.54 solar to 0.75 solar at $21''$ and remains constant out to about $45''$. The metallicity then declines to approximately 1/3 of the solar value at a radius of $100''$. The central dip in metallicity is unusual, although central abundance dips have been observed in several clusters such as Centaurus A (Sanders & Fabian, 2002), Perseus (Schmidt et al., 2002), and M 87 (Böhringer et al., 2001). Usually the metallicity rises to the center in cooling flows (De Grandi & Molendi, 2001). Our current understanding of the central metal enhancement of cooling flow clusters posits that SN Ia in the central galaxy are enriching the gas with iron and other metals. The peak metallicity is expected to be centered on the BCG. These rare systems with central dips may be explained by resonance scattering (Gilfanov et al., 1987), multiphase gas (Buote, 2000), warm+hot ISM (Buote, 2001), or bimodal metallicity distributions (Morris & Fabian, 2003).

We explore the metallicity profile first by taking into account projection effects. A deprojected fit was carried out using 5 radial bins, containing roughly 10000 net counts each. The spectrum for each region was modeled as a single temperature plasma with foreground absorption, but now with the additional projected component. The open circles in Figure 2.7 representing the deprojected profile show that the abundance dip becomes

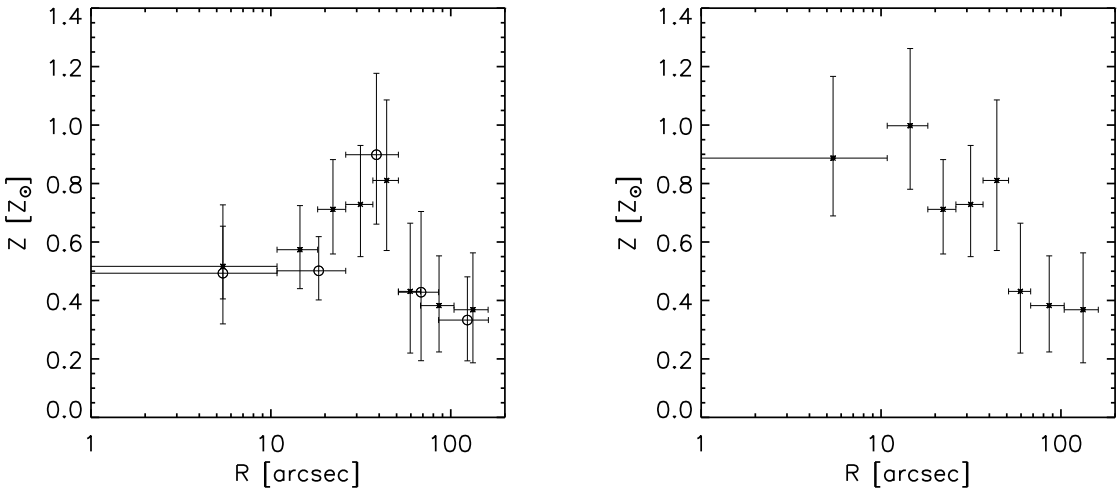

Figure 2.7: *Left*: Projected (*solid points*) and deprojected (*circles*) metallicity profile of the ICM in solar units. An unusual dip occurs in the central $\sim 50''$. *Right*: Metallicity profile of ICM in solar units. The inner two points were derived using a cooling flow model for a better metallicity estimation.

more pronounced. Overall the 5 bins generally remain within errors of the projected profile. The peak at 45″ lies at a value of 0.93 solar. To within errors, this value is consistent with the projected value at the same radius.

We now explore the possibility of multiphase gas and low energy absorption due to warm gas. Molendi & Gastaldello (2001) have shown that a single temperature model can bias a measurement to lower metallicities. It was previously demonstrated by Buote (2000) that this bias is due to the abundance measurement being sensitive to the Fe-L complex at low temperatures. In a multiphase medium, the Fe-L complex is excited by a range of temperatures around 1 keV, resulting in a broader spectral shape. A single, average temperature would treat this broad peak as a lower metallicity feature, resulting in an underestimation of the actual abundance.

Using the same regions and model we used for the projected analysis, we added a cooling flow component to the model (WABS×(MEKAL+MKCFLOW)) with the upper temperature tied to the temperature of the thermal component. The lower temperature was set at 0.1 keV to allow full cooling. A significant improvement in the fit was found for the inner two regions when adding this component. An F-test shows that the outer six regions improve slightly or remain the same. The reduced chi-squared values for both models are presented in Table 2.4.

The new abundance profile with the inner two regions modeled with cooling flows is shown in the right panel of Figure 2.7. The central metallicity dip has largely gone away. To within the errors, the profile is centrally peaked. The upper limit on the mass condensation rate for these two regions was found to be $56\pm10\ M_{\odot}\ \mathrm{yr}^{-1}$. In an attempt to improve the fit of the inner most region further, we assume that there may be a reservoir of warm gas ($\sim 10^5$ K), being deposited from the cooling flow, acting as a source of extra absorption in the lower energy range of the spectrum (0.4 - 0.8 keV). There is a known reservoir of cold gas that is comparable in mass to the hot X-ray emitting gas associated with the BCG (discussed in sec 3.3.1). Our assumption is that if the cooling flow is directly feeding the cold gas, then there would be gas in the intervening temperature range, though the amount expected is small due to extremely short cooling times and therefore the effect should be minimal. This extra absorption was represented using the EDGE component in XSPEC. A visual inspection of the spectrum at lower energies shows the fit is no longer systematically higher than the data, which increases the metallicity measurement to the solar value. However, by introducing two new free parameters to the model, the chi-squared value did not improve significantly.

Table 2.4: Reduced chi-squared fits for radial metallicity profile.

Region	Model	χ^2_{norm}	$d.o.f.$
Reg. 1	1T	1.15	133
	CF	0.98	132
Reg. 2	1T	1.35	146
	CF	1.07	145
Reg. 3	1T	1.06	148
	CF	0.97	147
Reg. 4	1T	1.20	153
	CF	1.15	152
Reg. 5	1T	0.99	156
	CF	0.92	155
Reg. 6	1T	1.17	152
	CF	1.17	151
Reg. 7	1T	0.95	206
	CF	0.93	205
Reg. 8	1T	1.12	234
	CF	1.10	233

2.3.6 Physical State of the Gas

A radial temperature analysis was performed by extracting regions from the same area of the CCD as the metallicity analysis. The sizes of the annuli were adjusted so that each contained approximately 2000 net counts. The radial bins were fit in projection following the same procedure and using the same model as described above in the metallicity analysis.

Shown in Figure 2.8 as asterisks, the temperature reaches a minimum of 2.2 keV at the center of the cluster. At a radius of about 18″, the temperature rises from 2.6 ± 0.1 keV to 2.9 ± 0.2 keV and drops back down to 2.5 ± 0.2 keV in the next annulus. This feature may be due to an asymmetric temperature structure caused by the eastern cold front. From there, the profile rises steeply to 4.6 keV at about 45″ and reaches its peak temperature of 5.7 keV at around 100″. We note that when fitting the temperatures with the abundances tied to those derived using the cooling flow model in Section 2.3.5, the changes in the best fit values are imperceptible.

The deprojected temperature profile was divided into 8 elliptical annuli. The temperature was determined using the PROJCT component in XSPEC, as before. The open circles represent the deprojected temperature profile in Figure 2.8. Apart from the central bins, the deprojected profile agrees with the projected profile. The central temperature decreases to 1.7 keV, making it 0.5 keV cooler than found in the projected profile. Between the second and third radial bin, the temperature jump is still apparent in the temperature structure.

Density, pressure, entropy, and cooling-time profiles have been derived from the same radial bins. The density profile, obtained from the deprojection of the surface brightness profile, is shown in the upper left panel of Figure 2.9. The core reaches an electron density of 0.07 cm^{-3}, which is comparable to that found in the core of the Perseus cluster (Fabian et al., 2006). The profile decreases radially to below 0.002 cm^{-3} in the last annulus at a radius of 160″.

The pressure profile was calculated as $2kTn_e$. The upper right panel of Figure 2.9 shows the pressure peaking at the center at a value of $5{\times}10^{-10}$ erg cm^{-3}. At 20″, there is a break in the profile. This is related to the temperature decrease described above.

The entropy profile in the lower left panel of Figure 2.9 was calculated using the standard relationship $S = kTn_e^{-2/3}$. The profile shows evidence for feedback in the core. A cluster without heating would have an entropy profile that decreases roughly as a power law to the center (Voit et al., 2002; Kay et al., 2004). We find that the profile decreases inward and then flattens at small radii around 13 keV cm^2. This entropy floor is normally found in cooling flow clusters (Voit & Donahue, 2005) where AGN activity is thought to

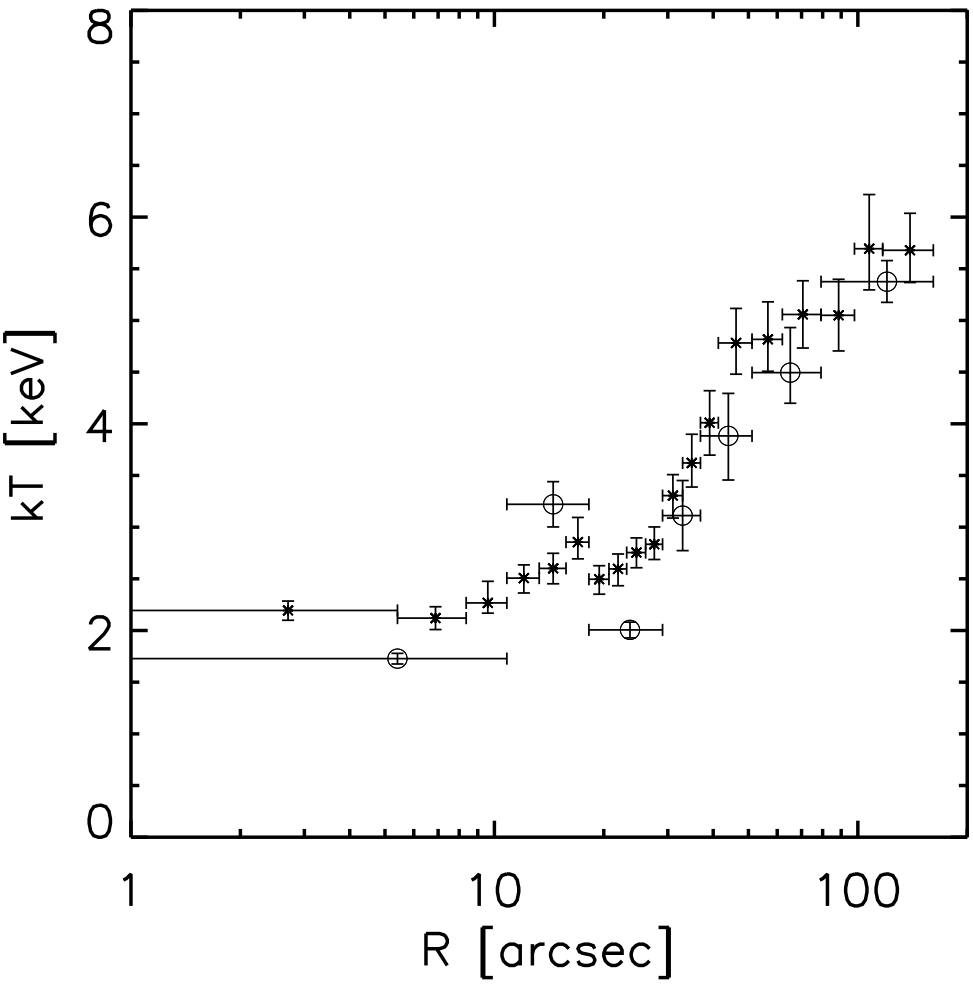

Figure 2.8: Projected (*solid points*) and deprojected (*circles*) X-ray temperature of the ICM.

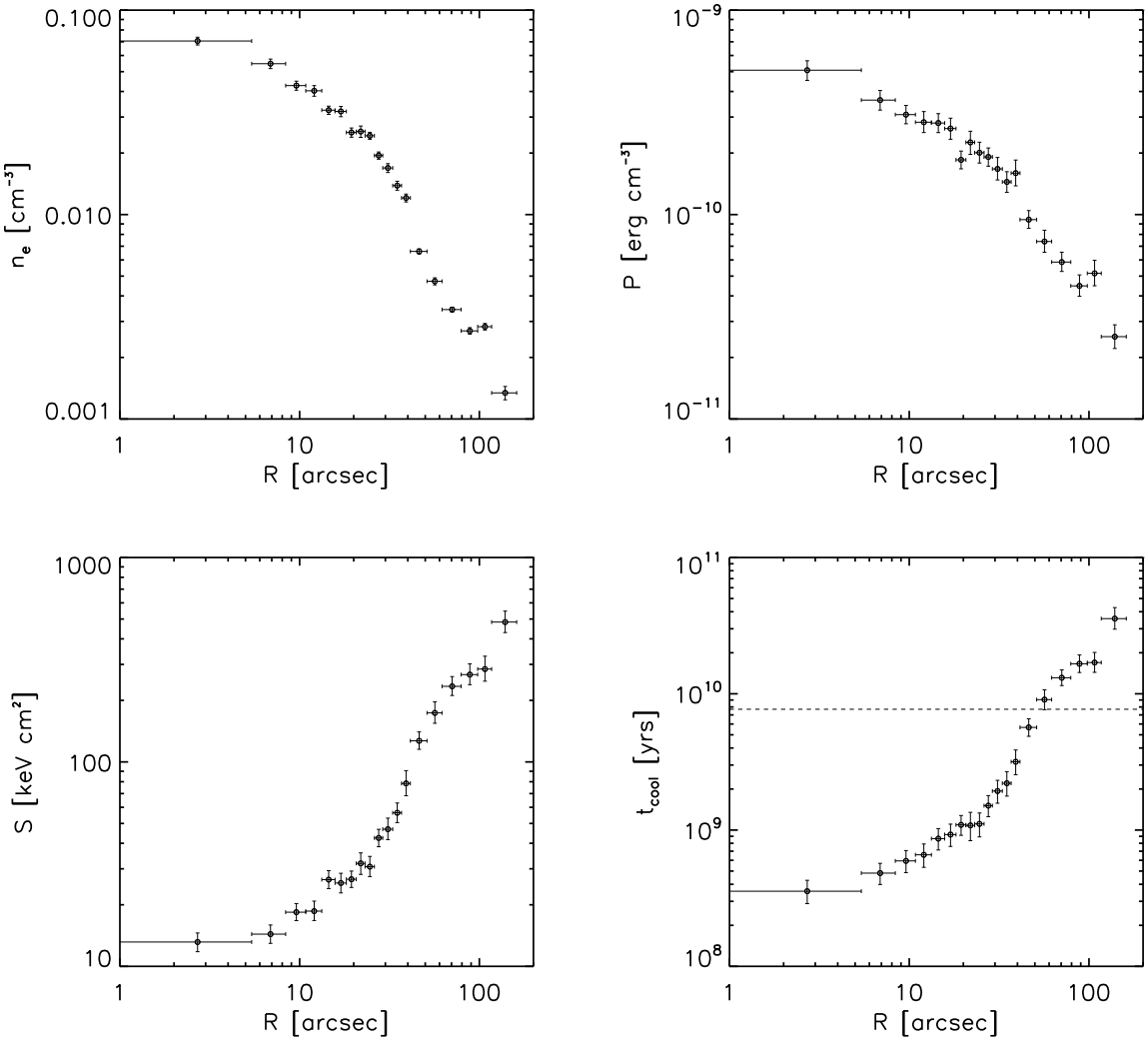

Figure 2.9: *Upper left*: Density profile of the ICM. *Upper right*: Pressure profile of the ICM. *Lower left*: Entropy profile of the ICM. *Lower right*: Cooling time profile of the ICM. Bins below the dotted line (7.7×10^9 yr) are considered to be within the cooling region.

be flattening out the profile by periodically releasing energy back into the surrounding gas. We present the cooling time as a function of radius in the lower right panel of Figure 2.9. The short central cooling times are characteristic of a cooling flow cluster. The decreasing cooling time towards the center reaches its minimum value of 3.6×10^8 yr, which is consistent with star forming cooling flows. The sample of Rafferty et al. (2008) showed that star formation is preferentially found in systems with a central cooling time less than approximately 5×10^8 yr, and with entropy less than 30 keV cm^2.

We pointed out in Section 2.3.2 that the central structure is asymmetric. A cold front could explain the structure in the global temperature profile. We have analyzed the eastern half of the cluster, between 99 and 273 degrees from west on the sky, towards the brightness edge pointed out in Figure 2.2 (point B). The surface brightness profile in the direction of this region is shown in the upper left panel of Figure 2.10. The break in the surface brightness profile at approximately $30''$ corresponds to a density and temperature discontinuity shown in the upper right and lower left panel of the Figure 2.10. Across the front, away from the center, we find that density falls from 0.018 cm^{-3} to 0.008 cm^{-3}. The temperature jumps at the front from about 3 keV to about 5.5 keV. However, the pressure profile in the last panel of Figure 2.10 is continuous and shows no break. This is characteristic of a cold front, possibly induced by sloshing of the ICM in the core due to a recent merger. A1664 hosts a radio relic in the outer halo of the cluster (Giovannini et al., 1999; Govoni et al., 2001). Radio relics are thought to be a signature of mergers (Enßlin et al., 1998; Enßlin & Brüggen, 2002), strengthening the case for merger induced sloshing in A1664.

2.3.7 Star Formation in the BCG

The visual light of A1664's BCG, shown in Figure 2.2, is centered at R.A. = $13^h03^m42^s.54$, DEC = $-24°14'42''.05$, which lies 2.18" NE from the X-ray centroid. The R- and U-band surface brightness profiles are presented in the left panel of Figure 2.11. We constructed these profiles using the *ellipse* routine in IRAF with elliptical annuli of ellipticity 0.46 and position angle 10° from north on the sky, based on the best fit to the BCG envelope. Nearby galaxies projected onto the envelope were masked out to avoid light contamination. The images were flux calibrated using Landolt standards. The Galactic foreground extinction correction was calculated following Cardelli et al. (1989), assuming a foreground color excess of E(B–V) = 0.141. Evolution and K-corrections from Poggianti (1997) were applied in both filters as -0.143 and 0.130 magnitude in R and -0.161 and 0.328 magnitude in U, respectively. The error bars represent the statistical errors and the dashed lines represent

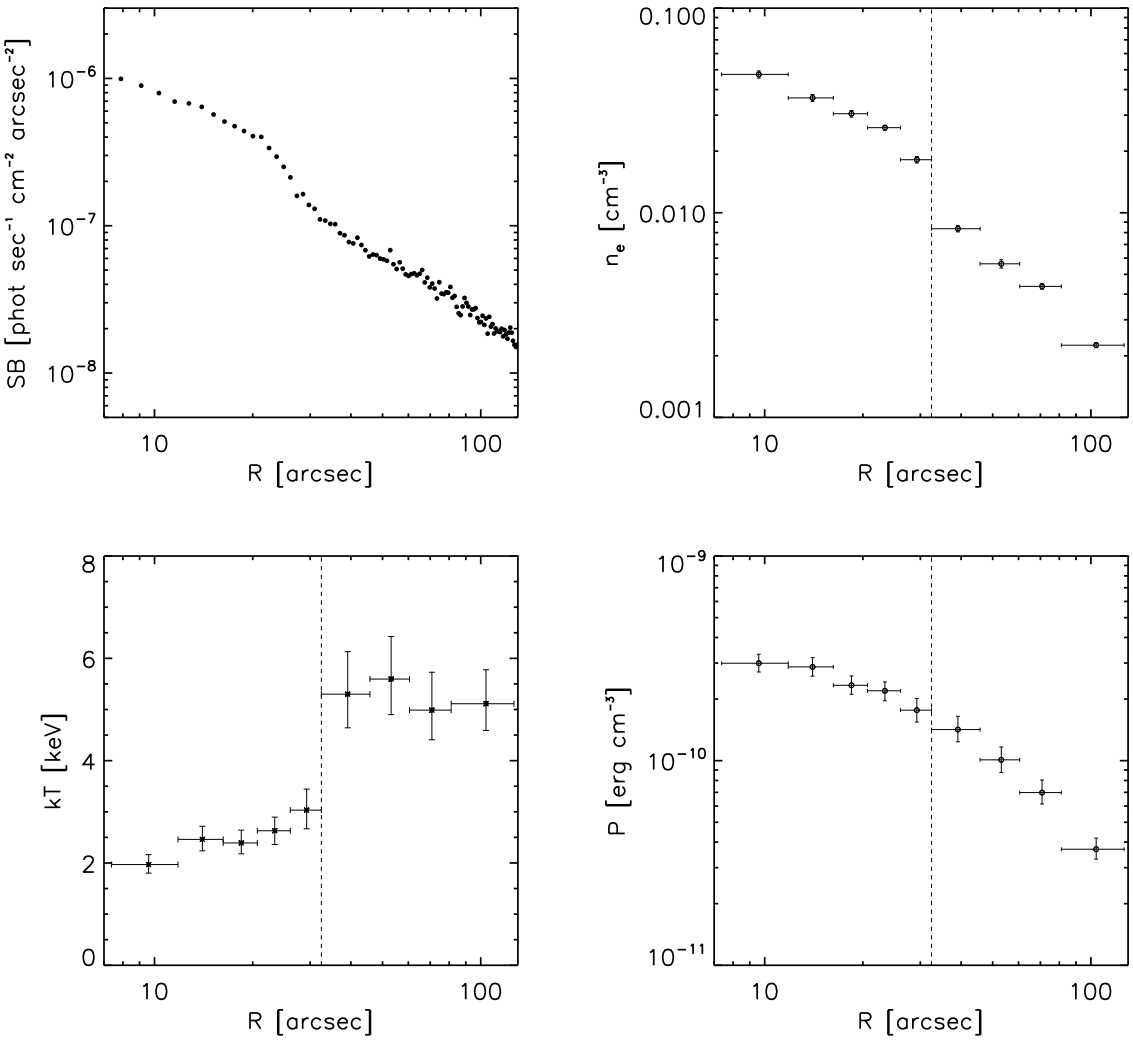

Figure 2.10: *Upper left*: X-ray surface brightness profile of the eastern half of A1664 in the 0.4 - 7.0 keV band. *Upper right*: Eastern half density profile of the ICM. The vertical line at $\sim 30''$ represents where the surface brightness discontinuity is located. The density is discontinuous at this point as well. *Lower left*: Eastern half temperature profile of the ICM. The temperature sees a $\sim$ keV jump at the discontinuity. *Lower right*: Eastern half pressure profile of the ICM. The pressure remains continuous across the discontinuity.

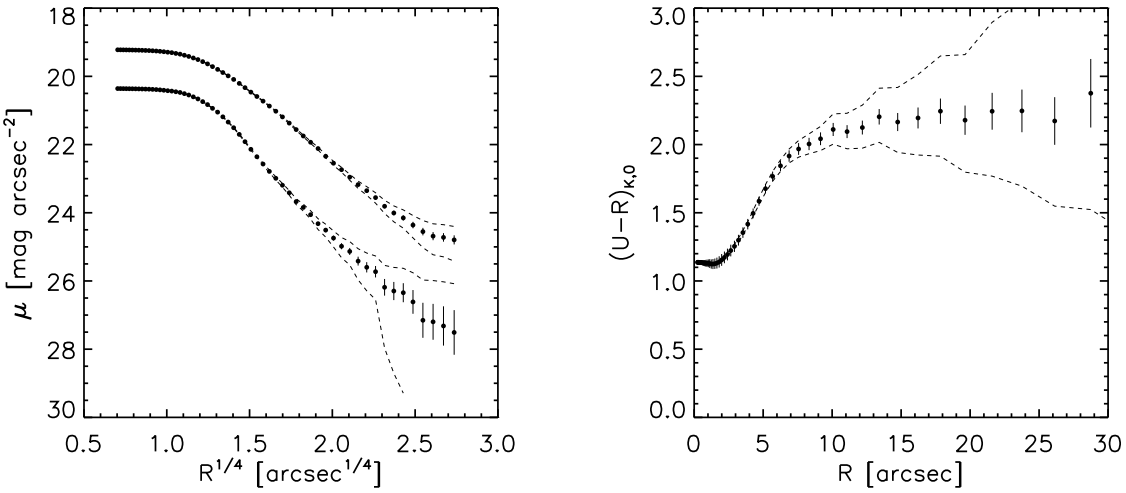

Figure 2.11: *Left*: R (upper) and U-band (lower) surface brightness profiles of the cD galaxy. Statistical errors are imperceptible at most point. The dashed lines represent the systematic uncertainty associated with the sky background subtraction. *Right*: *U*–*R* color profile of the cD galaxy illustrating the central $\sim 10''$ starburst region. Statistical errors and systematic error envelope are shown.

the systematic error confidence intervals. The method of determining these is described in McNamara & O'Connell (1992).

In the right panel of Figure 2.11, we present the U–R color profile. The inner $10''$ shows a positive gradient (bluer toward the center) with a central rest-frame color of 1.1. The envelope of the BCG reddens to a color of approximately 2.3. The central color is about one magnitude bluer than a normal giant elliptical, which have colors of 2.3 - 2.6 (Peletier et al., 1990). This indicates star formation.

The U-band image, after subtraction by a smooth stellar model, is presented in the left panel of Figure 2.12. Two distinct peaks can be seen in this image north and south of the center. To the right of this in Figure 2.12, we show the color map on the same scale. The normal colors are in white and the unusually blue regions are blue. The blue features are concentrated to the center with trails of emission leading north, south, and east. The trails to the north and south appear to end at or near neighboring galaxies. The two galaxies labeled 1 and 2 in Figure 2.2 are both red and have an average color of 2.5 and 2.2 respectively. Galaxy 1 has an absolute visual magnitude of approximately -22.7 ($2L_\star$) and galaxy 2 is approximately -21.1 ($0.5L_\star$). These appear to be giant ellipticals which are normally devoid of cold gas, so their relationship to the star formation in the BCG, if any, is ambiguous. They are unlikely to be the donors of the $\sim 10^{10}$ $M_\odot$ of cold gas feeding star formation in the BCG.

2.4 Discussion

2.4.1 AGN Feedback

AGN periodically inject energy to heat the ICM and quench cooling of the surrounding medium (Bîrzan et al., 2004; Dunn & Fabian, 2006; Rafferty et al., 2006). To determine whether heating is dominating in A1664, we compare the mechanical power of the AGN to the cooling power of the ICM. AGN power can be evaluated as the pV work required to inflate a cavity against the surrounding pressure of the hot ICM. In A1664, there are no detected cavities in the X-ray. We can, however, estimate the AGN power using the scaling relations found by Bîrzan et al. (2008) between jet mechanical power and radio synchrotron power. These relations were derived using a sample of radio galaxies with X-ray cavities. All results referred to in this discussion are presented in Table 2.5.

The radio flux emerging from the nucleus of the BCG was obtained from the NVSS catalogue. The source is unresolved in the $45''$ FWHM beam. Its 1.4 GHz flux 36.4 mJy

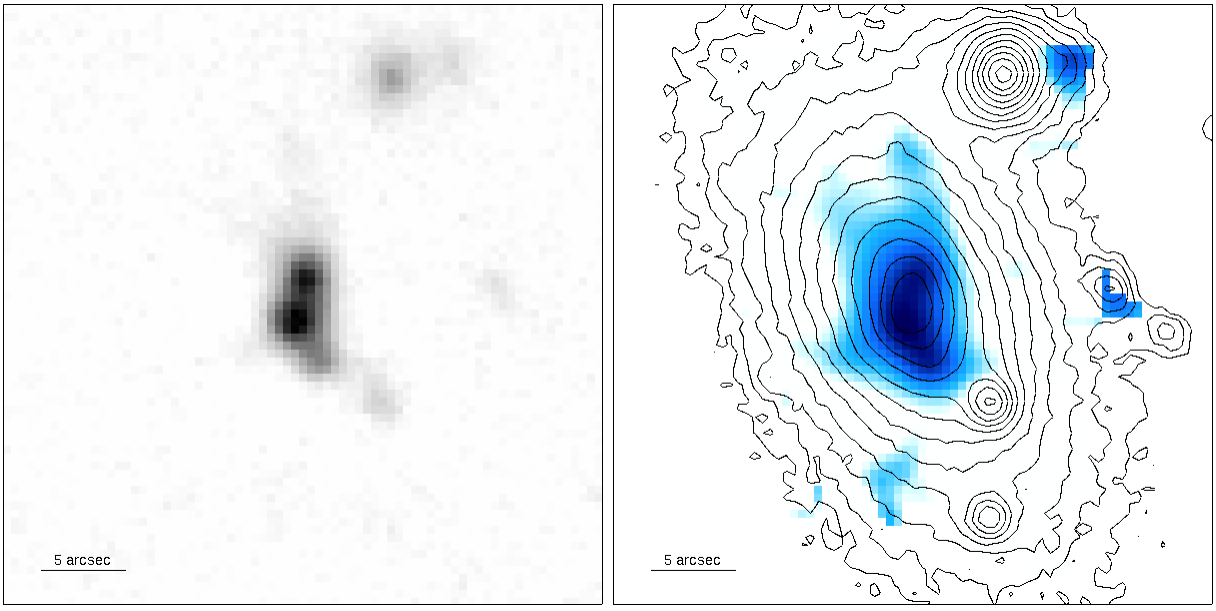

Figure 2.12: *Left*: U-band image after subtracting the smooth model galaxy. This image illustrates the separate star forming clumps. *Right*: U–R color map with R-band contours overlaid. The blue regions are shown in blue; the normal colored regions are in white. Four blue trails can be seen leading away from the center. North is towards the top; east is towards the left.

Table 2.5: Derived properties from X-ray & radio data.

Parameter	Value
S_{1400} (mJy)	36.4±1.2
P_{1400} (10^{24} W Hz^{-1})	1.57±0.05
S_{352} (mJy)	329±9
P_{352} (10^{24} W Hz^{-1})	14.2±0.4
$P_{cav,1400}$ (10^{42} erg s^{-1})	82.9±19.4
$P_{cav,352}$ (10^{42} erg s^{-1})	66.7±29.8
L_X (10^{42} erg s^{-1})	291±6
L_{CF} (10^{42} erg s^{-1})	46.5±10.8
r_{cool} (kpc)	117

corresponds to a power of 1.57×10^{24} W Hz^{-1}. The bulk of the energy from FR I radio sources emerges in the form of mechanical energy. Using the 1.4 GHz relationship of Bîrzan et al. (2008),

$$\log P_{\rm cav} = (0.35 \pm 0.07) \log P_{1400} + (1.85 \pm 0.10), \tag{2.2}$$

where $P_{\rm cav}$ has units of 10^{42} erg s^{-1} and P_{1400} has units of 10^{24} W Hz^{-1}, we estimate the jet power to be 8.29×10^{43} erg s^{-1}.

Rafferty et al. (2008) have shown that star formation is predominately found in systems where the X-ray cooling luminosity is greater than the jet power. To test this in A1664, we derived the X-ray luminosity by fitting the cooling region with a single temperature MEKAL model and using the bolometric flux (0.001-100.0 keV) of the model to calculate the luminosity. Similarly, the cooling flow luminosity was calculated from the flux of an additional MKCFLOW component with the lower temperature set to 0.1 keV. The cooling luminosity, $2.45\pm0.12\times10^{44}$ erg s^{-1}, is calculated as the the difference between these two values. The cooling luminosity here is three times greater than the estimated jet mechanical power found from Bîrzan's relation.

The uncertainty in the jet power is large. We can check our conclusions by using radio power measurements at a lower frequency. The radio flux from the nucleus of the BCG in the 352 MHz WISH catalogue is 329 mJy (De Breuck et al., 2002). With this we can independently check the the cavity power estimated using the 1.4 GHz flux. Using the 327 MHz relationship of Bîrzan et al. (2008) (where we assume the difference in frequency dependent flux is negligible),

$$\log P_{\rm cav} = (0.62 \pm 0.08) \log P_{327} + (1.11 \pm 0.17), \tag{2.3}$$

we find a cavity power of 6.67×10^{43} erg s^{-1}. This value is consistent with the cavity power found with the 1.4 GHz flux. An additional constraint is found using Bîrzan's relationship between jet power and lobe radio luminosity corrected for break frequency to account for aging effects,

$$\log P_{\rm cav} = (0.53 \pm 0.09) \log L_{\rm rad} - (0.74 \pm 0.26) \log \nu_C + (2.12 \pm 0.19). \tag{2.4}$$

$L_{\rm rad}$ and $P_{\rm cav}$ are in units of 10^{42} erg s^{-1} and ν_C is in units of GHz. Correcting for the break frequency reduces the scatter in this relationship by $\sim 50\%$ compared to the monochromatic relations. The VLSS survey gives a 74 MHz flux for A1664 of 1.16 Jy. Combining this flux measurement with the previous ones, we calculated the total radio luminosity by integrating the flux from 10 MHz to 10 GHz as two broken power law spectra, with spectral indices of 0.81 between 10 MHz and 352 MHz and 1.59 between 352 MHz and 10 GHz. The total radio luminosity is found to be $2.01\pm0.05\times10^{41}$ erg s^{-1}. We are using the total flux (lobe

plus some core flux), so this should be considered an upper limit to the lobe luminosity. The shape of the spectrum is defined by just three flux measurements. We have therefore taken the intermediate flux at 352 MHz to be the rough estimate of the break frequency. Based on Bîrzan et al. (2008), this is a reasonable lower limit. Adopting these assumptions, we estimate the upper limit on P_{cav} to be 1.80×10^{44} erg s^{-1}. Again, this result is consistent with the cooling luminosity being greater than the energy output by the AGN.

The scatter in the Bîrzan power relations is larger than the calculated difference between the jet power and the cooling luminosity. We cannot exclude the possibility that the AGN power exceeds the cooling luminosity. However, taking these figures at face value, the Bîrzan relations give a jet power that is consistently below the cooling luminosity. With this, the absence of detected cavities, and evidence for cooled gas in gravitational free-fall at the center (Wilman et al., 2009), it appears that the AGN is currently underpowered compared to the cooling luminosity. The hot atmosphere is now in a cooling phase.

2.4.2 Criteria For Cooling Flow Driven Star Formation

Since A1664 has an unusually blue core in the BCG with a star formation rate of 23 $M_\odot$ yr^{-1}, we have investigated whether gas cooling out of the ICM is directly feeding the cold gas reservoir and fueling star formation. We tested A1664 against the criteria of Rafferty et al. (2008) for star formation that require the jet power to be less than the X-ray cooling luminosity, a central cooling time less than 5×10^8 yr or a minimum entropy threshold of 30 keV cm^2, and a maximum of 20 kpc separation between the optical and X-ray centroids. We have shown in previous sections that A1664 has an underpowered jet as well as a central cooling time and entropy of 3.5×10^8 yr and 10.4 keV cm^2, respectively. The X-ray and optical centroids calculated have a separation of $\sim$ 5 kpc, which satisfies all of the criteria.

There are two other indications we have explored that star formation is related to the cooling flow (X-ray cusp). Clusters below the entropy threshold are more likely to have high luminosity Hα emission (Cavagnolo et al., 2008; Voit et al., 2008), a good tracer of star formation. A1664 is one the brightest Hα emitters in the ROSAT brightest cluster sample (Crawford et al., 1999). Also, the derived upper limit on the mass condensation rate (56 $M_\odot$ yr^{-1}) is larger than the star formation rate, although they are consistent to within their uncertainties. Rafferty et al. (2006) found that the average ratio of mass condensation to star formation was approximately four. For A1664, the ratio is smaller ($\sim$ 2.4). The upper limit on cooling being greater than the star formation rate is consistent with a cooling flow driven starburst.

2.4.3 Gas Deposited by Stripping

Cold gas and star formation in BCGs are found almost exclusively in clusters with cooling flows (i.e., central cusp of dense gas). Therefore, the origin of this cold gas must be linked in some way to the presence of the X-ray cusp. Throughout this paper we have argued that this link is through condensation from the dense cool gas. Another possible link could be through ram pressure stripping. Because of the high density cusp, the cross section to ram pressure stripping is larger in the center than in the cluster outskirts. Stripping could then be strong enough to drive dense molecular gas out of a gas-rich galaxy plunging through the cusp and depositing it onto the BCG.

Blue streams seen in Figure 2.12 could plausibly be star formation in cold gas stripped from plunging galaxies. Two of the blue trails appear to end near red ellipticals, so their origin is unclear. For the case of the southern most trail, Wilman et al. (2006) has suggested that it has been dynamically induced by a disturbance from the nearby galaxy (point 2 in Figure 2.2).

We will now consider the possibility that the 10^{10} $M_{\odot}$ cold gas reservoir was built up from gas stripped from spiral or gas-rich early-type galaxies. Previous observations have shown that lower density cold gas from a galaxy begins to be stripped at about 0.6 to 1 Mpc from the center of a cluster (Kenney & Koopmann, 1999; Vollmer et al., 2001). To determine if any gas will remain in a galaxy to be deposited onto the BCG, we calculated whether a face-on, high density disk of molecular gas can survive a close passage to the center of the cluster. In order to find the radius when stripping should occur, we compare the ram pressure stripping force to the maximum gravitational restoring force of the galaxy parallel to the flow as:

$$\rho v^2 = \frac{\partial \Phi(\varpi, z)}{\partial z} \sigma_{\rm s}. \tag{2.5}$$

Here, ϖ is the radius of the cold gas disk, z is the distance perpendicular to the disc, ρ is the density of the ICM, v is the velocity of the galaxy through the ICM, and $\sigma_{\rm s}$ is the surface density of the cold gas disk. Assuming the galaxy has an NFW potential (Navarro et al., 1997), the specific form for our model galaxy is,

$$\Phi(r) = -\frac{GM \ln(1 + \frac{r}{r_{\rm s}})}{r(\ln(1+c) - \frac{c}{1+c})}, \tag{2.6}$$

where $r = \sqrt{\varpi^2 + z^2}$, M is the mass enclosed at r_{200}, $r_{\rm s}$ is the scale radius, and c is the ratio of r_{200} to the scale radius. For our calculations we assume this ratio to be 10 to 1. Solving equation 2.5 for the velocity of a galaxy to overcome the maximum gravitational

restoring force per unit area,

$$v^2 = \frac{GMz\sigma_{\rm s}}{r^2\rho(\ln(1+c) - \frac{c}{1+c})}\left(\frac{\ln(1+\frac{r}{r_{\rm s}})}{r} - \frac{1}{r+r_{\rm s}}\right), \tag{2.7}$$

we present in Figure 2.13 how this varies with cluster radius for different galaxy types, assuming the density profile of A1664 (Figure 2.9).

The dotted line in Figure 2.13 represents a typical small spiral galaxy ($M = 10^{11}$ $M_\odot$, $\sigma_{\rm s} = 100$ $M_\odot$ pc^{-2}, $r_{200} = 200$ kpc, $\varpi = 0.3$ kpc, $z = 1.11$ kpc), such as IC 342 (Crosthwaite et al., 2001). Comparing this to the cluster's velocity dispersion of 900 km s^{-1} (Allen et al., 1995), it is likely the galaxy would lose its gas before reaching the center due to the low threshold value, making it nearly impossible for a significant amount of gas to be deposited onto the BCG. The solid line represents a typical large spiral galaxy ($M = 8 \times 10^{11}$ $M_\odot$, $\sigma_{\rm s} = 400$ $M_\odot$ pc^{-2}, $r_{200} = 210$ kpc, $\varpi = 0.4$ kpc, $z = 1.37$ kpc), such as M83 (Crosthwaite et al., 2002) or the Milky Way (Scoville & Sanders, 1987). A galaxy of this type would be able to hold onto its high density gas until about 80 kpc from the center. It is plausible then for the gas to be deposited onto the BCG. However, according to simulations by Benson (2005), in-falling halos in this radial velocity range on plunging orbits are rare. On average, a spiral galaxy contains only a few 10^8 $M_\odot$ of molecular gas in the inner 1 kpc. There would have to be hundreds of these encounters to build up the amount of cold gas seen in A1664.

Large spiral galaxies can merge and form what is known as a luminous infrared galaxy (LIRG). These early-type galaxies contain a potential source of cold gas that is comparable to the amount of gas found in BCGs. The dashed line represents a typical LIRG ($M = 3 \times 10^{12}$ $M_\odot$, $\sigma_{\rm s} = 10^3$ $M_\odot$ pc^{-2}, $r_{200} = 250$ kpc, $\varpi = 0.5$ kpc, $z = 1.68$ kpc), such as NGC 4194 (Aalto & Hüttemeister, 2000). For galaxies in this range, it would be nearly impossible for any of the gas to be stripped, even in the cusp of A1664. Similarly, a typical ULIRG ($M = 10^{13}$ $M_\odot$, $\sigma_{\rm s} = 10^4$ $M_\odot$ pc^{-2}, $r_{200} = 300$ kpc, $\varpi = 1$ kpc, $z = 2.85$ kpc), represented by the dash-dot line, would also hang onto its gas despite ram pressure stripping. Tidal stripping would be a more viable method of removing the gas from these galaxies. However, tidal stripping has no connection to the cooling cusp. If galaxies are depositing 10^{10} $M_\odot$ of molecular gas in this way, we should see this happening in all clusters, not just in cooling flows.

Based on these calculations, ram pressure stripping is an improbable explanation for the cold gas reservoir in A1664's BCG. This leaves us to favor the cooling flow driven star formation scenario.

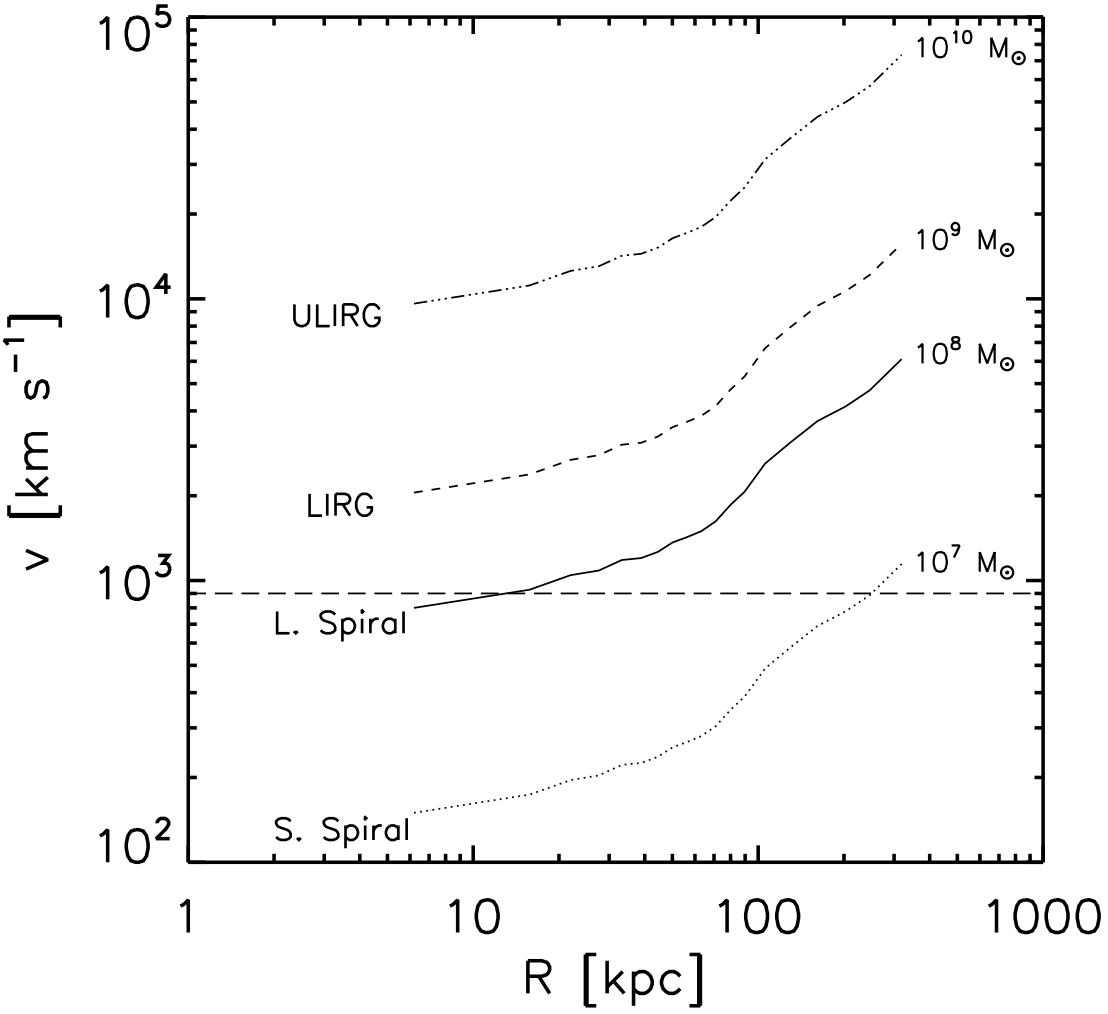

Figure 2.13: The velocity required at varying radii in A1664 for the ram pressure stripping force to overcome the maximum gravitational restoring force of dense molecular gas in different galaxies. From top to bottom, the lines represent typical ULIRG, LIRG, large spirals, and small spirals. Along the right side of the plot are the average masses of molecular gas found in the inner dense region of the galaxies. Across this range, galaxies towards the bottom are easier to strip, but have less gas to contribute to the BCG. Galaxies towards the top are harder to strip and are rare. The dashed horizontal line is the velocity dispersion of A1664.

2.4.4 Collapsed Cavity System

About 70 - 75% of cooling flow clusters have detectable X-ray cavities (Dunn et al., 2005). Thus, close to a third of cooling flows would either be in a state of pre- or post-AGN outburst. When cavities are formed, they sweep up low entropy gas into dense shells that may eventually break up and sink back to the cluster center. The X-ray bar could be the remains of collapsed cavity shells. Assuming the mass of the bar to be the minimum mass the AGN must have displaced, and further assuming the gas density (5.4×10^{-4} $M_\odot$ pc^{-3}) surrounding the bar to be the original, undisturbed density of the center, the amount of energy needed to displace 3.21×10^{10} $M_\odot$ of gas would be 3.1×10^{59} erg. This energy would correspond to two cavities 44 kpc in diameter. Energy and sizes of this magnitude are common in clusters (McNamara & Nulsen, 2007).

2.5 Summary

We have shown that star formation in Abell 1664 is consistent with fueling by the cooling flow. The BCG has a blue central color (positive color gradient), a central cooling time below 5×10^8 yr, a central entropy less than 30 keV cm^{-2}, an AGN power less than the X-ray cooling luminosity, and a BCG less than 20 kpc from the X-ray core. These properties are consistent with other star forming cooling flows (Rafferty et al., 2008). A large 10^{10} $M_\odot$ cold gas reservoir at the cluster center is also consistent with a cooling dominated cluster. It is unlikely that the gas was deposited by spiral or gas-rich early-type galaxies because it would take hundreds of encounters for it to be explained by ram pressure stripping alone. Other evidence that the cooling flow is directly feeding this reservoir comes from the measured mass condensation rate of 56 $M_\odot$ yr^{-1}, which compares well to the observed star formation rate of 23 $M_\odot$ yr^{-1}.

Additional evidence suggesting that A1664 is currently between AGN outbursts includes the possible collapsed cavity shell remnants we have referred to as the X-ray "bar". We have shown that the 3.1×10^{59} erg it would have taken to displace this gas would have created a pair of cavities approximately 44 kpc in diameter, typical of what is seen in galaxy clusters.

We further demonstrated that if gas in the central region is cooling at the rates estimated above, we can account for the apparent dip in the metallicity found when assuming a single temperature for the medium.

Chapter 3

Evidence for Outflow of Metal-Enriched Gas in Hydra A

3.1 Introduction

The elemental abundances of the hot gas at the centers of cooling flow clusters are often enhanced with respect to those at larger radii (De Grandi & Molendi, 2001). The high central iron abundance relative to the α-elements suggests the enhancements are largely composed of ejecta from type Ia supernova explosions associated with brightest cluster galaxies (BCG) (De Grandi et al., 2004; Tamura et al., 2004). Radial metallicity profiles of the hot gas tend to be broader than the stellar light profiles of BCGs, indicating that metal-enriched gas is diffusing outward and mixing with the intracluster medium (Rebusco et al., 2005, 2006; David & Nulsen, 2008; Rasera et al., 2008). BCGs frequently harbor active galactic nuclei (AGN) which are able to heat the metal enriched gas surrounding them, causing it to expand and mix with lower metallicity gas at larger radii (David & Nulsen, 2008). In addition, radio sources associated with AGN may be able to entrain metal enriched gas and transport it outward anisotropically along the radio jets and lobes (Gopal-Krishna & Wiita, 2001, 2003; Brüggen, 2002; Omma et al., 2004; Heath et al., 2007; Roediger et al., 2007).

Inclusions of unusually high metallicity gas have been found outside the centers of a handful of groups and clusters (Sanders et al., 2004; Gu et al., 2007; Simionescu et al., 2008), but their association with AGN has not been firmly established. Evidence linking a metal enriched outflow to jet activity has been found in the Hydra A cluster which shows enhanced metallicity near its radio lobes in an *XMM-Newton* X-ray image (Simionescu

et al., 2009). Hydra A has an extensive system of cavities embedded in its ICM that is filled with radio emission emanating from the nucleus of the BCG (McNamara et al., 2000; David et al., 2001; Nulsen et al., 2002, 2005; Wise et al., 2007). With a total energy of over 10^{61} erg, Hydra A is experiencing one of the most powerful AGN outbursts in the nearby universe. It is thus an ideal candidate to search for and characterize a metal-enriched outflow.

We performed such an analysis on a deep, high-resolution X-ray image obtained with the *Chandra X-ray Observatory*, and we find clear-cut evidence for metal enriched gas aligned with the radio source. Throughout this chapter we assume a ΛCDM cosmology with $H_0 = 70$ km s^{-1} Mpc^{-1}, $\Omega_M = 0.3$, and $\Omega_\Lambda = 0.7$. Hydra A is at a redshift of $z = 0.055$, which corresponds to an angular scale of 1.07 kpc arcsec^{-1}. All uncertainties are quoted at the 90% confidence level.

3.2 Data Analysis

3.2.1 X-ray Data Reduction

Chandra X-ray observations 4969 and 4970 were processed using CIAO version 4.0.1 and version 3.4.5 of the calibration database. Background flares were excluded using standard filtering, yielding a net exposure time of 182 ks. Time-dependent gain and charge transfer inefficiency corrections were applied. Blank-sky background files used for background subtraction were normalized to the source count rate in the 9.5 - 12 keV band.

3.2.2 Metallicity Profile Along the Jets

We have searched for a metal-enriched outflow by comparing the radial distribution of iron along and orthogonal to the radio jets and lobes. Guided by the cavity system and 330 MHz radio emission shown in Figure 3.1, we have defined sectors parallel to and roughly orthogonal to the jets. The northern sector located between 90 and 155 degrees, measured counterclockwise from west, was divided into five radial bins with minimum signal-to-noise of 210. Two regions east and west of the northern jet were created with 45 degree opening angles and bin sizes matching those of the northern sector. These regions are outlined in Figure 3.1. The spectrum for each bin was extracted and corresponding event-weighted response matrices were computed. Using XSPEC (Arnaud, 1996), single temperature plasma models with absorption (WABS×MEKAL) were fit to the spectra in the energy

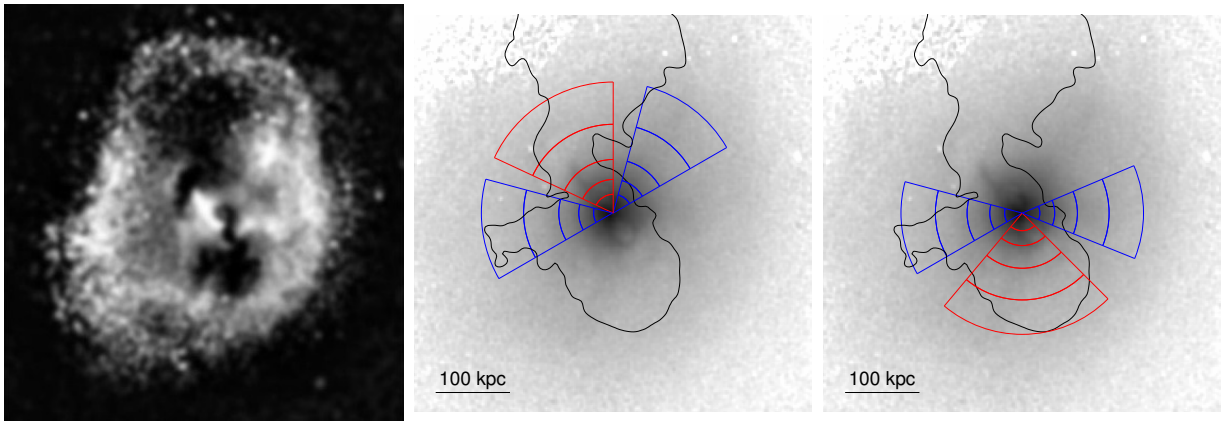

Figure 3.1: *First panel*: Residual map of the beta model subtracted surface brightness image from Wise et al. (2007). North is towards the top, east is towards the left. *Second panel*: Combined, adaptively smoothed image of Hydra A. The black contour outlines the 330 MHz radio emission. The red regions are where the spectra were extracted along the northern jet and the blue regions are where the off-axis spectra was extracted. Each bin contains at least 44000 counts. *Third panel*: Same as the second panel, but for the southern jet.

range 0.5 to 7 keV. The column density was frozen at the Galactic value of 4.94×10^{20} cm^{-2} (Dickey & Lockman, 1990). Temperatures, abundances, and normalizations were allowed to vary, while the abundance ratios were set to the the solar photospheric values of Grevesse & Sauval (1998). The spectra are very well fitted by this model.

The projected metallicity profiles along and orthogonal to the northern jet are shown in the upper panel of Figure 3.2. Between radii of $\sim$ 20 kpc and 120 kpc the metal abundance of the hot gas is enhanced by up to 0.2 dex along the jet relative to the orthogonal sectors. Metallicities for the inner and outermost bins are indistinguishable between the on and off jet sectors.

The southern sector is located between 230 and 315 degrees counterclockwise from west. The metallicity profiles along and orthogonal to the southern jet are shown in the lower panel of Figure 3.2. A metallicity enhancement is also found to the south, extending to approximately 120 kpc. The lower points in Figure 3.2 shown as triangles represent the orthogonal sectors and are interpreted as the undisturbed metallicity gradient. The gas in the undisturbed regions is warmer by up to 0.5 keV compared to the jet regions.

The metallicity enhancement could be affected by the presence of cooler gas. To explore this, we have considered a second temperature component when fitting the regions along the jets. For example, a component with a temperature between 0.5 and 0.7 keV in each sector would increase the abundances by approximately 15%, but would contribute at most 2% to the total emission. However, this and other similar models do not significantly improve the spectral fit. If such an extended cool component were present, it would have the effect of increasing the metal enhancements shown in Figure 3.2 by roughly 0.1 dex.

3.2.3 Metallicity Map

The abundance map shown in Figure 3.3 was created using a weighted Voronoi tessellation binning algorithm (Cappellari & Copin, 2003; Diehl & Statler, 2006). Each bin has a S/N of 150 and was chosen to balance the uncertainties on the best-fit abundances while preserving the excellent spatial resolution afforded by the large number of source counts. For each bin, a spectrum was extracted using the procedure described in Section 3.2.2. The spectrum from each bin was fitted in the energy range 0.5-7.0 keV with an absorbed single temperature MEKAL thermal plasma model using the parameters defined previously in Section 3.2.2.

The highest metallicity gas, shown in yellow in Figure 3.3, extends to the north-east and south of the nucleus. This gas is closely aligned with the radio emission and is consistent with the metallicity excesses shown in Figure 3.2. The temperature along the north-east

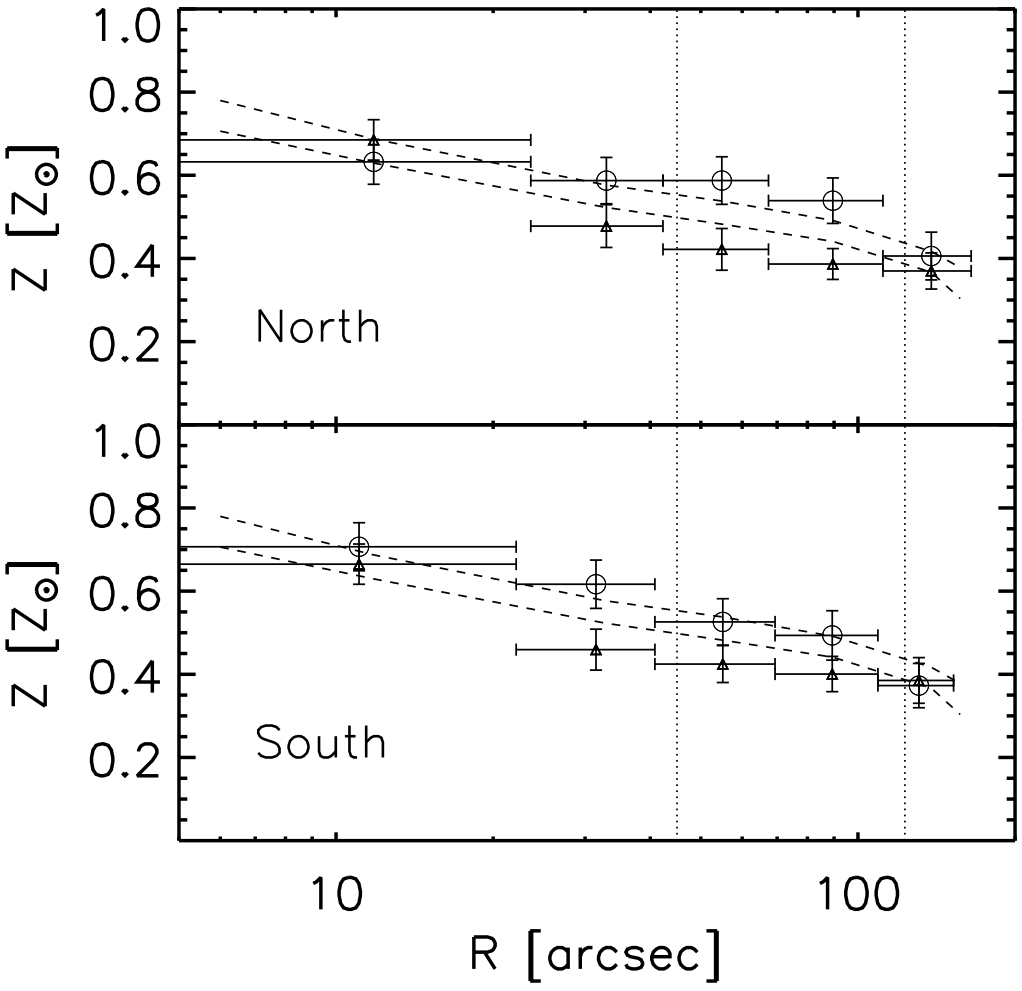

Figure 3.2: Projected metallicity profiles for Hydra A. The circles represent regions along the jets and triangles are the average fits to the regions east and west of each jet. The dashed lines represent the aximuthally-averaged metallicity profile. The left vertical dotted lines indicate the outer edges of the cavity pairs A and B from Wise et al. (2007), and the right dotted line is for cavity pair C and D.

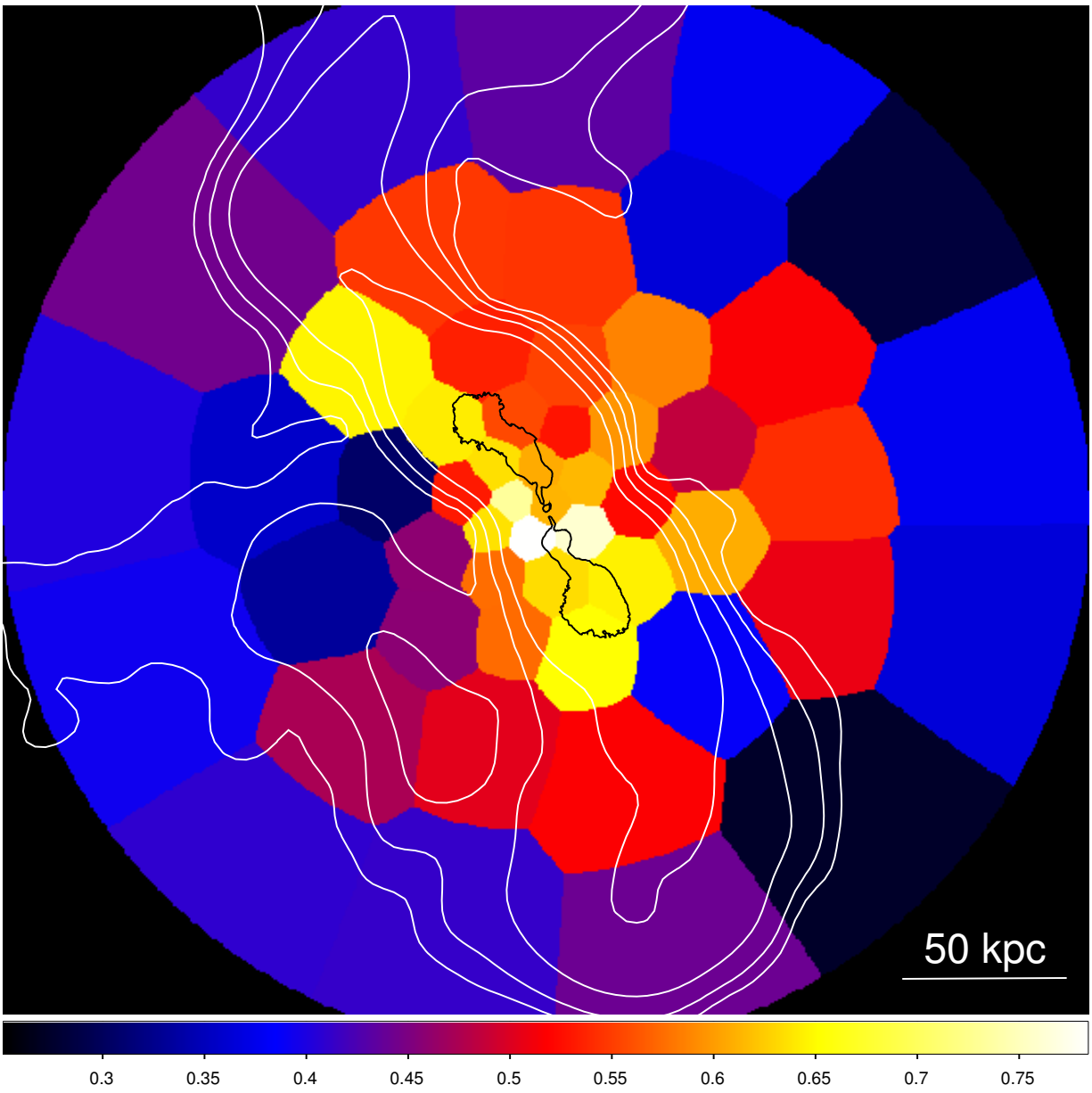

Figure 3.3: Metallicity map showing the central 5' × 5' of Hydra A. Each bin contains approximately 22500 counts. Brighter regions represent a higher metallicity. The average error per bin is approximately 18%. The 330 MHz emission is shown by the white contours and the 1400 MHz emission is shown by the black contours.

jet is approximately 2.7 keV, and the southern jet is found to be approximately 3.1 keV. The surrounding region has a temperature that ranges between 3.4 keV and 3.8 keV. This is similar to what was found in the *XMM* analysis by Simionescu et al. (2009). A plume of gas with a modest metallicity enhancement of ~ 0.1 $Z/Z_{\odot}$, shown in orange, can be seen extending north-west along an X-ray filament. Though it is located within what we have defined as the undisturbed region described in Section 3.2.2, it has a negligible effect on our analysis.

3.3 Discussion

3.3.1 Iron Mass

We estimate the excess iron mass in two regions. First, we assume the metal-enriched gas fills the entirety of the on-jet regions defined in Figure 3.1. Second, we consider only the most significant iron excess shown in yellow in Figure 3.3. We consider both regions because the mass estimate depends critically on the volumes and filling factors (which we assume to be unity) of the metal-enhanced regions. The uncertainty associated with these quantities should be smaller in the yellow region alone. At the same time, the true enhancement must be larger as it is indeed spread over a large volume. We compute the iron mass as

$$M_{\rm Fe} = \rho V Z f_{\rm Fe,\odot}, \tag{3.1}$$

where Z is the metallicity of the gas, $f_{\rm Fe,\odot}$ is the iron mass fraction of the Sun, V is the volume, and ρ is the density of the gas assuming $n_{\rm e} = 1.2 n_{\rm H}$. The density was calculated from the deprojection of the surface brightness profile along the jets assuming the volumes of the semi-annular wedges shown in Figure 3.1.

For the first case the difference between the iron mass along the jet and the iron mass of the underlying metal distribution in equal volumes is plotted in Figure 3.4 for both north and south regions. A significant excess is seen in the second, third, and fourth bins along both jets. The total volume of these bins combined is 4.1×10^{70} cm^3. We find a total excess iron mass of $3.2^{+1.1}_{-1.0} \times 10^7$ M$_\odot$ along the northern jet and $3.6^{+1.9}_{-1.6} \times 10^7$ M$_\odot$ along the southern jet. These values are consistent with the upper limit found by Simionescu et al. (2009).

In our second case, the volumes of the regions are approximated as cylinders extending from 15 kpc outside the nucleus to a radius of 100 kpc, with an approximate width of 25 kpc. Their total volume is 2.7×10^{69} cm^3. After subtracting the average metallicity of the

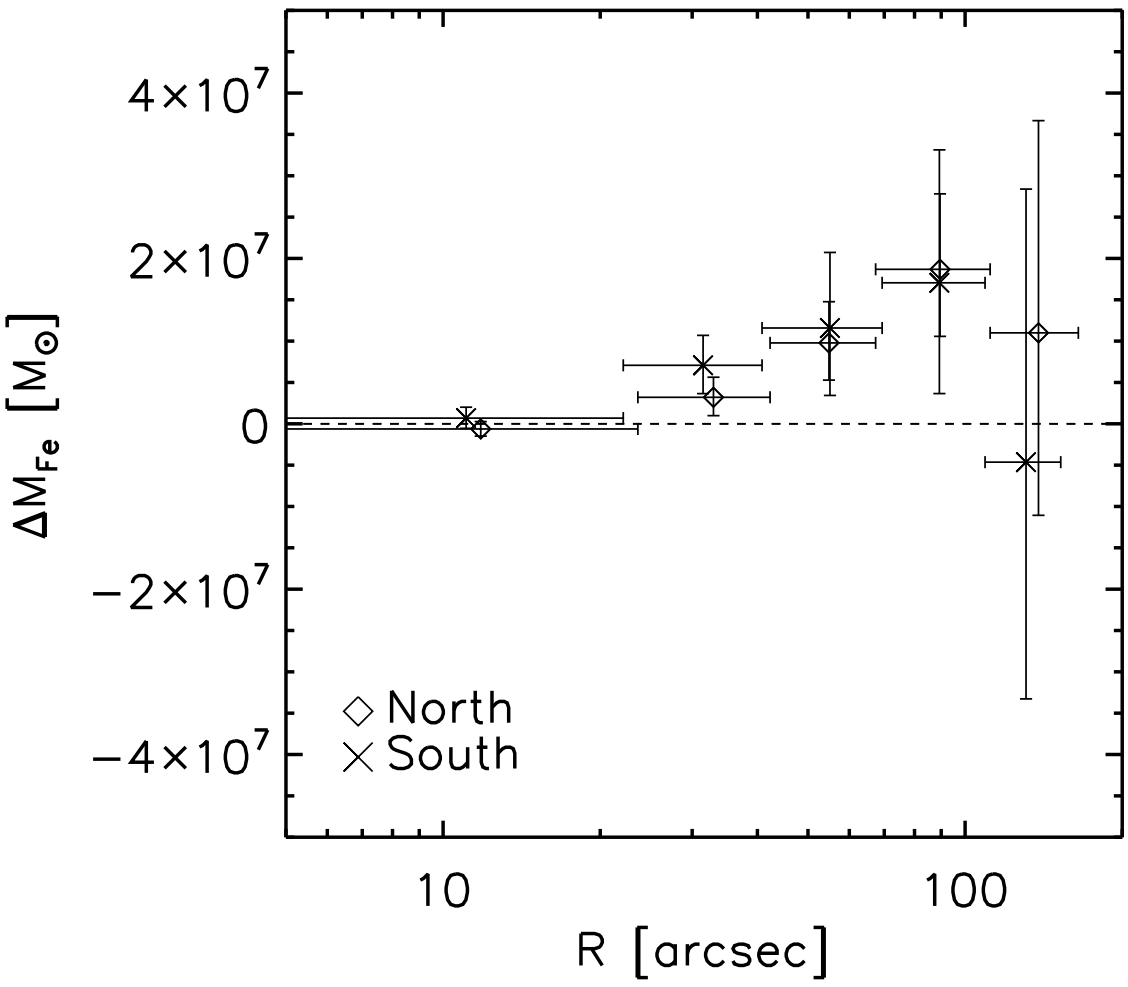

Figure 3.4: The diamond points represent the excess iron mass along the northern jet compared to the global profile. The cross points represent the excess iron mass along the southern jet. Only the second, third, and fourth bins show a significant excess.

undisturbed background 0.42 $Z/Z_{\odot}$, we estimate the excess iron mass within the yellow region in Figure 3.3 to be $\sim 1.6 \times 10^7$ $M_{\odot}$.

The excesses iron mass represents a significant fraction of the total iron mass in the gas surrounding the BCG. The total iron mass measured within a 30 kpc radius is $1.61^{+0.60}_{-0.52} \times 10^8$ $M_{\odot}$, consistent with the value in both David et al. (2001) and Simionescu et al. (2009). Assuming the the excess iron originated at the center of the cluster, this implies that $\sim$ 10% - 30% of the iron originating from this central region has been displaced along the jets.

Using the relationship of Böhringer et al. (2004), we estimate the time required to replenish the lost iron through SNe Ia and stellar mass loss as,

$$t_{\rm enr} = \left(10^{-12} S \eta_{\rm Fe} + 2.5 \times 10^{-11} \gamma_{\rm Fe}\right)^{-1} \frac{M_{\rm Fe} L_{\rm B\odot}}{L_{\rm B}}. \tag{3.2}$$

Here, $\eta_{\rm Fe} = 0.7$ $M_{\odot}$ is the iron yield from SN Ia and $\gamma_{\rm Fe} = 2.8 \times 10^{-3}$ is the iron mass fraction from stellar mass loss. With a B-band luminosity of $L_B = 9.2 \times 10^{10}$ $L_{\odot}$ (David et al., 2001) and a supernova rate of $S = 0.15$ SNU (Cappellaro et al., 1999), the enrichment time required to replace the uplifted iron is approximately 0.2 - 0.7 Gyr. The enrichment time is a small fraction of the age of the cluster and is only two to seven times larger than the age of the outburst that created the surrounding shock front. Thus, the central metallicity peak would recover if the AGN becomes dormant for a period of only a few times its current age.

Because some star formation is occurring in the BCG, we have also considered the contribution from SN II enrichment. Assuming one supernova per 100 solar masses of stars produced and a star formation rate of 1 - 5 $M_{\odot}$ yr^{-1} (McNamara, 1995) in the BCG, we find only 3% of the total iron mass is expected to originate from SN II enrichment over this time-scale.

3.3.2 Outflow Energy

The fraction of the AGN outburst energy required to lift the enriched gas to its present position provides a lower limit to the AGN energy deposited into the high metallicity gas near the BCG. This value can be estimated by calculating the difference in gravitational potential energy between the original position of the uplifted gas and its current position. Following Reynolds et al. (2008), we calculate this quantity as,

$$\Delta E = \frac{M c_{\rm s}^2}{\gamma} \ln\left(\frac{\rho_i}{\rho_f}\right), \tag{3.3}$$

where the sound speed is $c_s \approx 750$ km s^{-1}, ρ_i and ρ_f are the initial and final densities of the surrounding ICM and $\gamma = 5/3$ is the ratio of specific heat capacities. Assuming all of the displaced gas was initially at the center of the cluster, the energy required to lift the metal-enriched gas lies between 0.5 - 5×10^{59} erg. This figure is comparable to the work required to inflate the inner cavities against the surrounding pressure (Wise et al., 2007) and is between 1% and 5% of the total energy expended by all of the cavities and the surrounding shock front. This analysis suggests that lower power AGN outbursts typically observed in clusters (McNamara & Nulsen, 2007) would have a minor impact on their metallicity distributions.

3.4 Conclusions

Hydra A has undergone a major AGN outburst that has transported 2 - 7×10^7 $M_\odot$ of metal-enriched gas out of the BCG along the radio jets. The gas has been enhanced by up to 0.2 dex in metallicity compared to the ambient gas out to distances as large as 120 kpc. Approximately 10^{59} erg was expended while uplifting the metal-enriched gas, which is 1% to 5% of the total AGN outburst energy.

Chapter 4

Correlation Between AGN Outbursts and Anisotropic Metal-Enriched Outflows

4.1 Introduction

A hot, diffuse plasma composed primarily of hydrogen and helium and enriched in heavy elements fills the space in and between the galaxies in rich clusters. Chemical enrichment of the intracluster medium (ICM) is thought to have occurred early, primarily by type II supernova explosions. The supernova ejecta raised the heavy element abundance of the ICM to an average of approximately 1/3 of the solar value (Mushotzky et al., 1996; Mushotzky & Loewenstein, 1997). Exceptions are found near brightest cluster galaxies (BCGs) located at the centers of cool core (cooling flow) clusters. The heavy element abundances there often rise to values approaching the mean metallicity of the Sun (Allen & Fabian, 1998; Dupke & White, 2000; De Grandi & Molendi, 2001). Furthermore, the iron abundance in cool cores is usually enhanced with respect to the α-elements. Because the α elements are produced primarily by core collapse supernovae, while iron is produced primarily by type Ia supernovae, the gas in cool cores has probably been enriched relative to the ICM by the stars associated with the BCGs (De Grandi et al., 2004; Tamura et al., 2004).

Several studies have shown that the radial distributions of type Ia ejecta extend to larger radii than the stellar light profiles of BCGs (Rebusco et al., 2005, 2006; David & Nulsen, 2008; Rasera et al., 2008). Assuming the ejecta was produced by the stars, the

profiles imply that the ejecta is being displaced from the galaxies by some mechanism. Turbulence induced by cluster mergers or outflows from active galactic nuclei (AGN) are likely possibilities (Sharma et al., 2009). BCGs often host radio AGN that are interacting with the hot, metal-rich gas by forming cavity systems and shock fronts (see McNamara & Nulsen, 2007, for review). The cavity systems in the objects discussed here have displaced between $10^{10} M_{\odot}$ and $10^{12} M_{\odot}$ of gas. The dynamical forces associated with them may also be able to drive the metal-enriched gas out of the BCG and into the ICM in outflows oriented along the radio jet (Gopal-Krishna & Wiita, 2001, 2003; Brüggen & Kaiser, 2002; Omma et al., 2004; Moll et al., 2007; Roediger et al., 2007; Pope et al., 2010).

Recent studies of some clusters have identified gas with unusually high metallicity beyond the cores and along the radio lobes (Simionescu et al., 2008, 2009; Kirkpatrick et al., 2009a; O'Sullivan et al., 2011). The gas along the radio lobes is, in some cases, enhanced in metallicity by up to 0.2 dex relative to the surrounding gas. These metal-rich inclusions indicate that the cool, metal-rich material originating from the BCG is mixing with lower metallicity gas lying at larger radii. It is still unclear how general this phenomenon is, and how these outflows scale with the properties of the host AGN. A systematic analysis of a large sample of X-ray clusters with a range in AGN jet power is needed to definitively explore this phenomenon.

Here, we show that AGN are driving metals out of BCGs to very large distances. We have performed our analysis using deep, high-resolution X-ray images of 10 clusters drawn from the *Chandra X-ray Observatory* archive. We report on the discovery of a significant trend between jet power and the radial extent of uplifted, metal-enriched gas, and we briefly discuss its consequences. Throughout this chapter we assume a ΛCDM cosmology with $\mathrm{H_0} = 70$ km s^{-1} Mpc^{-1}, $\Omega_{\mathrm{M}} = 0.3$, and $\Omega_{\Lambda} = 0.7$. All uncertainties are quoted at the 67% confidence level.

4.2 Cluster Sample

We examine 10 clusters selected from the Bîrzan et al. (2004), Rafferty et al. (2006) and Diehl et al. (2008) samples of clusters with prominent cavity systems. The 10 clusters span a broad range of jet (cavity) power. The sample includes clusters having *Chandra* images that are deep enough to generate metallicity maps with a resolution of at least 25 bins with a minimum signal-to-noise ratio (S/N) of 100 per bin. Our goal is to make high precision measurements of the projected metallicity distribution while maintaining a spatial resolution that optimizes the measurement of the spatial distribution of the high metallicity gas for comparison to the radio sources. The clusters that meet these criteria are A133,

A262, Perseus, MS0735.6+7421, Hydra A, M87, A1835, A2029, A2199, and A2597. Each cluster observation was processed using version 4.1.2 of CIAO and the calibration database. Background flares were excluded using standard filtering techniques, and point sources were identified in the combined image of each cluster using *wavedetect*, and removed. Blank-sky background files were normalized to the source count rate in the 9.5-12 keV band.

4.3 Analysis

4.3.1 Metallicity Maps and Profiles

We present example metallicity maps for three clusters (A262, Hydra A, A1835) in Figure 4.1. The combined exposures for each cluster were binned using a weighted Voronoi tessellation algorithm (Cappellari & Copin, 2003; Diehl & Statler, 2006). With approximately 10,000 net counts or greater per bin, spectra were extracted and weighted response matrices were created using standard CIAO routines. A single temperature plasma model with absorption (WABS×MEKAL) was fit over the energy range 0.5-7 keV. Temperature, abundance, and normalization were allowed to vary with the column density frozen at the values quoted by Dickey & Lockman (1990). The internal ratio between metals was set to the solar photospheric values of Grevesse & Sauval (1998). Allowing the α-elements to vary independently does not show any significant effect on the outcome of the iron abundance measurement, therefore we have chosen to use the simple model. The spectra are reasonably well fit by the single temperature model, with the exception of the central region of A262. This region is better fit with a multi-temperature model which finds a higher central metallicity value (see Kirkpatrick et al., 2009b). However, this does not affect the interpretation of our results as the central regions of the clusters are not important for this analysis.

Metallicity profiles have been measured for each cluster. Spectra were extracted from regions occupied by radio emission and/or cavities in semi-annular-shaped bins. Each bin size was determined by requiring a minimum S/N of 140, which achieves uncertainties of approximately 0.05 $Z_{\odot}$. A high S/N ratio is required to find deviations between the profiles along and orthogonal to the radio cavity system. These orthogonal profiles, which we consider to represent the undisturbed region of the cluster, are extracted using the same bin width as the radio cavity system profile. The S/N for these regions is usually greater than 140 due to larger angular sizes. All profiles are fit using the same model as the two-dimensional analysis.

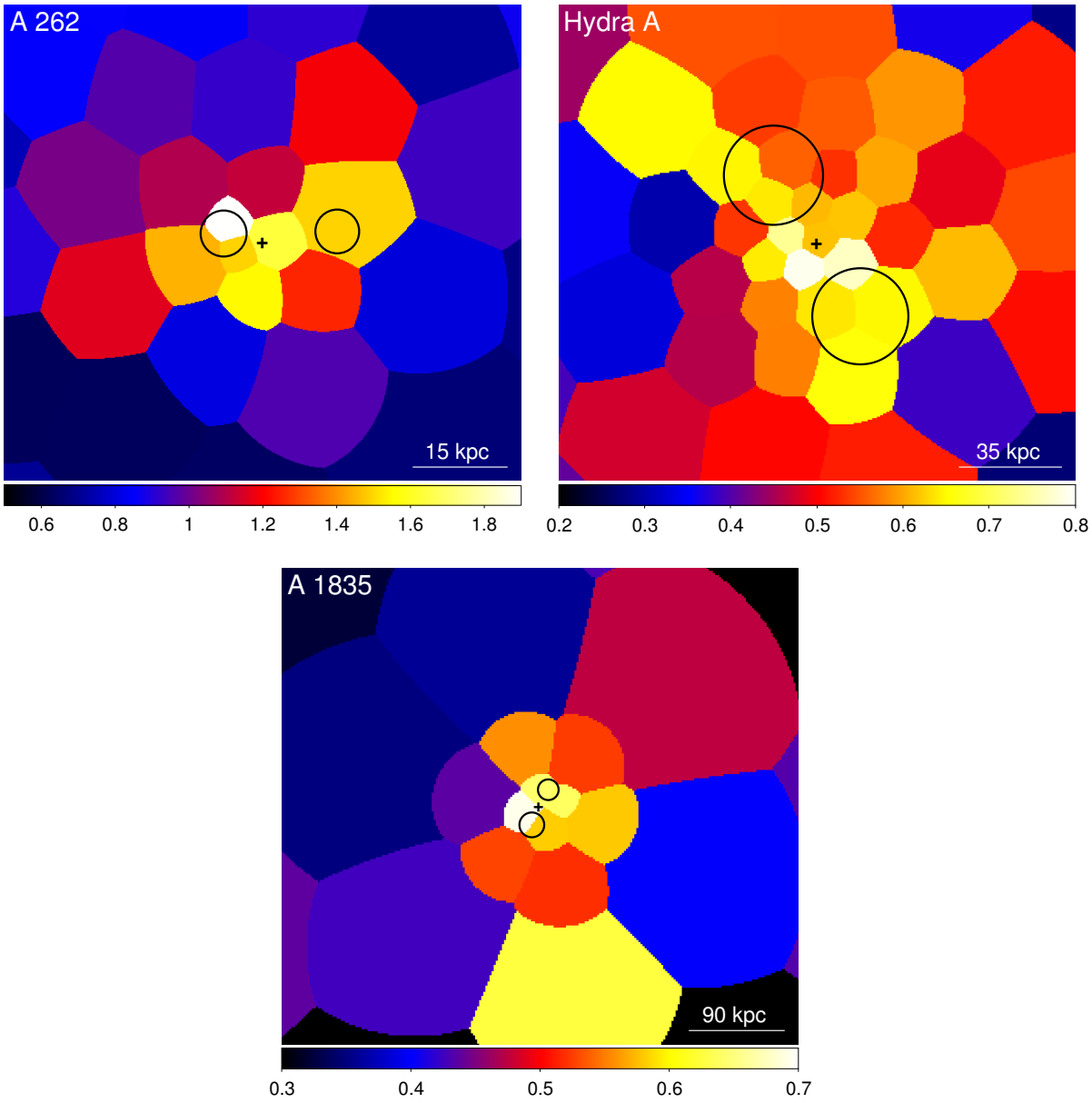

Figure 4.1: Three panels show the metallicity maps for clusters A262, Hydra A, and A1835, respectively. In all three cases, high metallicity gas (shown in yellow) extends outward along the same axis of the cavity system (approximate size and location indicated by black circles). The black crosses indicate the approximate cluster centers.

4.3.2 $P_{\rm jet} - R_{\rm Fe}$ Scaling Relation

The radial profiles for A262, Hydra A, and A1835 are presented in Figure 4.2. The red squares represent the metallicity of the radio cavity system and the blue triangles represent the undisturbed metallicity profile. The dotted vertical line indicates the maximum radius at which a significant enhancement in metallicity has been detected. We refer to this as the iron radius ($R_{\rm Fe}$). This radius is concisely defined as the location of the radial bin furthest from the cluster center where the 1σ error bars of the profiles along and orthogonal to the radio axis do not overlap. The errors on $R_{\rm Fe}$ are the width of the bin. Regions interior to the iron radius show a systematic enhancement in iron abundance over the undisturbed regions. For regions beyond the iron radius, the abundance profiles are indistinguishable. From top to bottom, the three panels are arranged in order of increasing jet power and increasing iron radius. This shows that higher power AGN are able to launch metal-enriched gas to greater distances.

In Figure 4.3, the iron radius is plotted against jet power derived using X-ray cavity data taken from Rafferty et al. (2006) for all 10 clusters in the sample. The powers quoted there were derived from the total energy of the cavities, $4pV$, and their buoyant rise time. In systems with multiple generations of cavities, the average power is used. Note that the iron radius was determined using the radial metallicity profiles only and not using the metallicity maps. A trend between jet power and iron radius is evident over three decades in jet power. The low powered AGN outbursts $P_{\rm jet} \simeq 10^{43}$ erg s^{-1} drive out material on a scale of a few tens of kiloparsecs. For exceptionally large outbursts with jet power exceeding 10^{46} erg s^{-1}, such as MS0735, metals from the core are being launched hundreds of kiloparsecs into the ICM.

To quantify this trend, we fit a linear function to the logarithms of jet power and iron radius. Performing a least-squares regression, the best fit plotted in Figure 4.3 takes the form

$$R_{\rm Fe} = 58 \times P_{\rm jet}^{0.42}\ ({\rm kpc}), \tag{4.1}$$

where jet power is in units of 10^{44} erg s^{-1}. The rms scatter about the fit is approximately 0.5 dex. The correlation is strong and shows a fairly small scatter, although with only 10 objects the true scatter about the mean is difficult to evaluate. The scatter will likely increase with the inclusion of additional clusters, which will be addressed in a future paper.

A spurious correlation between iron radius and jet power, which depends on the volume of the cavities, could arise due to the dependence of distance on both the linear diameter of the cavity systems and the iron radius. This does not appear to be the case. The clusters we considered here all have been exposed deeply with *Chandra*. We could have easily

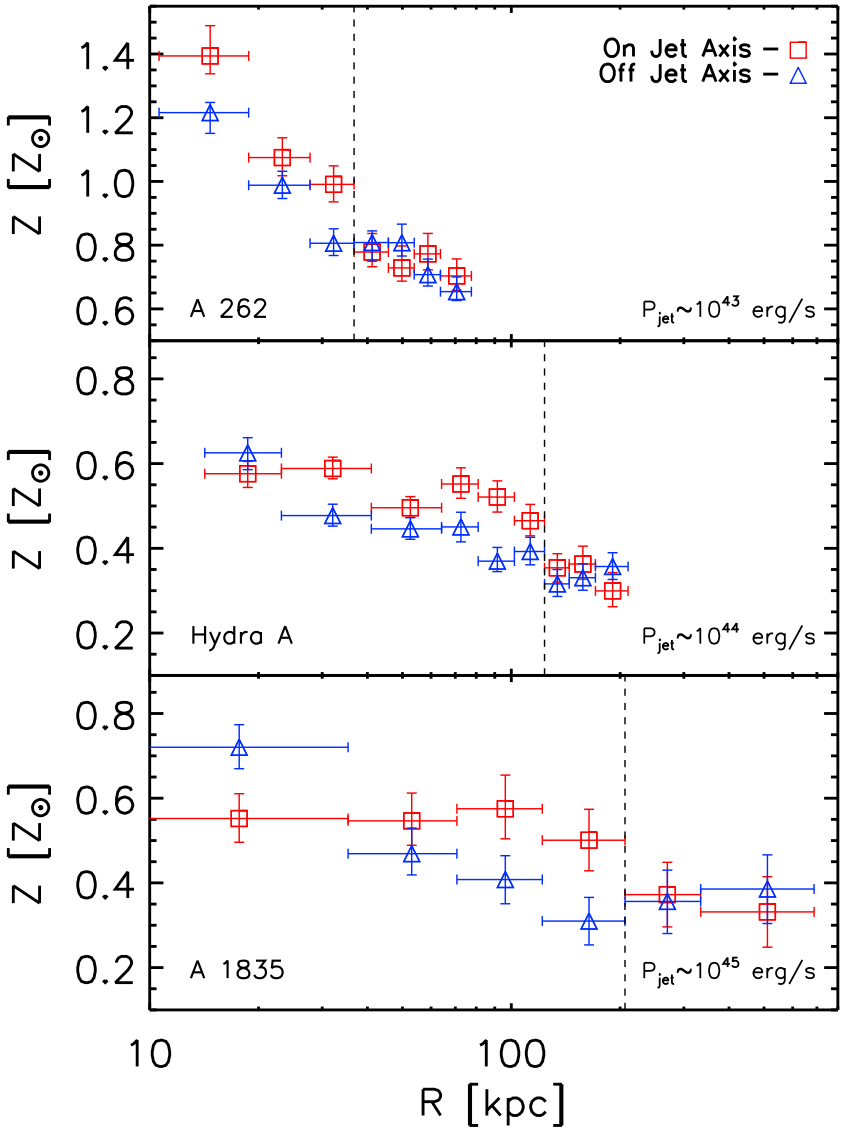

Figure 4.2: Each panel represents metallicity profiles along and orthogonal to the radio axis for each cluster. The red square points represent the metallicity along the axis of the radio cavity system, and the blue triangular points represent the undisturbed region of each cluster. The dashed vertical line represents the iron radius.

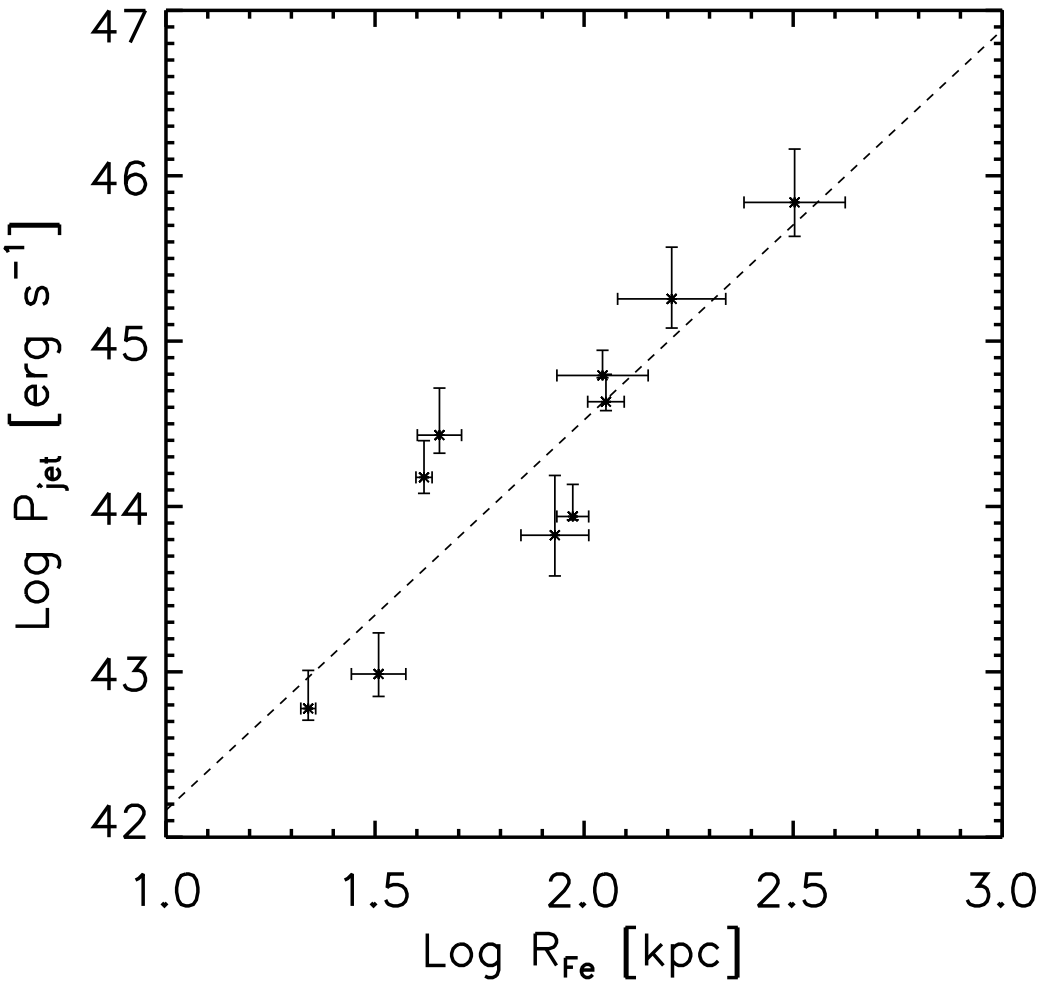

Figure 4.3: Jet power vs. iron radius. The dashed line is the best fit to the data.

detected cool, metal-rich gas on all spatial scales of interest here, and at random angles with respect to the cavities and radio sources. Hydra A, for example, has a complex cavity system that was created by at least three separate outbursts or a continuous outburst that has persisted for several hundred million years (Wise et al., 2007). The cavity systems considered separately have similar jet powers, but their centers lie at very different radii between 25 kpc and 250 kpc. Nevertheless, Hydra A does not deviate significantly from the trend in Figure 4.3, implying that the measured iron radius is not a simple function of cavity size alone. In Figure 4.4, we have plotted the inner cavity position for all clusters in our sample versus the iron radius. In all cases, the iron radius lies beyond the inner cavities. This shows that the metallicity outflows are not simply tracing the current generation of AGN activity, but are maintained over multiple generations. The iron radius may provide a reliable indicator of average jet power in a cluster where cavity power measurements are ambiguous.

There are uncorrected systematic uncertainties in Figure 4.3. We have made no attempt to measure the additional power associated with shock fronts and faint ghost cavity systems, which would be difficult to do for the entire sample. The total jet power for objects such as MS0735 and Hydra A, which have detected shock fronts at high significance, is under reported here by roughly a factor of two (see McNamara & Nulsen 2007 for a discussion). Including energy from the shocks affects the slope of the fit by $\sim 20\%$. We chose not to boost the power of these systems to avoid biasing them with respect to other systems. Thus, only cavity power is given here for consistency. In addition, the iron radii given here are projected values. Their true values may be underestimated in extreme cases by roughly a factor of two, but typically by a few tens of percent. Errors of this size will not change our basic result. We intend to explore these issues in a future paper.

4.3.3 Alignment Between Metal Enhancements and the Radio Orientation

We find that the high-metallicity gas outflow regions are spatially aligned with the radio and X-ray cavity systems. Using the metallicity maps, we have independently measured the angle on the sky with respect to the center of the cluster of the high metallicity gas outside of the cluster core. We have also measured the mean position angle of the cavity system. The position angle was measured using unsharp masks of each cluster in order to estimate the locations of the centers of the cavities. Finally, the angle of the extended radio emission was determined for those systems with resolved radio imagery. Using 330 MHz images, the radio angle was determined by bisecting the radio emission on either side

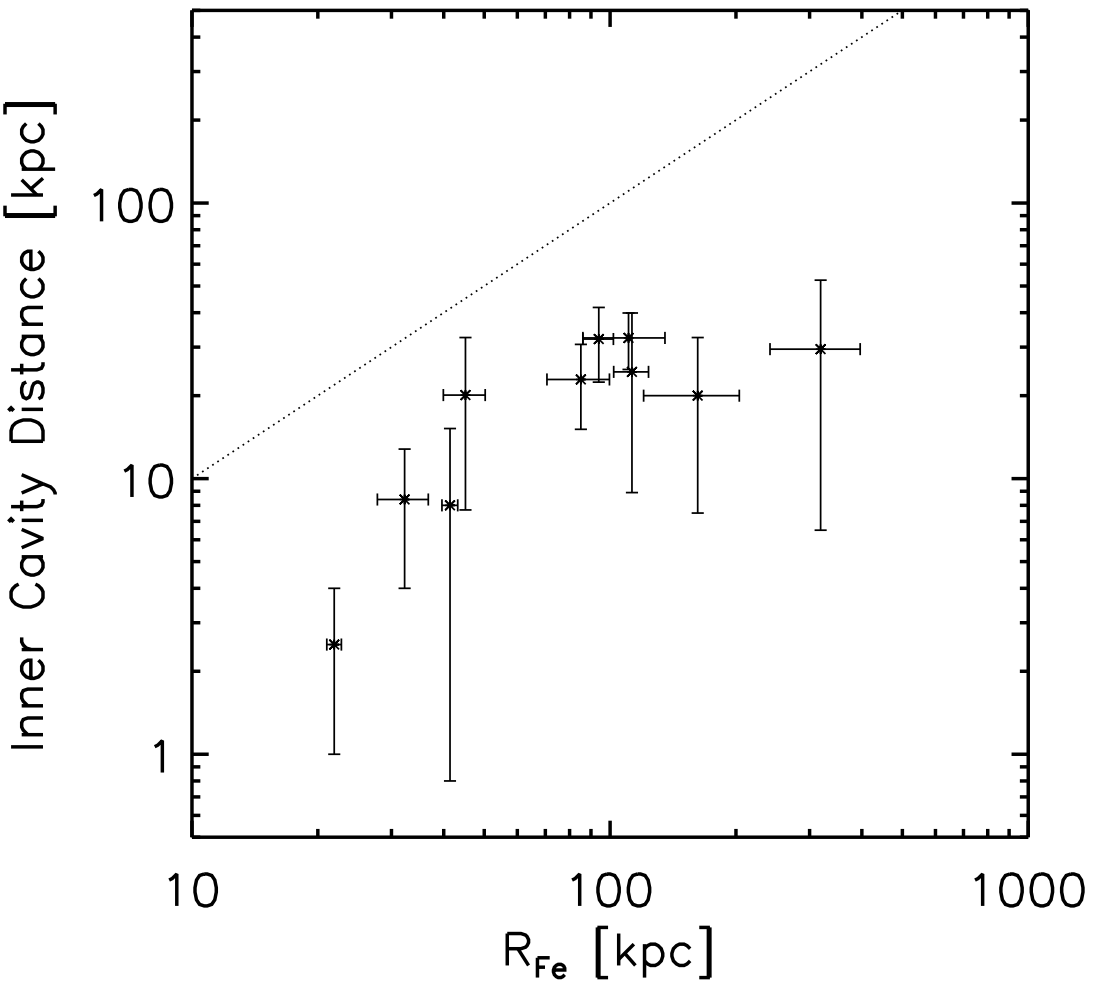

Figure 4.4: Radius of the innermost cavity of each cluster is plotted against the iron radius. The points represent the cavity center and the vertical error bars indicate the radius of the cavity. The dotted line of equality is also plotted.

of the nucleus of the BCG. We have plotted metal angle versus cavity center (blue squares) and radio angle (red diamonds) in Figure 4.5. Both sets of points are consistent with the dashed line of equality. In clusters with calculated radio angles, all three quantities are in excellent agreement with one another.

4.3.4 Comparison to Independent Metallicity Measurements and to Simulations

Independent reports of metal enriched outflows are consistent with the trend shown in Figure 4.3. For example, the radial abundance effect is seen in a relatively low S/N metallicity map of the poor cluster AWM 4 (O'Sullivan et al., 2010, 2011). This study found metal-enriched gas extending along the radio jets from the nucleus of the BCG to a radius of 35 kpc. With a jet power of approximately 2×10^{43} erg s^{-1}, our scaling relation predicts an iron radius of 25 kpc. This result lies within one standard deviation of our relationship.

Recent simulations of AGN outflows have shown that radio jets are expected to advect ambient material and launch it into the ICM (e.g., Pope et al., 2010). Using a three-dimensional AMR hydrodynamical code, Gaspari et al. (2011) found in their simulations that jets are able to transport metal-rich gas from the cores of clusters into the ICM. Their simulated jet power of approximately 5.7×10^{44} erg s^{-1} lifted gas 200 kpc from the center before it mixed with the surrounding metal-poor gas. The simulation overpredicts the iron radius by a factor of 1.6 compared to our scaling relation, which represents about a 1σ deviation from our relationship.

Using a series of three-dimensional hydrodynamical jet simulations centered in a realistic, non-static atmosphere, Morsony et al. (2010) have evaluated the spatial impact of radio jets on the hot ICM as a function of jet power. They refer to this as the radial "sphere of influence" of the jet, which we compare to our iron radius. They find that the sphere of influence scales with jet power as $R \propto L_{\rm jet}^{1/3}$. This dependence on jet power is somewhat shallower than ours. However, the rough agreement between our observed scaling relation and their simulations is encouraging.

4.4 Summary and Discussion

We have shown that metal-rich gas is being transported outward by AGN in all 10 clusters in our sample. In each case, the metallicity enhancements found in the maps are closely aligned with the radio and cavity systems. We find a significant trend between jet power

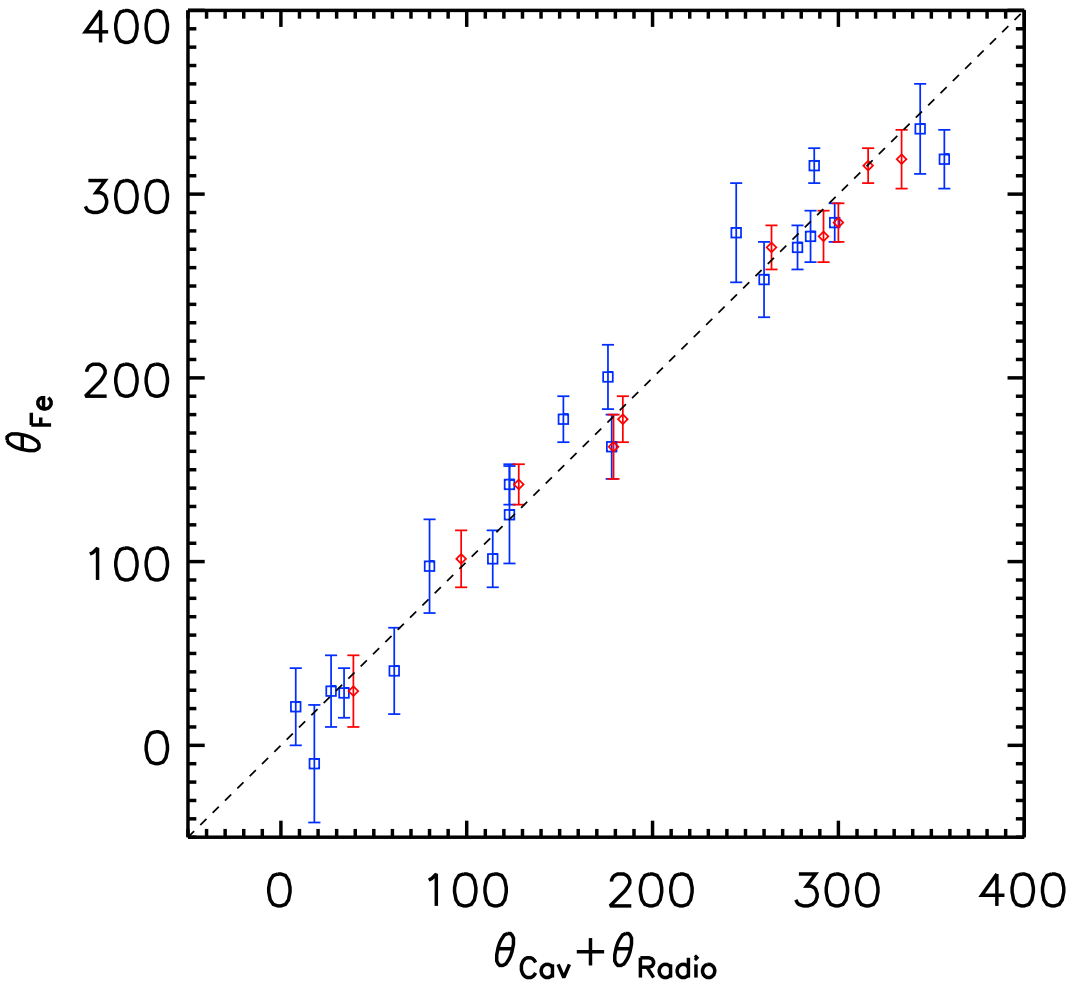

Figure 4.5: Angle of metal enhanced gas vs. cavity angle and radio emission angle. The blue squares represent angle on the sky with respect to the center of the cavity. Where high resolution data are available, the radio angle (330 MHz radio emission) is represented by red diamonds. Blue and red points located at the same $\theta_{\rm Fe}$ highlight the difference in cavity and jet angle in the same cluster. The dashed line represents the line of equality.

and iron radius, with a power-law scaling as $R_{\rm Fe} \propto P_{\rm jet}^{0.42}$. This scaling relation shows that AGN play an important role in dispersing metals throughout the cores of clusters. A comparison between our scaling relation and recent hydrodynamical simulations discussed in the literature shows encouraging agreement. A detailed comparison between observed and simulated outflows shows strong potential to place interesting constraints on jet physics.

Simulations of cluster assembly seem to require outflows in order to spread metals throughout the cores of clusters (Fabjan et al., 2010; Barai et al., 2011). Major mergers at early times are efficient at distributing gas throughout the ICM (Burns et al., 2008), but recent studies show in cool core clusters, sloshing due to mergers alone cannot explain at later times the large radial extent (i.e., $\geq$ 100 kpc) of metallicity peaks (Roediger et al., 2010). A simple extrapolation of our scaling relation to a higher jet power indicates that AGN exceeding 10^{47} erg s^{-1} would be required to drive metals beyond 1 Mpc, which is a cosmologically interesting regime. Mechanical jet powers of this magnitude have not been observed in clusters, although quasars radiating above 10^{47} erg s^{-1} have been observed in the centers of a few cool core clusters (e.g., Russell et al., 2010). Achieving mechanical jet powers of this magnitude requires accretion rates of several tens of solar masses per year onto a nuclear black hole. At the same time, mechanically dominant AGN are expected to occur in radiatively inefficient inflows accreting below a few percent of the Eddington rate (Narayan & McClintock, 2008). Therefore, achieving such powerful mechanical outflows would be exceedingly difficult unless the host galaxies harbor black holes with masses significantly in excess of $10^9 M_\odot$, which are expected to be rare. This may explain why the metallicity enhancements at the centers of clusters extend several hundred kpc beyond the BCG and generally not to 1 Mpc.

Chapter 5

AGN as a Mechanism for Distributing All Metal-Rich Gas in the ICM

5.1 Introduction

Brightest cluster galaxies (BCGs) at the centers of cool core clusters play a major role in the evolution of the intracluster medium (ICM). The existence of BCGs is due to a massive feedback loop of hot, X-ray gas emitting its energy away through line cooling, eventually fueling star formation and the supermassive black hole (SMBH) at the center (Johnstone et al., 1987; McNamara & O'Connell, 1989; Fabian, 1994; Crawford et al., 1995, 1999; Cardiel et al., 1998; Edge et al., 2002; Salomé & Combes, 2003; Rafferty et al., 2006; Donahue et al., 2007; Edwards et al., 2007; Bildfell et al., 2008; O'Dea et al., 2008; Rafferty et al., 2008; Cavagnolo et al., 2008; Voit et al., 2008; Soker, 2008). The presence of a massive BCG also alters the chemical composition of the ICM. For a typical galaxy cluster, the mean metallicity is approximately 1/3 of the solar value (Mushotzky et al., 1996; Mushotzky & Loewenstein, 1997). Enrichment occurs early in the evolution of a cluster, primarily through ejecta from core-collapse supernovae (SNe II) associated with massive star formation in the member galaxies. The enrichment throughout the cluster is fairly uniform, in most cases decreasing slightly with radius. This is not the case when a cluster has a BCG. The gas surrounding a BCG is known to be enriched in heavy elements approaching the mean metallicity of the Sun (Allen & Fabian, 1998; Dupke & White, 2000; De Grandi & Molendi, 2001). The BCG enriches cluster cores primarily by type Ia

supernovae (SN Ia), a process known for generating greater quantities of iron compared to SN II (De Grandi et al., 2004; Tamura et al., 2004). A dichotomy therefore exists between the α-element enhanced outskirts and the iron enhanced core.

The iron-enhanced ejecta is being produced by the stars of the BCG, so it is expected that stellar light profiles and metallicity profiles would match accordingly. Several studies have shown that the radial distribution of iron in cool core galaxies extends to radii a few times larger than the stellar light Rebusco et al. (2005, 2006); David & Nulsen (2008); Rasera et al. (2008). AGN and mergers are prime candidates for driving the distribution of metals beyond the stars of the BCG. AGN are a common occurrence in BCGs and are already known for displacing the ICM by inflating cavities and generating shock fronts (for a review, see McNamara & Nulsen, 2007). Entraining large quantities of cool, metal-enriched gas through the injection of radio jets into the ICM has been seen to potentially produce outflows of enriched gas (Gopal-Krishna & Wiita, 2001, 2003; Brüggen & Kaiser, 2002; Omma et al., 2004; Moll et al., 2007; Roediger et al., 2007; Pope et al., 2010).

Clusters such as M87 and Hydra A, due to their prolific cavity systems and availability of deep observations, were prime examples of radio jets interacting with the high metallicity ICM. In M87, it has been shown that along the bright, X-ray filaments that coincide with the radio jets, the metallicity content is higher than the average surrounding area out to 20 kpc from the BCG (Simionescu et al., 2008; Kirkpatrick, McNamara & Cavagnolo, 2011). Similarly, Hydra A showed this same effect, but out to distances of 100 kpc (Simionescu et al., 2009; Kirkpatrick et al., 2009a; Gitti et al., 2011). Hydra A is undergoing a much more powerful outburst than the current outburst in M87 and is the most likely explanation why material is uplifted further out. Expanding this analysis to a larger sample of 10 objects, it was confirmed that jet power does determine how much uplift in a cluster center can occur (Kirkpatrick, McNamara & Cavagnolo, 2011). This process appears to be a long lasting effect over many generations of cavities and could potentially be responsible for enriching the entire cluster core, not just along pointed outbursts.

In this chapter we present our analysis of a sample of 29 galaxy clusters drawn from the *Chandra X-ray Observatory* archive, chosen based on the requirement of AGN activity exhibited by X-ray cavities and long exposure times needed for accurate measurement of the metallicity content. The first goal is to further refine the relationship established by Kirkpatrick, McNamara & Cavagnolo (2011) between jet power and the extent metals are uplifted out of the cluster center. The second goal is to test whether or not over the lifetime of a cluster, an AGN can be the driving mechanism behind uplifting all the gas originally associated with the BCG and creating the broad abundance peaks we currently observe. Throughout this chapter, we assume a ΛCDM cosmology with $H_\circ = 70$ km s^{-1} Mpc^{-1}, $\Omega_M = 0.3$, and $\Omega_\Lambda = 0.7$. All uncertainties are quoted at the 67% confidence level.

5.2 Cluster Sample

All clusters in this sample were selected from the study done by Rafferty et al. (2006). The sample covers system sizes from elliptical galaxies up to the most massive of galaxy clusters, each currently exhibiting AGN activity in the form of radio emission filled X-ray cavities. In total, 29 clusters were chosen for this study. Previously we have studied a smaller subset of cool-core clusters, referred to as the "high quality" sample, to determine what relationship exists between the jet power of an AGN and the mixture of heavy metals in the ICM (Kirkpatrick, McNamara & Cavagnolo, 2011). When searching for data for the high quality sample, we selected the clusters with deep enough exposures to allow us to make metallicity measurements on spacial scales similar to that of the radio/cavity system of the cluster. Here we have added 7 more systems to the sample, which brings the total to 17, in an effort to further calibrate the "iron radius" relationship. Table 5.1 has a complete list of the clusters and observations used in this study. A second set of cool-core clusters, referred to as the extended sample, is used for the purpose of investigating the predictive powers of the iron radius relationship as well as for the analysis of general cluster properties. The list of these 12 clusters and observations used can be found in Table 5.2.

5.3 Data Preparation

All data analyzed in this study are publicly available in the *Chandra X-ray Observatory* data archive. Data preparation was carried out using version 4.1.2 of both CIAO and the calibration database. When present, background flares were eliminated from each observation using the *lc_clean* routine, a part of the contributed scripts. Using the full energy range (0.3-10 keV), a light curve is extracted from the level 2 event file. Time intervals with a count rate that varies more than 3-sigma from the mean are automatically eliminated and confirmed by eye. The corrected exposure time for each ObsID can be found in Tables 5.1 and 5.2. Time-dependent gain and charge transfer inefficiency corrections have also been applied. Background subtraction was carried out using blank-sky background files normalized to the source image count rate in the 9.5-12 keV energy band. Coordinates are reprojected to match the new background file to the source image in order for background spectra to be extracted from the equivalent regions. Observations with multiple pointings are stacked in order to properly identify the faintest of point sources using *wavedetect*. Each point source is marked, confirmed manually, then compiled into a list. The region list is used to remove all photons located within for each pointing individually.

Table 5.1: High quality sample.

System	ObsID	Exp. Time[a] (ks)	z	$P_{\rm jet}$[b] (10^{42} erg s^{-1})	$M_{\rm B}$[c]	$R_{\rm e}$[c] (kpc)
A133	2203	34.4	0.0566	620	-22.64	52.5
	9897	69.2				
A262	2215	28.7	0.016	9.7	-21.07	25.1
	7921	110.7				
Perseus	3209	95.8	0.018	150	-22.65	23.5
	4289	95.4				
	4946	23.7				
	4947	29.8				
	4948	118.6				
	4949	29.4				
	4950	85.4				
	4951	96.1				
	4952	164.2				
	4953	30.1				
	6139	56.4				
	6145	85.0				
	6146	47.1				
2A 0335	919	19.2	0.035	24	-23.04	30.9
	7939	49.5				
	9792	33.7				
A478	1669	42.4	0.088	100	-23.54	28.4
	6102	10.0				
MS 0735	10468	46.0	0.22	6900	-22.18	40.0
	10469	93.3				
	10470	141.9				
	10471	19.5				
	10822	75.4				
	10918	65.2				

Table 5.1 – Continued

System	ObsID	Exp. Time[a] (ks)	z	$P_{\rm jet}$[b] (10^{42} erg s^{-1})	$M_{\rm B}$[c]	$R_{\rm e}$[c] (kpc)
	10922	35.2				
Hydra A	4969	83.1	0.055	430	-23.05	42.3
	4970	98.8				
HCG 62	921	48.5	0.014	3.9	-19.97	13.3
	10462	67.1				
	10874	51.4				
A1795	3666	14.4	0.063	160	-22.59	45.8
	5286	14.3				
	5287	14.3				
	5288	14.6				
	5289	15.0				
	5290	15.0				
	6159	14.9				
	6160	14.8				
	6161	13.6				
	6162	13.6				
	6163	14.9				
	10898	15.7				
	10899	14.9				
	10900	15.8				
A1835	6880	117.9	0.253	1800	-23.27	31.8
	6881	36.3				
	7370	39.5				
A2029	891	19.8	0.077	87	-19.87	52.6
	4977	77.9				
A2052	5807	127.0	0.035	150	-21.74	38.0
	10477	61.2				
	10478	119.1				

Table 5.1 – Continued

System	ObsID	Exp. Time[a] (ks)	z	$P_{\rm jet}$[b] (10^{42} erg s^{-1})	$M_{\rm B}$[c]	$R_{\rm e}$[c] (kpc)
	10479	64.9				
	10480	19.9				
	10879	81.1				
	10914	38.8				
	10915	15.0				
	10916	35.0				
	10917	55.3				
A2199	497	18.7	0.030	270	-23.01	38.5
	498	17.9				
	10748	40.6				
	10803	30.2				
	10804	18.8				
	10805	30.3				
Cygnus A	360	34.7	0.056	1300	-21.83	17.9
	5830	23.4				
	5831	51.1				
	6225	24.3				
	6226	23.8				
	6228	16.0				
	6229	22.8				
	6252	29.7				
Sersic 159	1668	9.9	0.058	780	-22.34	36.9
	11758	97.7				
A2597	922	23.3	0.085	67	-22.51	39.8
	6934	52.2				
	7329	58.9				
M87	5826	126.8	0.0043	6	-22.05	18.9
	5827	156.2				

Table 5.1 – Continued

System	ObsID	Exp. Time[a] (ks)	z	$P_{\rm jet}$[b] (10^{42} erg s^{-1})	$M_{\rm B}$[c]	$R_{\rm e}$[c] (kpc)
	5828	33.0				
	6186	51.6				
	7210	30.7				
	7211	16.6				
	7212	65.2				

[a]Exposure time after blackground flares removed.
[b]Rafferty et al. (2006)
[c]*HyperLeda*

Table 5.2: Extended sample.

System	ObsID	Exp. Time[a] (ks)	z	$P_{\rm jet}$[a] (10^{42} erg s^{-1})	$M_{\rm B}$[a]	$R_{\rm e}$[a] (kpc)
A85	904	38.4	0.055	37	-22.76	47.4
PKS 0745	508	12.0	0.103	1700	-20.53	15.6
	2427	17.9				
	6103	10.3				
4C 55.16	1645	8.3	0.241	420	-22.14	46.5
	4940	87.5				
RBS 797	2202	11.7	0.35	1200	—	—
	7902	38.0				
A2390	500	9.8	0.23	*	—	—
	501	8.8				
	4193	92.0				
Zw 2701	3195	26.7	0.21	*	-22.25	48.8
	12903	95.8				
Zw 3146	909	45.7	0.29	*	-22.81	32.0
	9371	37.6				
MACSJ1423	1657	18.5	0.54	1400	—	—
	4195	115.1				
MKW 3S	900	57.3	0.045	410	-22.09	34.2
Hercules A	5796	47.3	0.15	310	-21.51	31.9
	6257	49.5				
3C 388	4756	7.7	0.091	200	-22.98	36.0
	5295	30.7				
A4059	5785	91.9	0.048	96	-22.88	53.8

[a]Same as Table 5.1.

5.4 Data Analysis

5.4.1 X-ray Spectra

All X-ray data in our sample were observed with the *Chandra* ACIS detector, using either the ACIS-S3 back-illuminated CCD, or the ACIS-I front-illuminated CCD array. Spectra are extracted using the CIAO tool *dmextract*. All observations are reduced/analyzed at a focal temperature of $-120°$C, or at $-110°$C on the back-illuminated ASIS-S3 for observations before 2000 January 29. This allows us to created weighted response files using the CIAO tools *mkacisrmf* and *mkwarf*.

Throughout this paper we have modeled all spectra using the same single temperature plasma model with absorption unless otherwise noted. Using WABS×MEKAL components in Xspec over the energy range 0.5-7 keV, temperature, abundance, and normalization are allowed to vary. The column density is set to the values quoted by Dickey & Lockman (1990). The internal ratio between metals are set by Grevesse & Sauval (1998), based on solar photospheric data.

In instances where the spectra are poorly fit by the single temperature approximation, we have turned to two different alternatives. We have shown previously for some clusters that the core is sometimes better fit with a multi-temperature model (Kirkpatrick et al., 2009b), which is apparent by a sharp decrease in metallicity where a peak is expected (Buote, 2000; Molendi & Gastaldello, 2001). This method of diagnosis is limited to use only in cores and gives us no way to identify multi-temperature regions in other parts of the ICM without any prior assumption of the distribution of metals. What this does tell us are the characteristics of a poorly fit spectrum in a region that may have multi-temperature gas. Single temperature models underestimate the emission at energies higher than 4 keV. This underestimation has not only been seen in the cores of clusters in our sample, but also in resolvable outflow regions due to AGN activity. An example of a typical spectrum is presented in the left panel of Figure 5.1. The residuals show all data points at greater than 4 keV systematically lie above the single temperature fit. Throughout this sample, all spectra fit for maps and profiles have been identified by poor chi-squared statistics and confirmed by visual inspection. These spectra are then fit by adding a second temperature component (WABS×(MEKAL+MEKAL)). The second component's temperature and normalization are allowed to vary with the abundance tied to the abundance of the first component. The two-temperature fit shown in the right panel of Figure 5.1 has fully corrected the underestimation. When blindly applying the two temperature model to all spectra, those extracted from regions already well fit by the single temperature model find the second

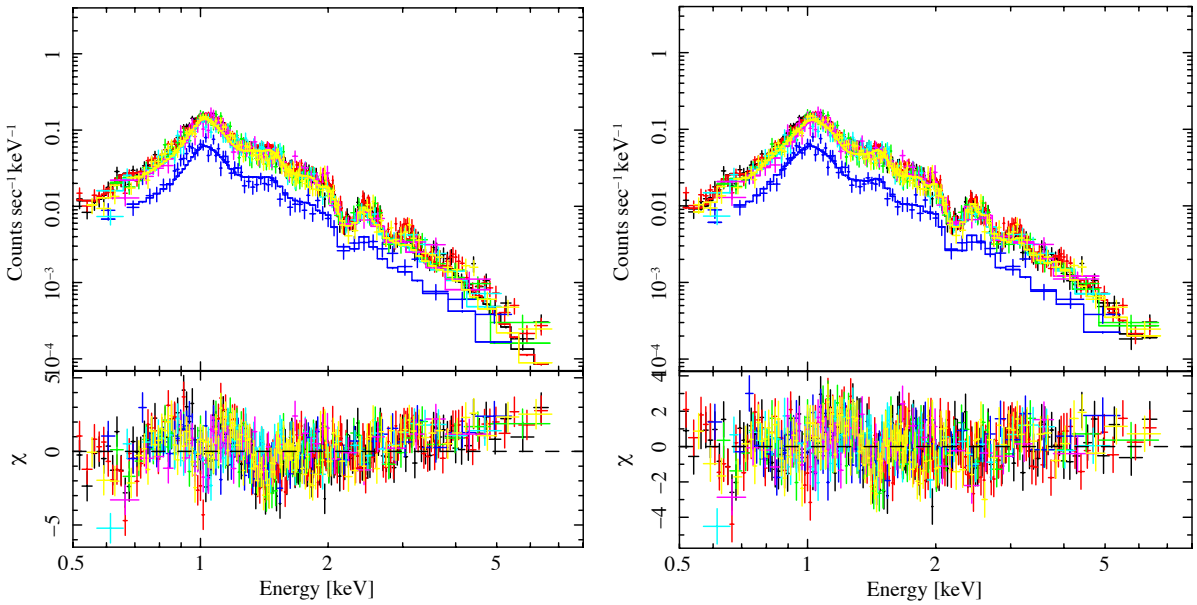

Figure 5.1: *Left*: A typical, multi-observation X-ray spectrum poorly fit by a single-temperature model. *Right*: The same spectrum is better fit at energies above 3 keV when a second temperature component is added.

component consistent with zero or an improvement in chi-squared statistics that are shown to be insignificant when performing an F-test.

The second alternative to our model involves varying column density during fitting. Our initial assumption is that the 21 cm column density is uniform over the width of the beam. Using the standard value can lead to a poor fit at low energies for systems at the same locations on the sky as large molecular clouds (Bregman et al., 2003; Bourdin & Mazzotta, 2008). The spectrum presented in the left panel of Figure 5.2 is an example of a poor fit due to the underestimation of the column density due to variations on cluster sized scales. The top row of Figure 5.3, 100 μm images from the IRAS all sky survey, is an example of sky regions where the approximated column density values are not valid . Compared to the bottom row of the same figure, where emission is smooth over the entire field, there is significant structure. We have found that poorly fit clusters at energies below than 1 keV in our sample all correspond to regions obscured by molecular clouds. The right panel of Figure 5.2 represents the improvement in spectral fitting when column density is allowed to vary.

5.4.2 Metallicity Maps

For each system in the high quality sample, we have produced high resolution maps of the spatial projected properties of the cluster. The binning of the data is carried out using a weighted Voronoi tessellation (WVT) algorithm (Diehl & Statler, 2006), a generalization of a previous algorithm (Cappellari & Copin, 2003). We start by defining a minimum signal-to-noise (S/N) of 100 for each bin. For deeper data, we have increased this value up to 150 or 200. For the Perseus cluster, the S/N was set to 1000 to lower the number of bins created. Using a S/N of our minimum standard would create almost 6000 bins where only 100 are needed for this analysis and saves many hours of computational time. The goal is the achieve bin sizes that minimize uncertainties as much as possible while over-sampling the size of the radio/cavity system.

The WVT algorithm proceeds by searching for the highest S/N pixel in the input image, which normally corresponds to the approximate cluster center. The bin is grown by accreting the nearest neighbor with the highest S/N and then recalculates the centroid for the bin. This process is repeated until the bin reaches the target total S/N. The following bin is created similarly by finding the next highest S/N pixel closest to the centroid of all previously binned pixels. Because each bin is grown one pixel at a time, the desired S/N is very accurately achieved. The main reason we choose this method is due to the compact nature of the generated bins. For our analysis we are interested not only in how

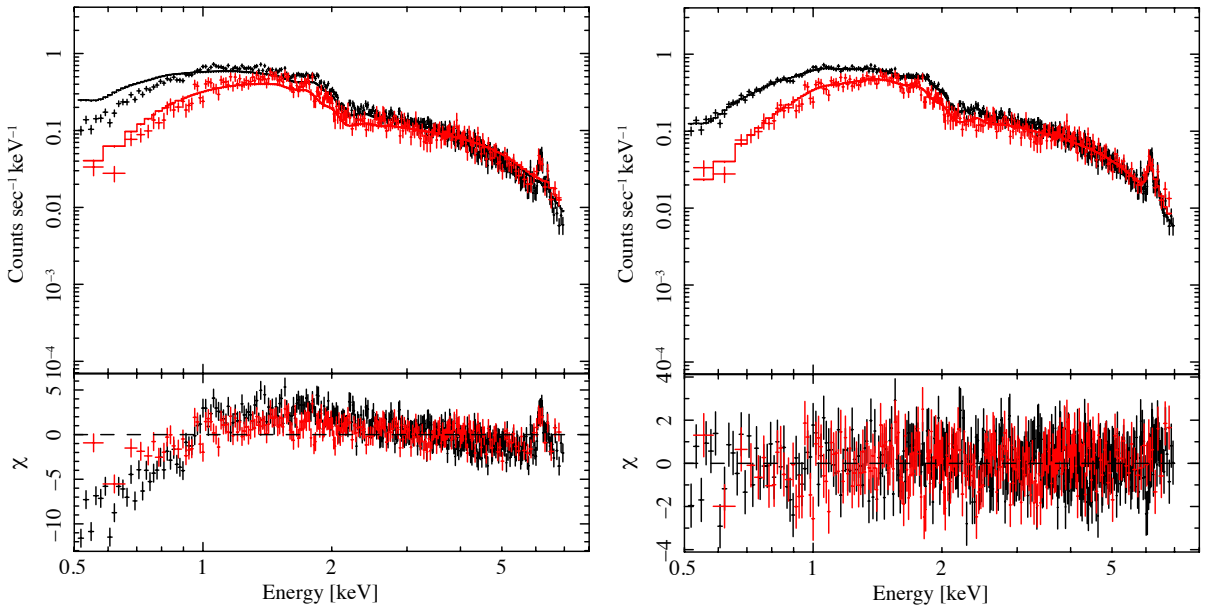

Figure 5.2: *Left*: A typical X-ray spectrum poorly fit when the average column density is underestimated. *Right*: Allowing the column density to vary when large molecular clouds are present along the line of sight improves the fit at energies below 1 keV.

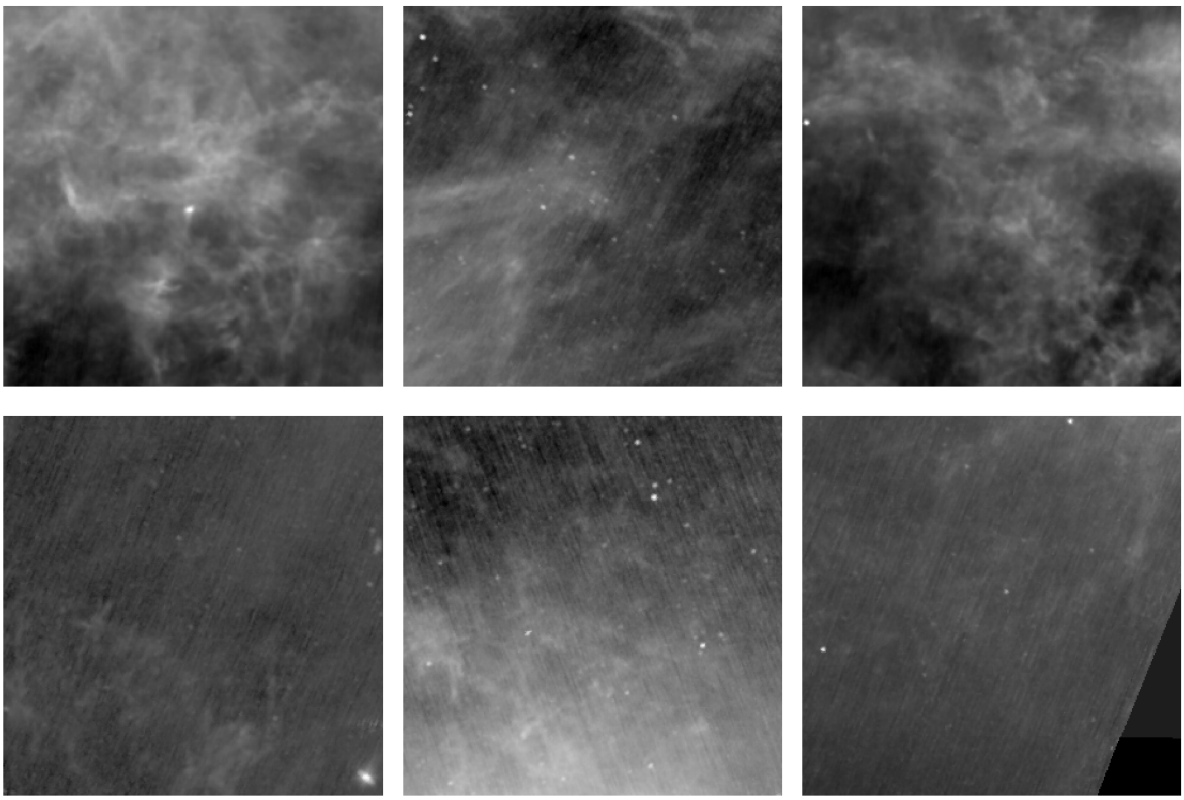

Figure 5.3: All panels are 7.5×7.5 degree IRAS 100 μm images. The top row images have lots of structure making average column densities inaccurate. Located at the centers of these three panels are A478, A262, and 2A 0335, respectively. The bottom row images are mostly smooth and have accurate average column densities. Located at the centers of these three panels are A133, A1835, and A2597, respectively.

the metallicity of the ICM changes with radius, but also with how it changes at fixed radii at different projected angles from the cluster center. Surface brightness contour binning creates wide, arc shaped bins which are not ideal for comparing regions at the same radius.

The metallicity maps of the entire high quality sample are presented in Figure 5.4. In each panel we have indicated with a black diamond the approximate cluster center, chosen based on location of central point source or the peak brightness of the BCG in the R-band. The jet angle is illustrated by the black circles approximating the size and position of the jet and cavity system. Jet angle and high metallicity regions in all systems are found to match one another (Kirkpatrick, McNamara & Cavagnolo, 2011). The full analysis of the significance of these regions is found in section 5.4.3.

For the extended sample, the metallicity maps found in Figure 5.5 were generated based on spatial resolution rather than S/N. This data sample does not go as deep as the high quality sample which would make the bins too large to achieve the minimum S/N we prefer, rendering the maps themselves useless. Instead we choose bin sizes for these maps in order to have more than 1 bin per quadrant on the sky and S/N ranging between 45 to 75. The black circles represent the approximate cavity size and position. We find systematically over the entire extended sample that there is a correlation between cavities and high metallicity, but for an individual system, the uncertainties are too large and there is too much variation across the individual fields to confidently say any single rise in metallicity correlates with outflowing gas from the AGN.

5.4.3 Updated P_{jet} - R_{Fe} Scaling Relation

Previously we have shown that there is a relationship between the power output by the central AGN of a galaxy cluster and the distance out to which we can measure an enhancement in metallicity of the ICM (Kirkpatrick, McNamara & Cavagnolo, 2011). We have shown this relationship by measuring metallicity profiles in two sectors on the sky for each cluster in our sample. The sectors consist of semi-annular-shaped bins where spectra are extracted, as demonstrated previously in Figure 3.1. One sector encompasses the entire region of a cluster where extended radio emission and/or a cavity system is detected ("on-jet"). The second sector is the region where the ICM is mostly undisturbed by the central AGN ("off-jet"). The assumption is this region of the ICM is what the current state of the metallicity profile for a cluster would look like if there had not been any recent AGN activity.

To find deviations between the on-jet profile and the off-jet profile, each semi-annular bin must have enough counts to reduce the uncertainties to approximately 10%. It is

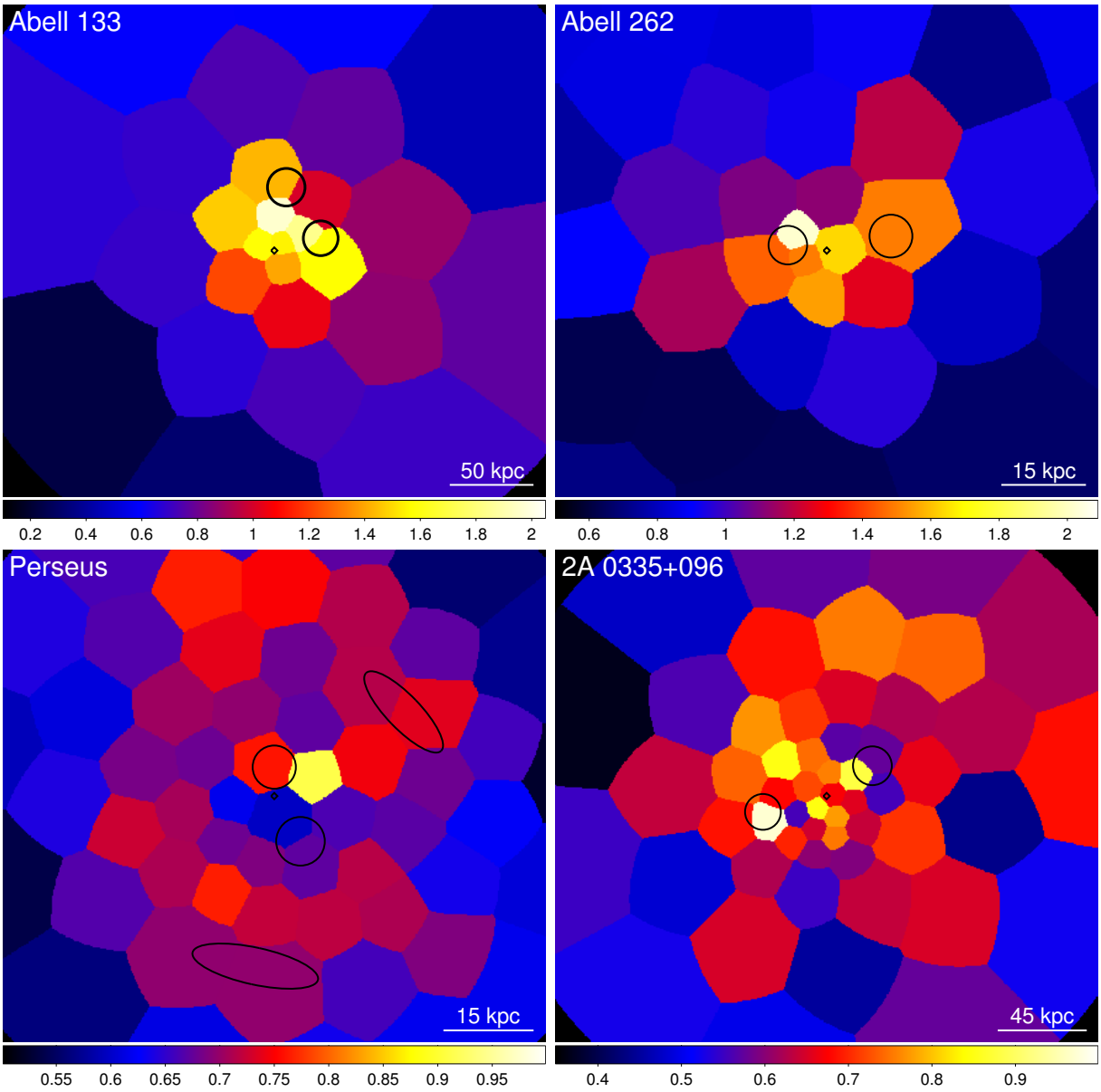

Figure 5.4: Metallicity maps for the high quality sample. The black diamonds represent the cluster center. The black circles are the approximate location of the radio jet and cavity system.

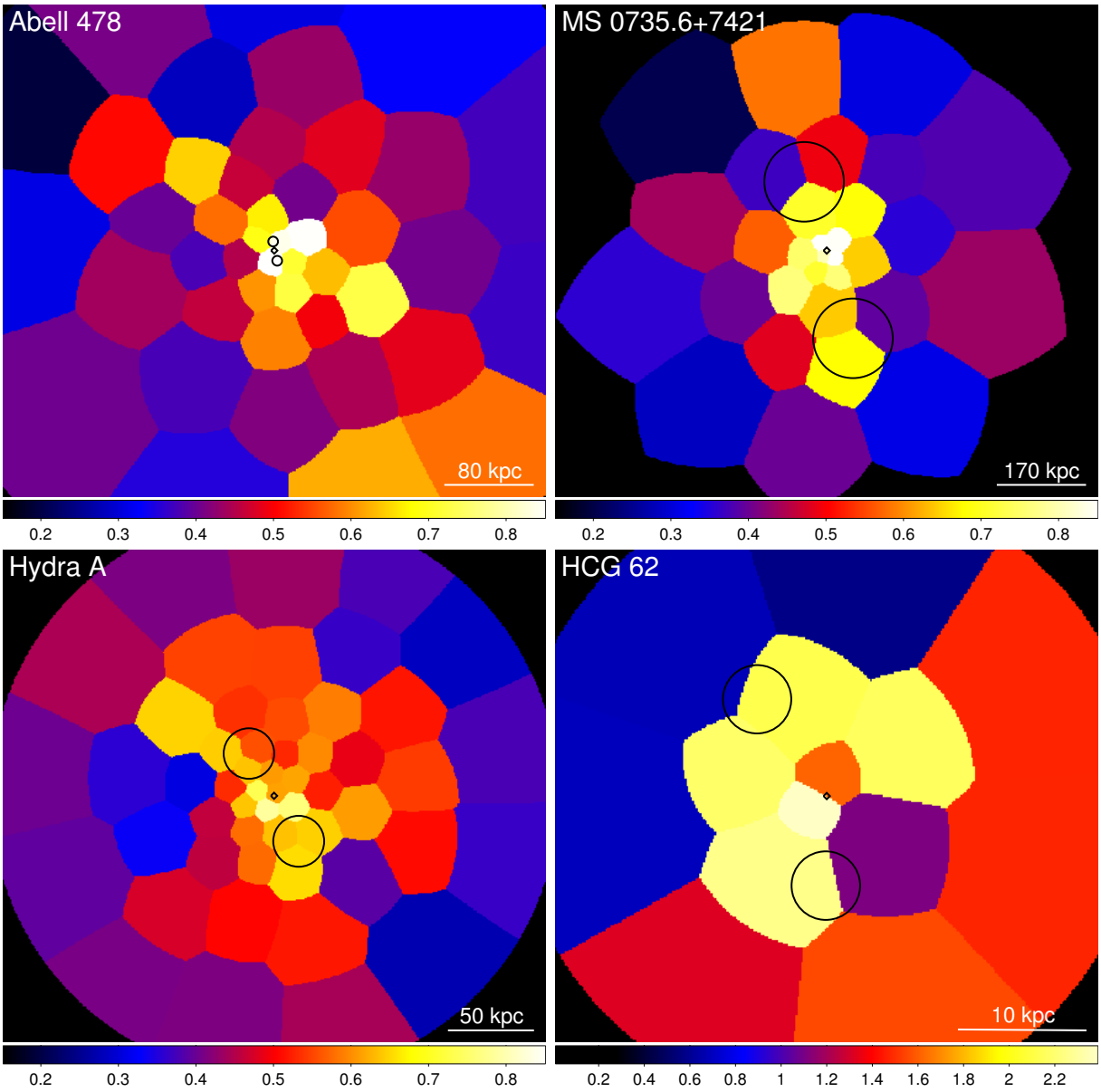

Figure 5.4: - *continued*

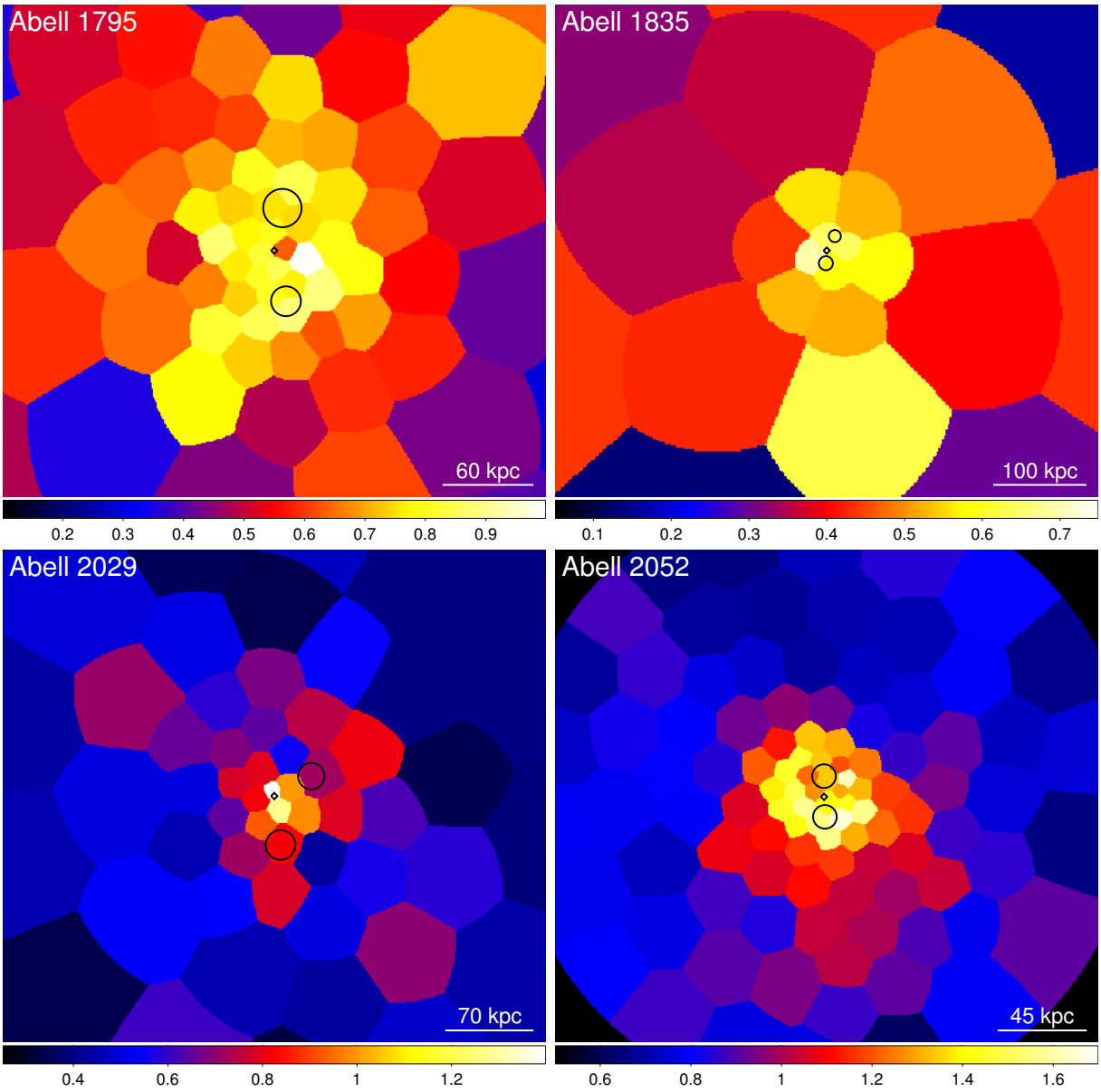

Figure 5.4: - *continued*

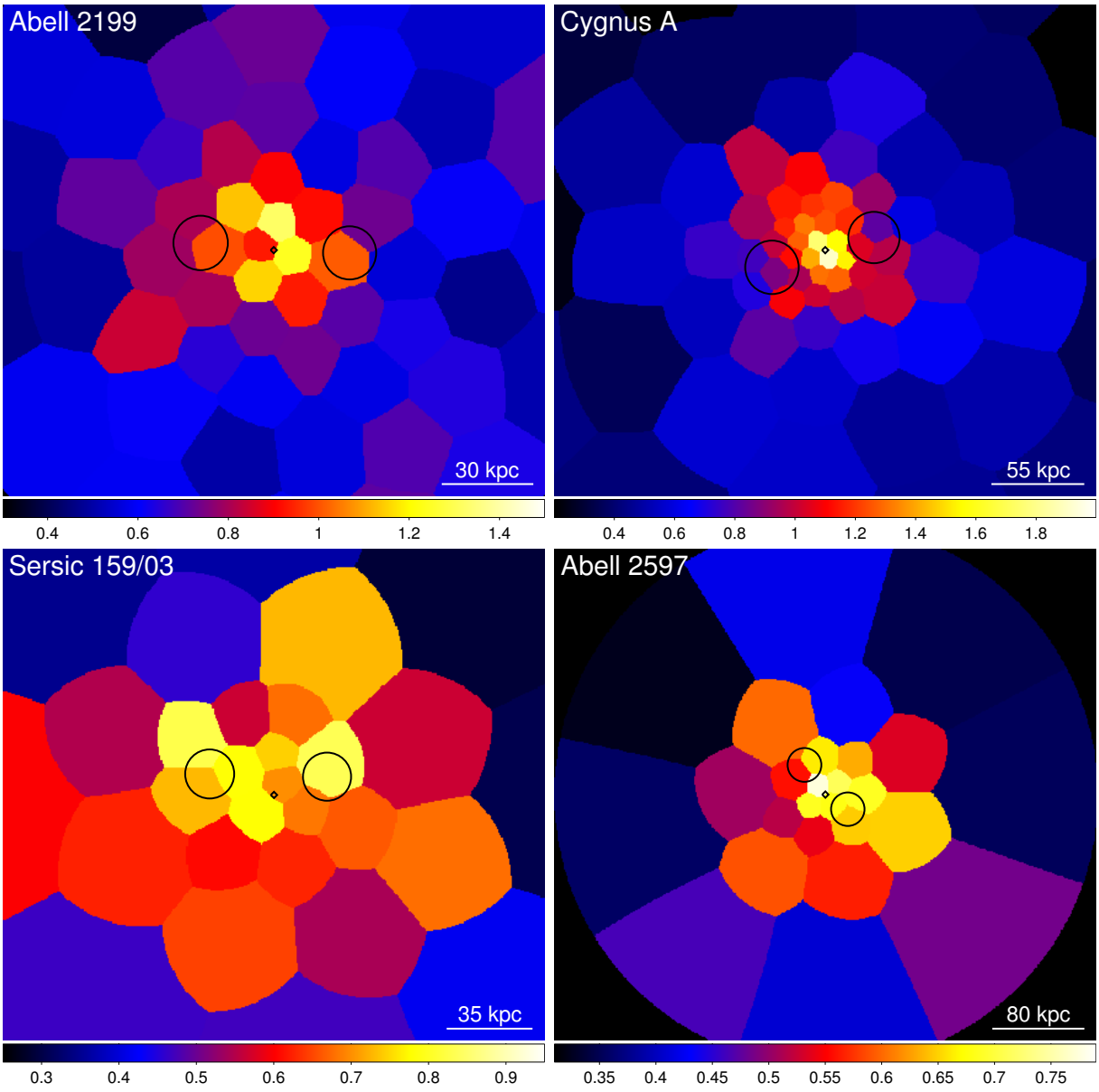

Figure 5.4: - *continued*

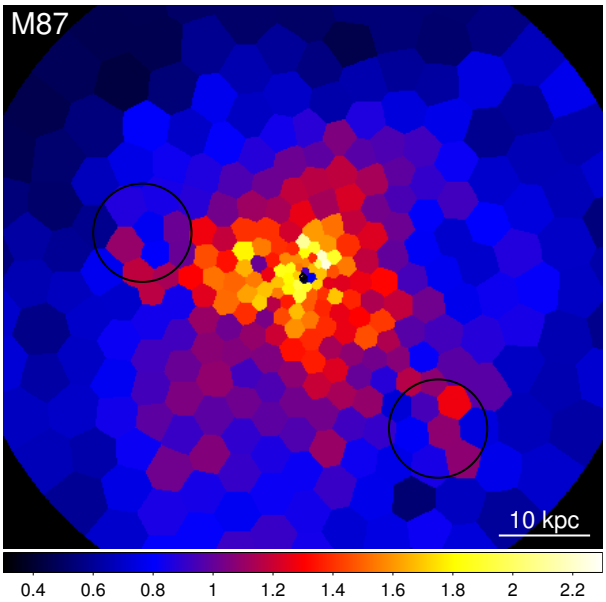

Figure 5.4: - *continued*

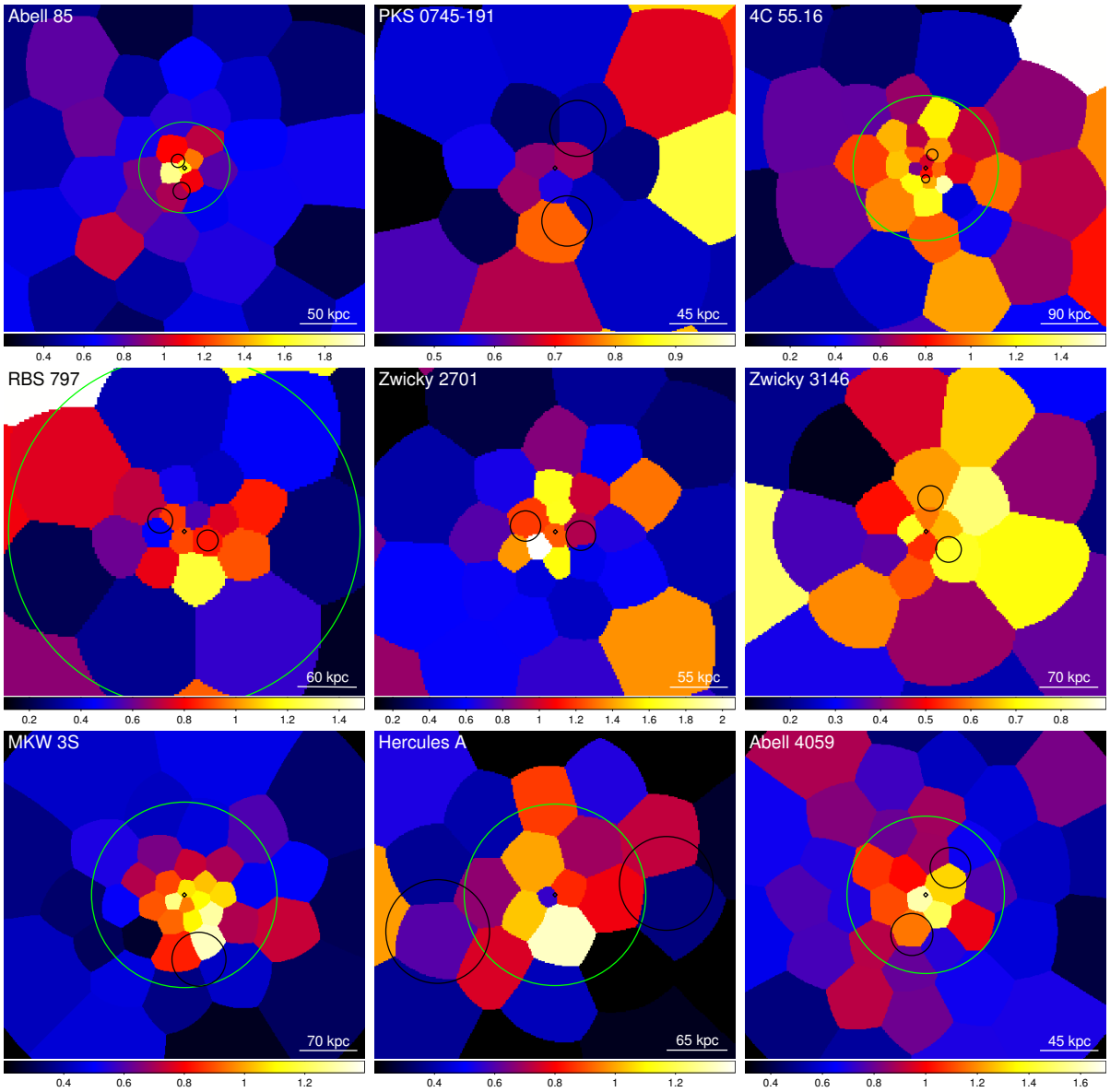

Figure 5.5: Metallicity maps for the extended sample. The black diamonds represent the cluster center. The black circles are the approximate location of the radio jet and cavity system. The green circles are the predicted iron radius, discussed in section 5.4.4.

also important to preserve spatial resolution. Large radial bins will wash out small scale fluctuations due to the metallicity gradient. To achieve this we have extracted profiles averaging 9 bins with a minimum S/N of 140 for each cluster in the high quality sample. The highest quality data (M87) allows for a total of 20 bins in the profile, allowing small variations to be noticeable. In the lowest quality case (MS 0735), there are only 4 bins to the profile, but due to the large variations due to the power AGN outburst, that is enough resolution for the purpose of our analysis. This does result in larger uncertainties in the extent at which the metals are distributed throughout the ICM.

All profiles for the complete high quality sample are found in Figure 5.6. The on-jet profiles are represented by the circular data points. The off-jet profiles are represented by the triangle data points. The dotted vertical line represents the location of the iron radius as discussed in Kirkpatrick, McNamara & Cavagnolo (2011). We define this point by counting bins outward from the center until we reach the last bin in a row where the 1σ error bars do not overlap and the regions outer to this are either indistinguishable between sectors or the off-jet region is higher in metallicity.

In Figure 4.3, with a smaller subset of data, we fit the relationship between AGN jet power and iron radius, found in equation 4.1. To further calibrate this trend, we have refit the data using the entire high quality sample which includes more low-power and high-power systems. The new jet power vs. iron radius plot is found in Figure 5.7. The jet powers used here were taken from cavity measurements by Rafferty et al. (2006), except for Sersic 150/03, which will be discussed in section 5.4.4. The best fit after performing a least-squares regression gives,

$$R_{\rm Fe} = (61 \pm 6) \times P_{\rm jet}^{(0.43\pm0.01)} \text{ (kpc)}, \tag{5.1}$$

where jet power is in units of 10^{44} erg s^{-1}. The new rms scatter is approximately 0.42 dex. Increasing the sample size from 10 to 17 does not make a notable change to the fit. The predicted iron radius is slightly higher, but within the error of the sample, the new relationship is indistinguishable from that in Kirkpatrick, McNamara & Cavagnolo (2011). We note that the scatter has decreased by adding additional objects, further strengthening the correlation.

5.4.4 Iron Radius as a Predictor of Jet Power

With a calibrated $P_{\rm jet} - R_{\rm Fe}$ scaling relation, it is possible to predict the average jet power of past AGN activity for a cluster independently from cavity measurements. Cavities at large distances from the center can be difficult to detect due to decreasing surface brightness.

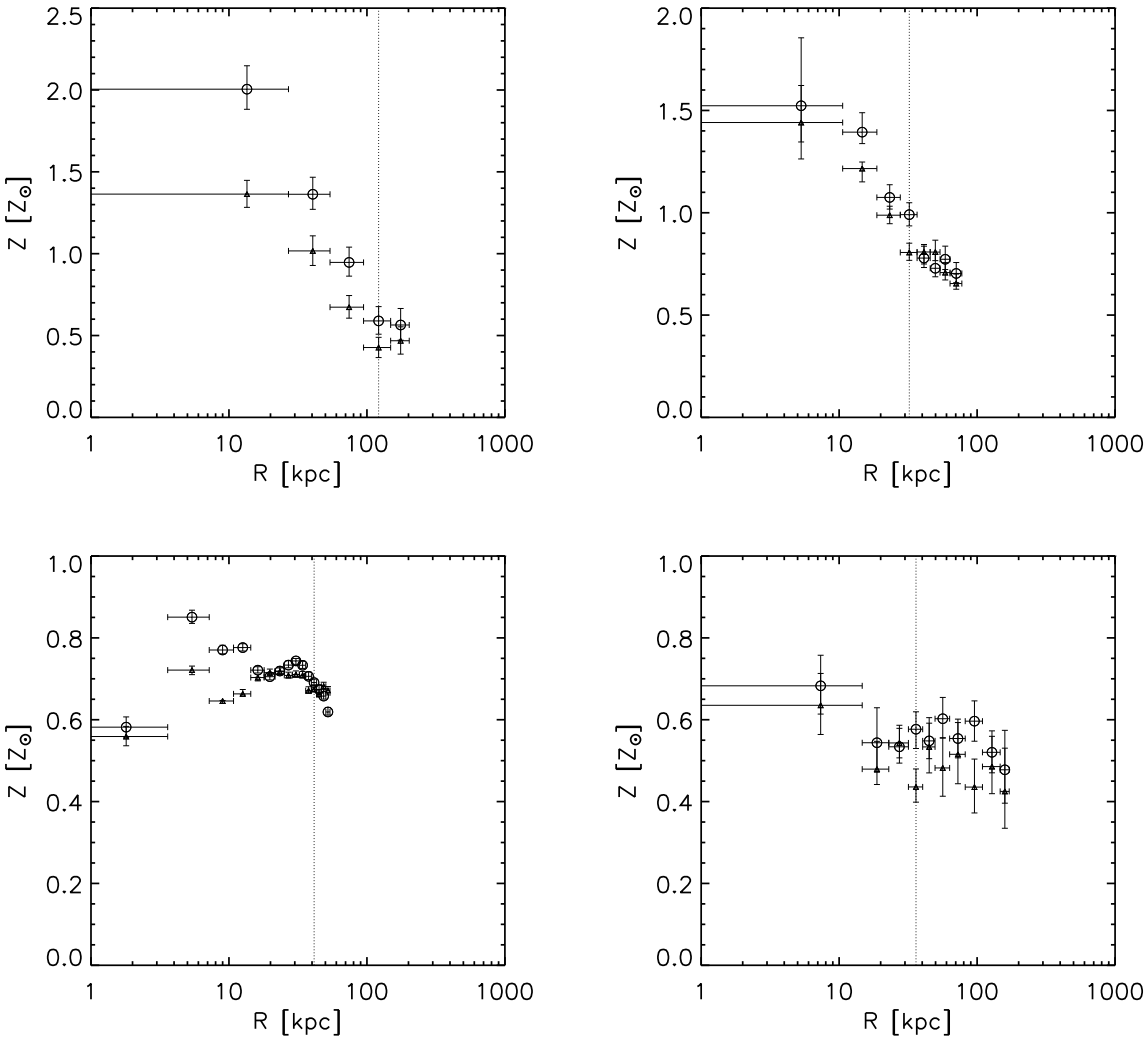

Figure 5.6: Metallicity profiles for on-jet regions are represented by circles. Off-jet profiles are represented by triangles. The dotted line is the measured iron radius. Top row: A133 and A262. Bottom row: Persues and 2A 0335.

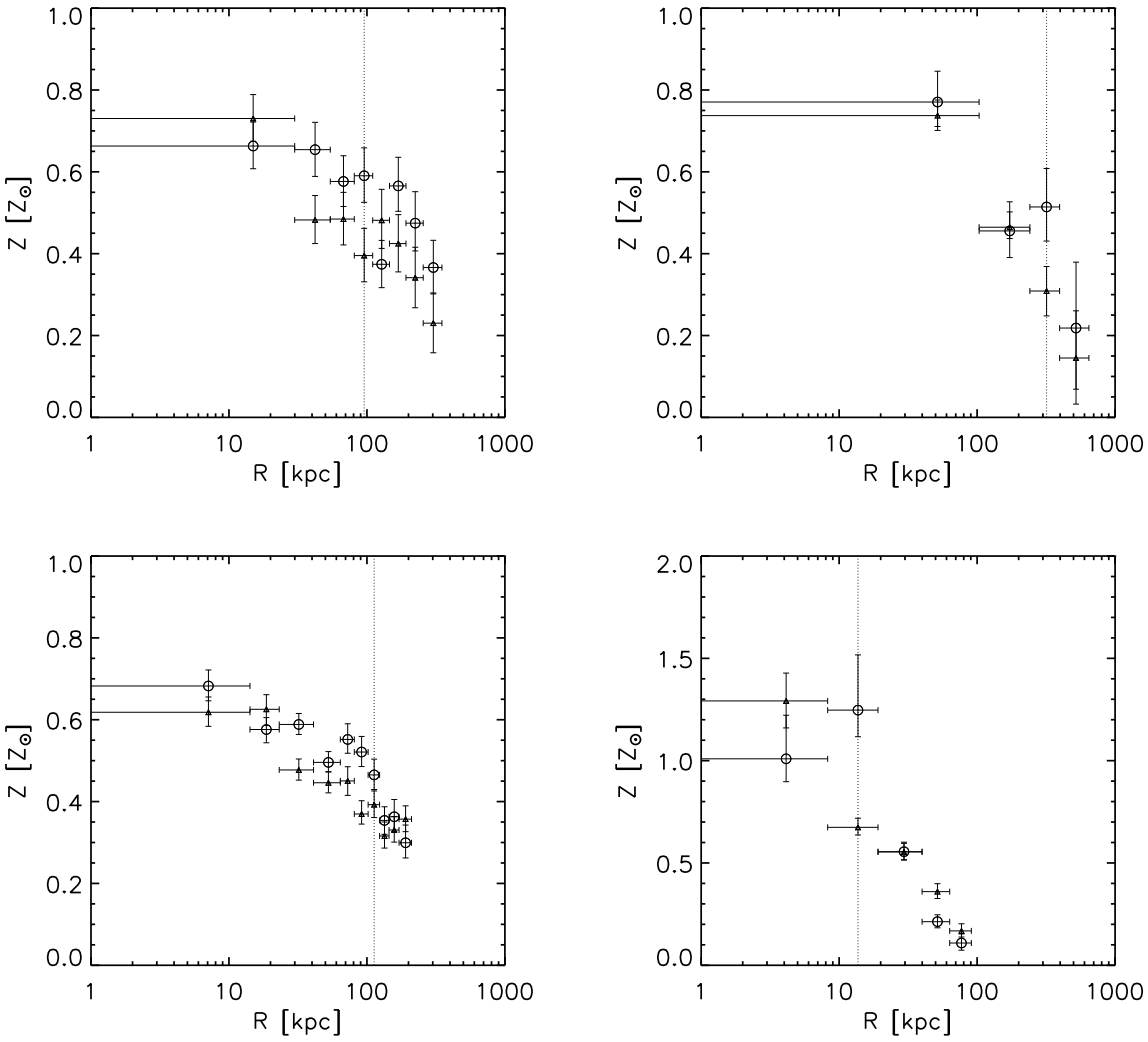

Figure 5.6: - *continued*: Top row: A478 and MS 0735. Bottom row: Hydra A and HCG 62.

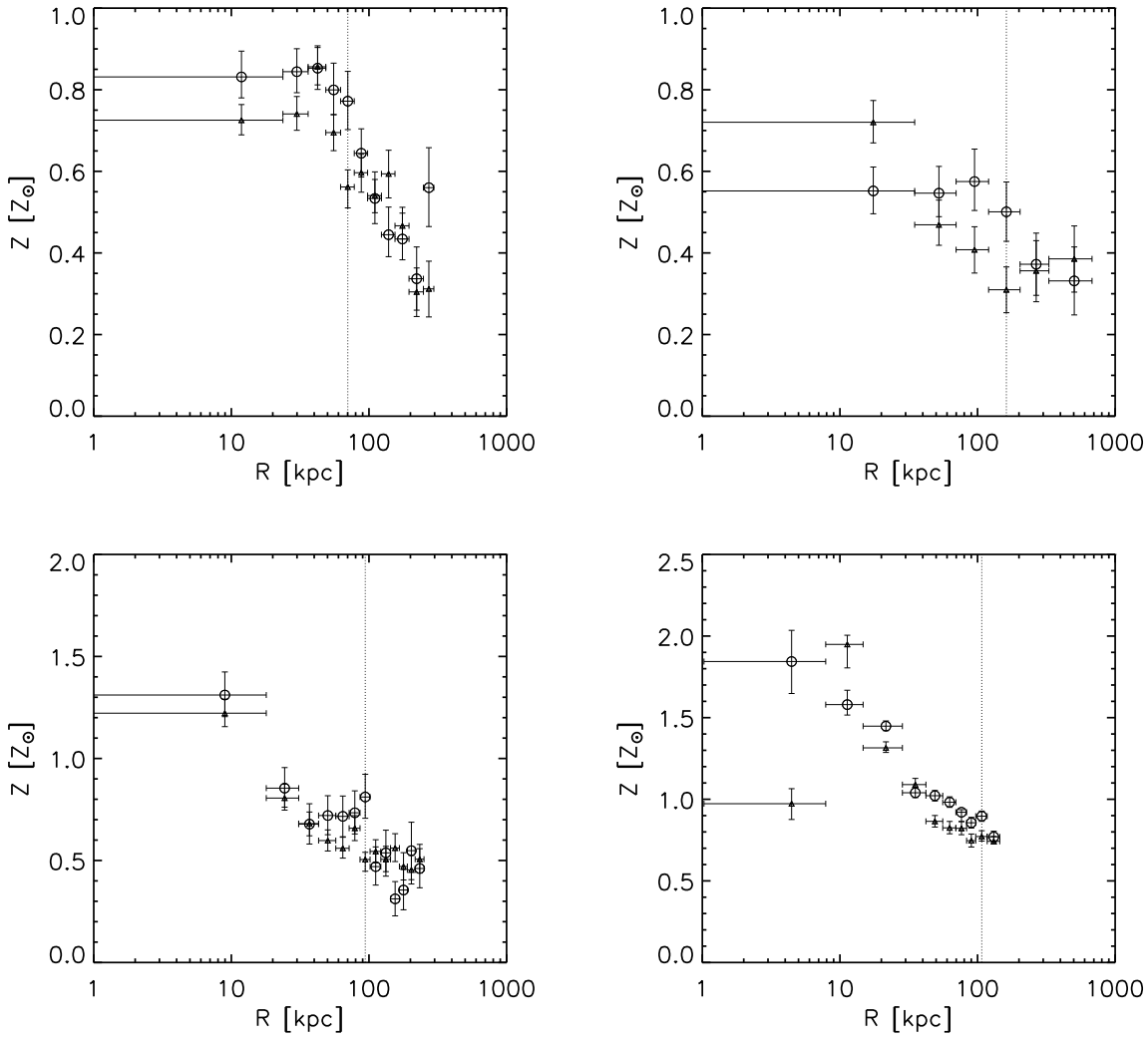

Figure 5.6: - *continued*: Top row: A1795 and A1835. Bottom row: A2029 and A2052.

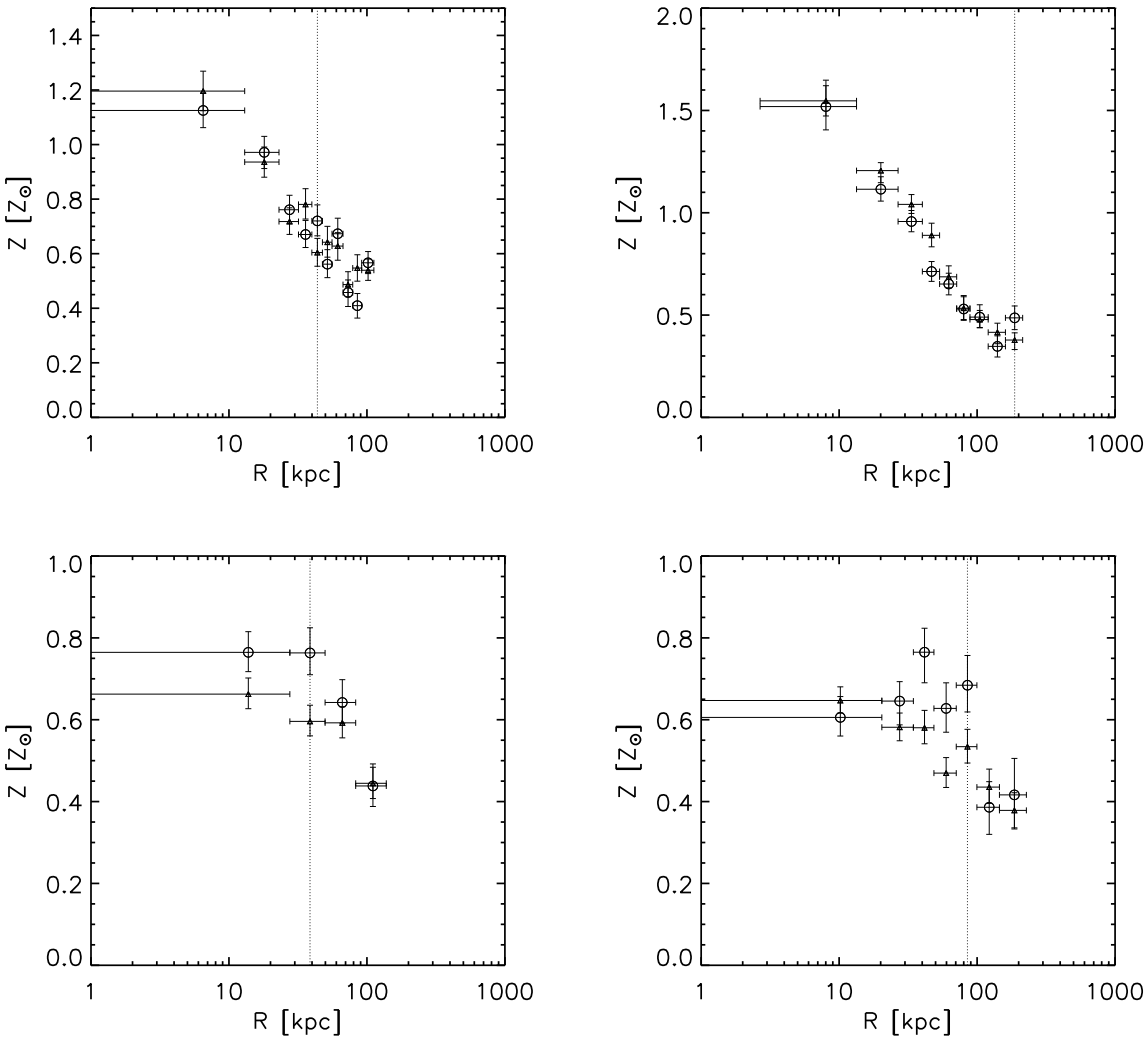

Figure 5.6: - *continued*: Top row: A2199 and Cygnus A. Bottom row: Sersic 159/03 and A2597.

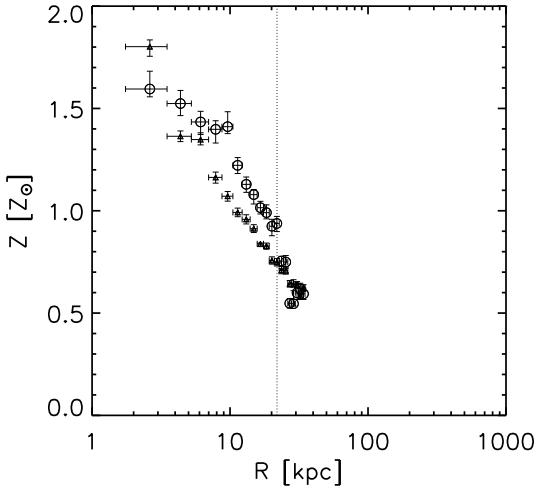

Figure 5.6: - *continued*: M87

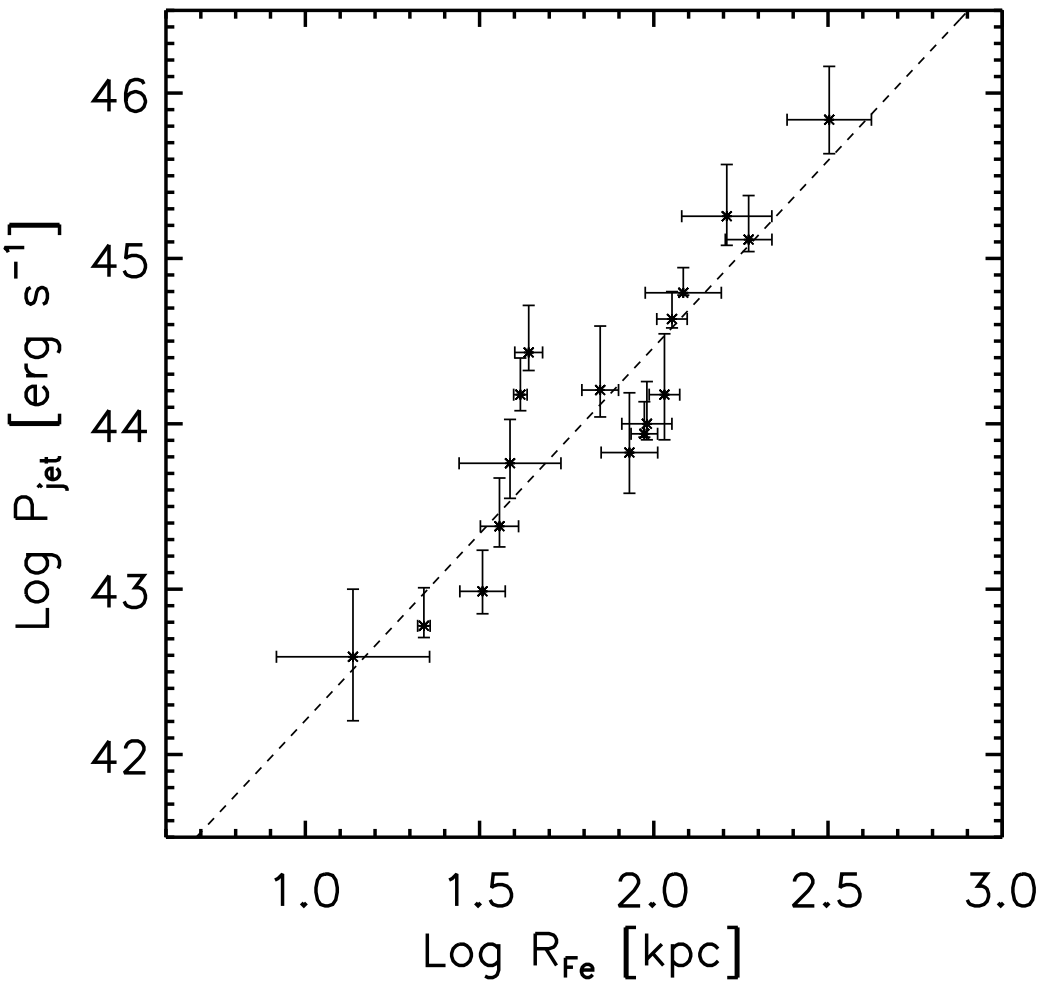

Figure 5.7: Updated jet power vs. iron radius including 7 more data points. The dashed line is the new best fit to the data.

There are a number of clusters in the Rafferty et al. (2006) sample with cavity powers comparable to MS 0735, but measured at very low significance. It would be rather difficult to successfully propose follow up observations for targets that could potentially have little AGN activity.

Sersic 159/03 is a good target for testing the predictive power of our relationship. Sersic 159/03 has been observed recently for a second time with the *Chandra X-ray Observatory*. The cluster was observed for 99 ks on 2009 August 24 (ObsID 11758) using the ACIS-I CCD. After cleaning and combining with the original observation, the net exposure time comes out to 107.7 ks. With only the original 9 ks observation, the cavity power was estimated to be $780^{+820}_{-260} \times 10^{42}$ erg s^{-1} (Rafferty et al., 2006). Plugging that into equation 5.1, the expected iron radius would be approximately 150^{+54}_{-24} kpc. Using our metallicity profile technique for determining the iron radius, we find a much smaller radius of 39 ± 11 kpc. Equation 5.1 predicts a cluster with this iron radius to have a jet power of about 3.5×10^{43} erg s^{-1}. This is more than an order of magnitude difference in jet power between the two measurements.

We can take better care at estimating the cavity sizes with the new data set. The positions of the cavities in Sersic 159/03 have been approximated by eye and masked out of the image. A surface brightness profile was constructed using elliptical annuli with the mask image. The profile is represented by the cross points found in Figure 5.8. A second surface brightness profile was constructed, this time using only the masked out regions, to compare to the "smooth" profile. Represented by diamond points in Figure 5.8, we see a 23% drop off in surface brightness at approximately 10 arc seconds. To quantify the projected two-dimensional shape of the cavities we have produced an unsharp mask image. We start by smoothing the image, using *aconvolve*, with a Gaussian that has a sigma of 10 pixels along each axis. This smoothed image acts as a cluster model that is then subtracted from the un-smoothed image. The resulting unsharp mask is presented in the left panel of Figure 5.9. The green ellipsoids highlight our best estimate of the locations and sizes of the cavities. This is similar to the result found by Dong et al. (2010). The eastern most cavity has a major and minor axis of 23.4 kpc and 16.8 kpc, respectively. The western cavity has a major and minor axis of 27.6 kpc and 18.8 kpc, respectively. To convert the projected cavity sizes into volumes, we must assume a radius in the third dimension. We approximate this by taking the ratio of the major axis to the minor axis and taking the upper bound of the third dimension to have that same ratio with the major axis. The same ratios is also used with the lower bound and the minor axis. Taking the average of the major and minor axis as the best guess for the third dimension radius a triaxial ellipsoid, the volumes of the cavities are $1.23^{+0.75}_{-0.50} \times 10^{68}$ cm^3 and $1.85^{+1.39}_{-0.83} \times 10^{68}$ cm^3 for the east and west cavities respectively. In order to calculate the total energy of the outburst, the deprojected

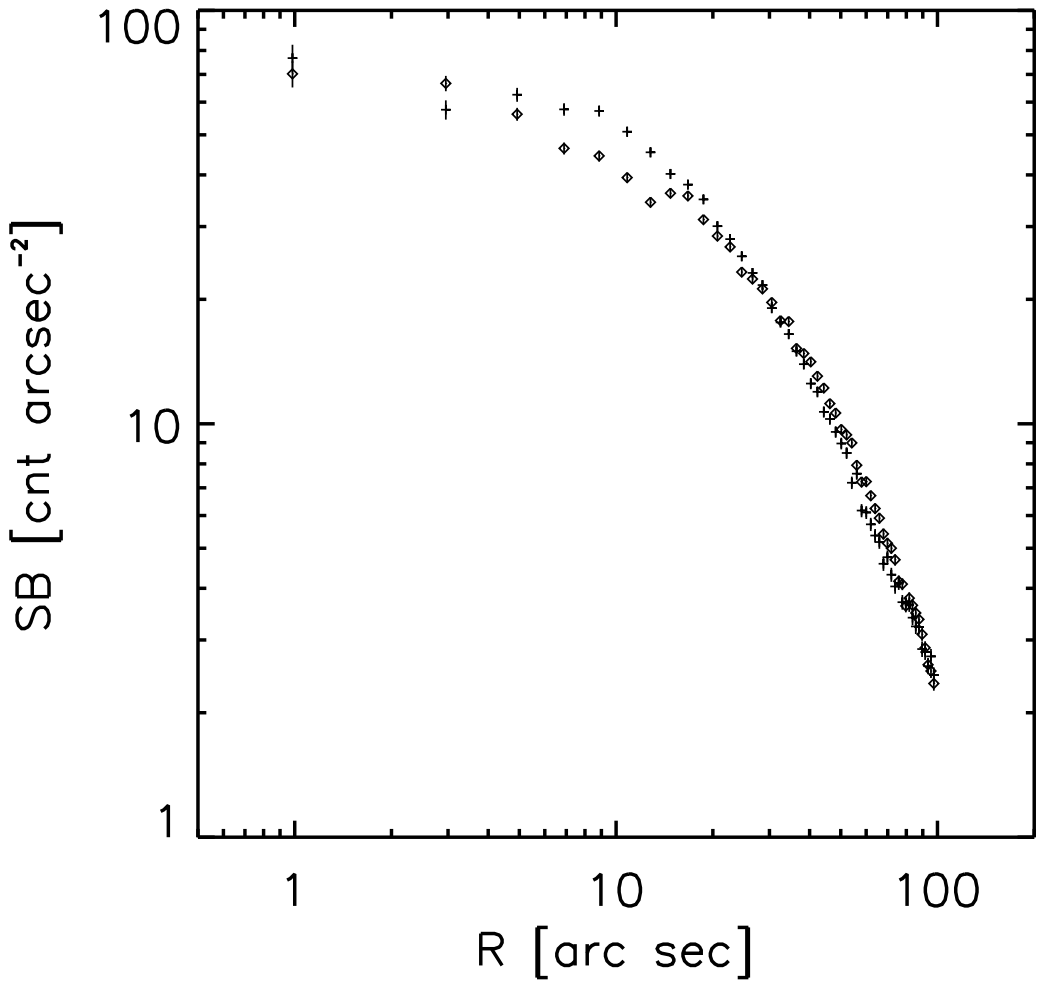

Figure 5.8: Diamond points are the surface brightness profiles along the cavity system. Cross points are the surface brightness profile with the cavity system removed.

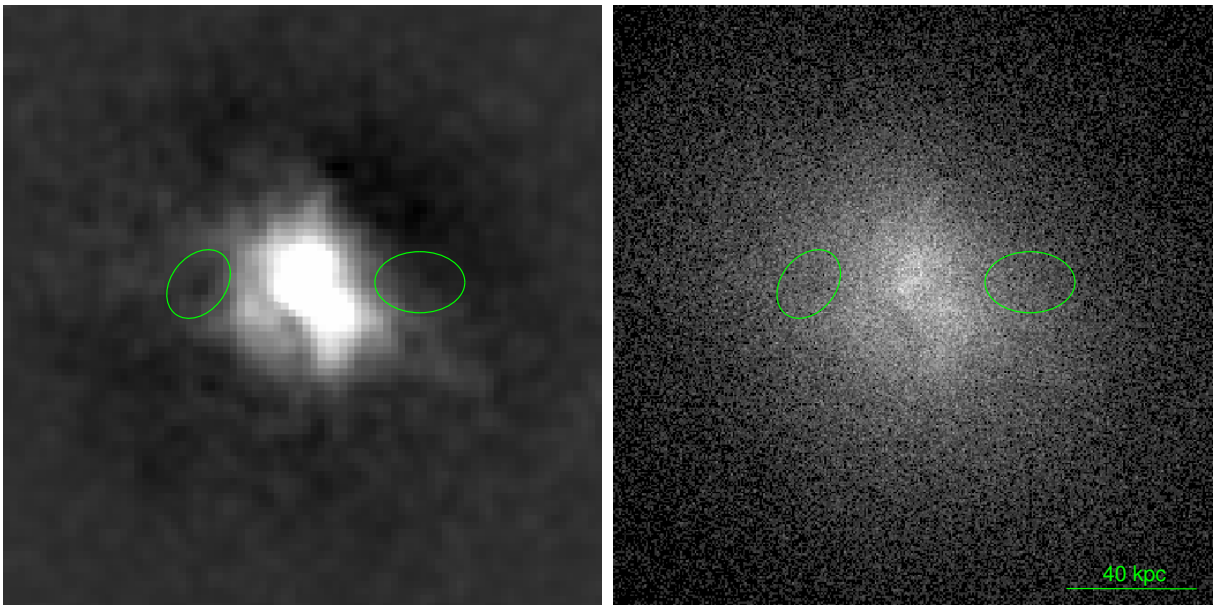

Figure 5.9: *Left*: Unsharp mask image of Sersic 159/03. The green circles are the sizes and positions of the cavities. *Right*: X-ray image of the same region with cavities superimposed.

density and temperature profiles found in the first and second panels of Figure 5.10 must be used to calculate pressure of the ICM. To carry out a deprojected fit, a large number of counts are need per bin. These bins have an average S/N value of 190. In the last panel of Figure 5.10 is the pressure profile for Sersic 159/03. We take the pressure at the center of the cavity as the average pressure the expanding cavities work against. The total work the AGN applies to the surrounding ICM is approximated as the pressure multiplied by the volume, giving pV $= 3.75^{+1.85}_{-1.15} \times 10^{58}$ erg. The total energy that goes into creating the cavity system is equal to the enthalpy. The enthalpy is given as,

$$E_{\rm cav} = pV\frac{\gamma}{\gamma - 1} = 4pV, \tag{5.2}$$

where $\gamma = 4/3$ is the ratio of specific heats for a relativistic gas filling the cavities. To convert this to a jet power, we assume the buoyancy time of the cavity to be the lifetime of the outbursts. The buoyancy time is given by

$$t_{\rm buoy} = R\sqrt{SC/2gV}, \tag{5.3}$$

where R is the projected distance to the center of the cavity to the center of the cluster, S is the cross section of the cavity, C = 0.75 is the drag coefficient (Churazov et al., 2001), g is the gravitational acceleration which is approximated as $\approx 2\sigma^2/R$, and V is the cavity volume. For any values not stated here, we have used the standard values as quoted in Bîrzan et al. (2004). The final jet power for the entire cavity system is $P_{\rm jet} = 5.77^{+4.86}_{-2.23} \times 10^{43}$ erg s^{-1}. This is consistent with the predicted value and is the value we have used in calibrating the $P_{\rm jet} - R_{\rm Fe}$ scaling relation in Figure 5.7.

It may be possible now to predict jet power in clusters where cavity size measurements are highly uncertain using the $P_{\rm jet} - R_{\rm Fe}$ scaling relation. The extended sample of clusters' data quality does not allow us to make on-jet and off-jet metallicity profiles that are distinguishable from one another. Still, a systematic trend can be seen in jet metallicity as shown in Figure 5.5. The green circles seen in some of the panels mark the predicted iron radius. In the panels where this circle is not seen (PKS 0745, Zw 2701, and Zw 3146), it is due to the fact the prediction is so large they are outside the field of view. For the rest there appears to be mixed results between the prediction and the maps. RBS 797, MKW 3S, Hercules A, and Abell 4059 all systematically show metallicity plumes extending out along the jet axis as highlighted by the black circles. Though they do not show the same significance as the high quality sample, they still exhibit the same properties. Abell 85 and 4C 55.16 stand out from the rest, though there does seem to be some indication the metallicity is higher along the jet, there is a hint that high metallicity material is out farther than the prediction. We can only speculate what this means. It is possible these cluster

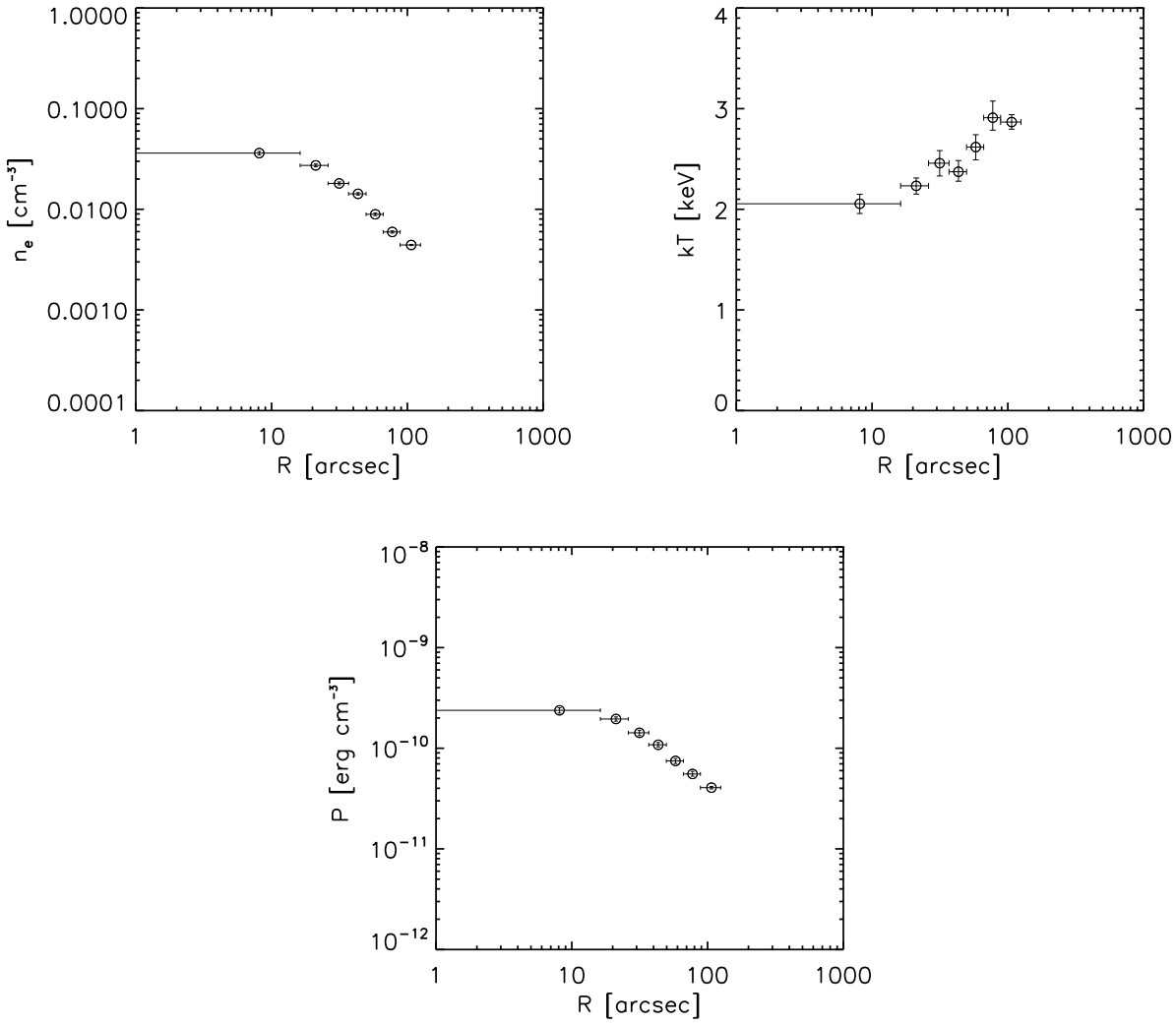

Figure 5.10: Deprojected density, temperature, and pressure profiles for Sersic 1159/03, respectively.

have larger, unseen cavity systems due the short exposure times, though it is equally probable better photon statistics would constrain metallicity values due to background subtraction uncertainties inherent in low surface brightness regions of the ICM.

Of the three clusters mentioned before with iron predictions too large to show in the metallicity maps, Zw 2701 shows indications that its actual iron radius may be much smaller. High metallicity material appears to stand out along the east to west axis to a radius of approximately 100 kpc. In Rafferty et al. (2006), they measured the jet power to be $6^{+8.9}_{-3.5} \times 10^{45}$ erg s^{-1}, which would correspond with an iron radius of 355^{+170}_{-112} kpc. As the second most power outburst in the sample, Zw 2701 was flagged as being a very low confidence measurement due to short exposure time. Since then, Zw 2701 has been re-observed for 97 ks on 2001 February 3 (ObsID 12903) using the ACIS-S CCD on board the *Chandra X-Ray Observatory*. The metallicity map presented in Figure 5.5 was constructed using the total exposure of 122 ks after cleaning. Following the same procedure as described above for Sersic 159/03, we have re-measured the cavity sizes and positions. Surface brightness plots for Zw 2701 are found in Figure 5.11. The cross points make up the profile with the cavity regions masked out. The diamond points make up the profile across the cavities. At approximately 7 arc seconds, there is a 34% deficit in surface bright across the cavities. An unsharp mask presented in the left panel of Figure 5.12 confirms the location and size of the cavity system. The previous measurement found the cavities to be two times larger than shown here. Here we measure the major axis of the east and west cavities to be 33.2 kpc and 52.4 kpc, respectively, as seen overlaid on the X-ray image in the right panel of Figure 5.12. Density, temperature, and pressure profiles generated for this analysis are found in Figure 5.13. We have calculated the total work for both the eastern and western cavities to be pV $= 2.61^{+0.62}_{-0.50} \times 10^{59}$ erg. Dividing the enthalpy (equation 5.2) by the buoyancy time (equation 5.3) gives a new jet power for Zw 2701 of $P_{\rm jet} = 4.21^{+1.50}_{-1.09} \times 10^{44}$ erg s^{-1}, more than a order of magnitude less than the original measurement. The new power corresponds to an iron radius of 113 kpc on the scaling relation. This new iron radius is indicated on the metallicity map presented in Figure 5.14. This falls in line more with what the metallicity map is suggesting for the distribution of metals.

5.4.5 Outflow Energy in Radio Jets

With large quantities of material being uplifted out of the centers of galaxy clusters, some fraction of the total energy must go into moving gas. This was originally calculated for Hydra A where it was found the energy was comparable to work done to inflate the inner

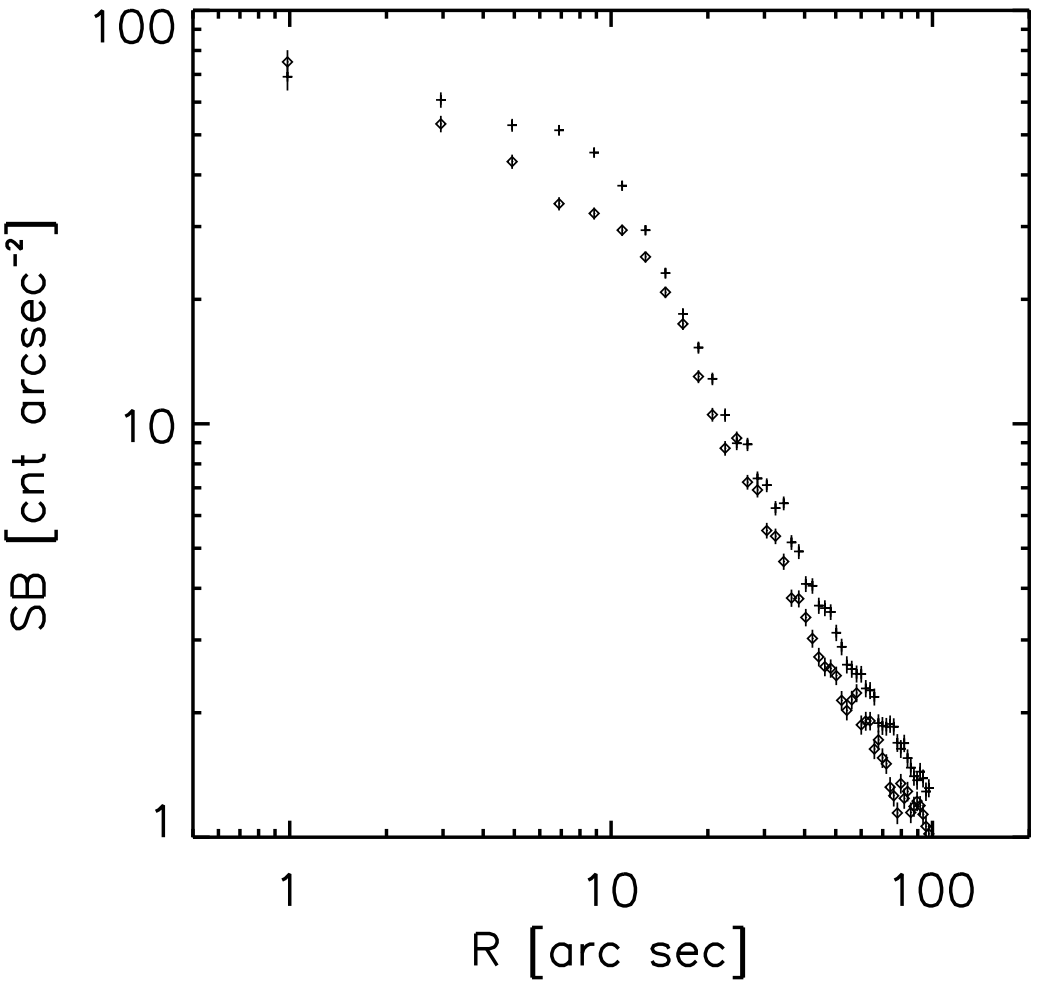

Figure 5.11: Diamond points are the surface brightness profiles along the cavity system. Cross points are the surface brightness profile with the cavity system removed.

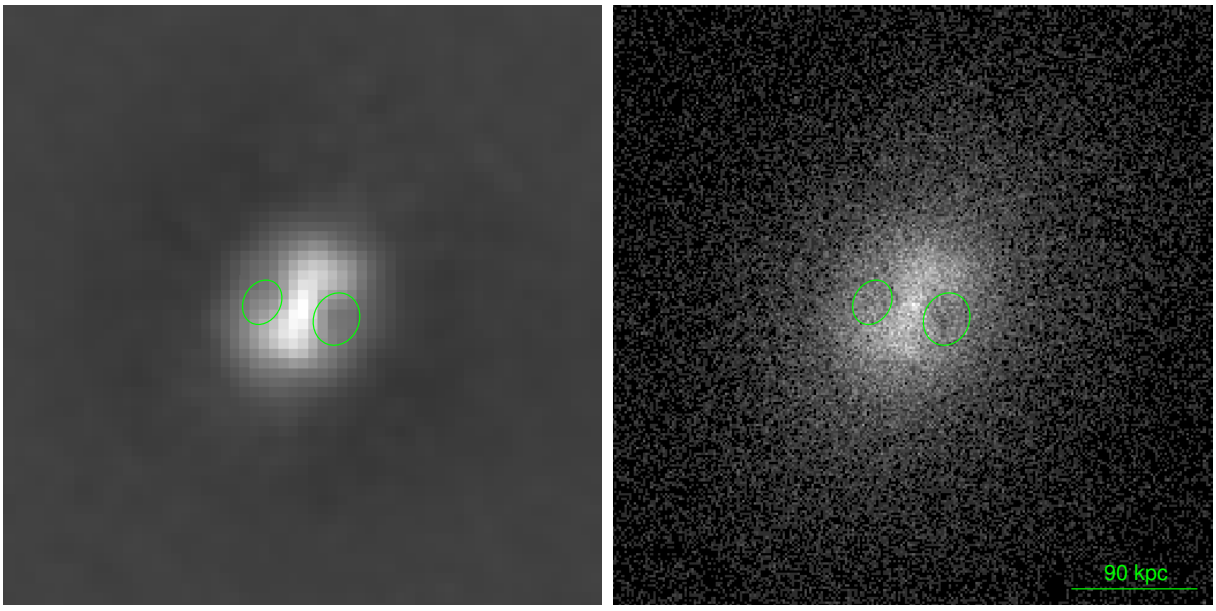

Figure 5.12: *Left*: Unsharp mask image of Zw2701. The green circles are the sizes and positions of the cavities. *Right*: X-ray image of the same region with cavities superimposed.

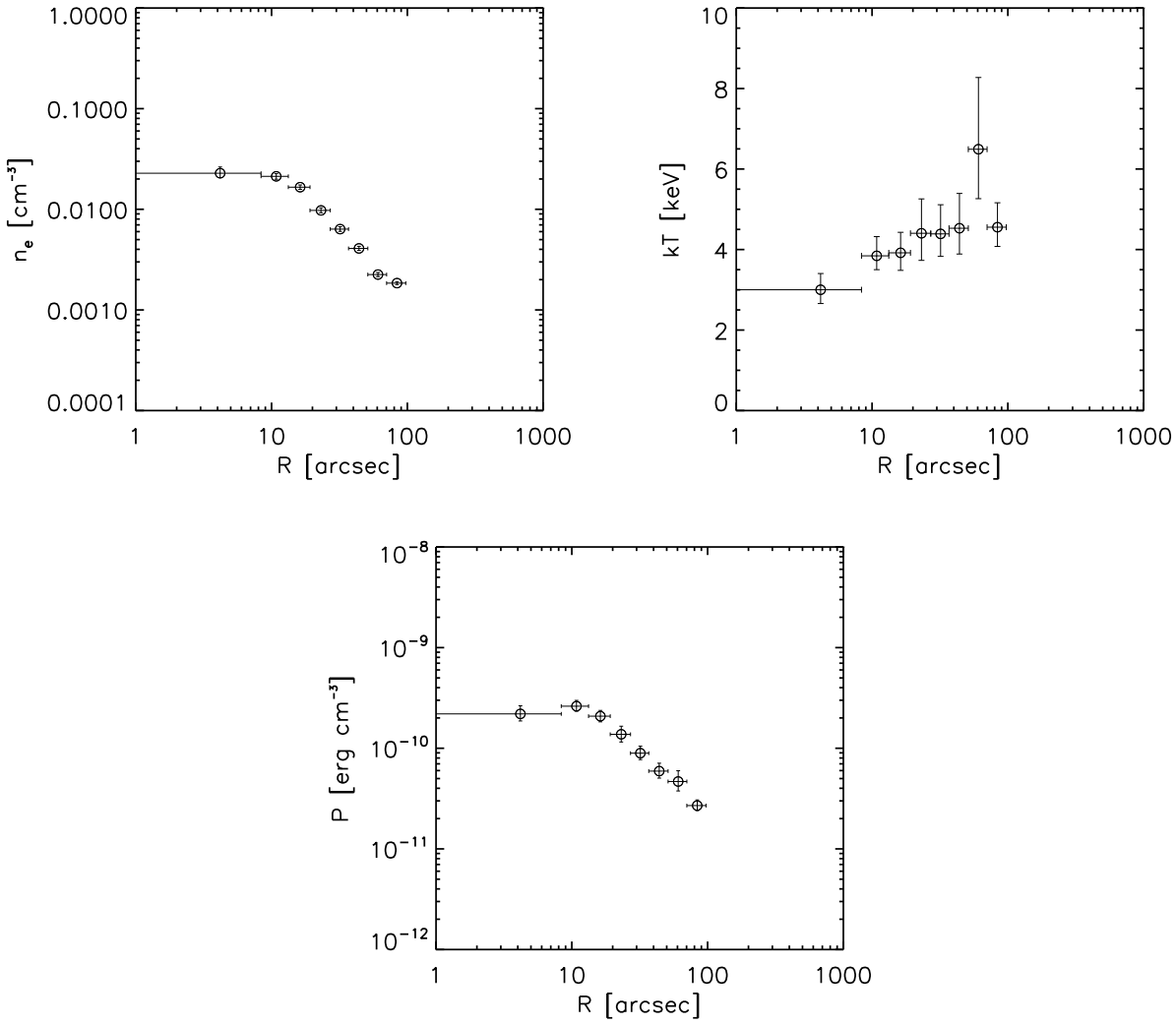

Figure 5.13: Deprojected density, temperature, and pressure profiles for Zw2701, respectively.

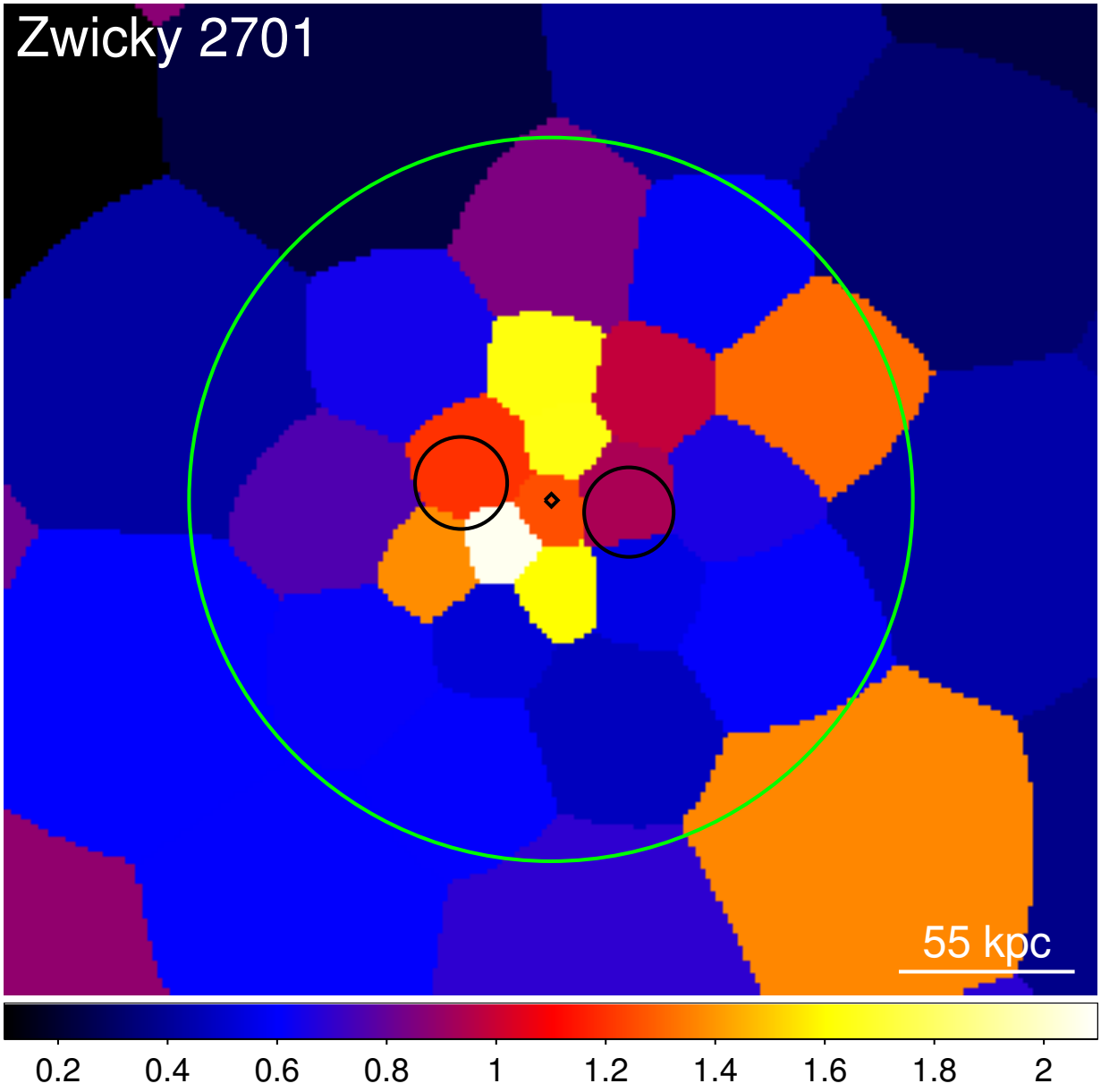

Figure 5.14: Metallicity map of Zw2701 with the updated iron radius. The iron radius is now in better agreement with what the metallicity map.

pair of cavities (Kirkpatrick et al., 2009a). We have carried out this same analysis using the high quality sample.

The first assumption we make is that the outflowing material is confined to a cylindrical volume with the same approximate radius as the cavity system. The second assumption we make is that the off-jet profile is the undisturbed, azimuthally averaged profile before an outburst. The final assumption we make is that the uplifted iron found along the jet was originally produced some where within the half-light radius of the BCG.

The uplifted iron mass is calculated as the total gas mass within the outflow region, minus the metallicity profile of the undistrubed azimuthally averaged profile. The uplifted iron mass is given as

$$M_{\rm Fe} = \rho V (Z_{\rm on} - Z_{\rm off}) A_{\rm Fe} f_{\rm Fe,\odot}, \tag{5.4}$$

where ρ is the density of the gas assuming $n_{\rm e} = 1.2 n_{\rm H}$, V is the volume of the outflow region, $Z_{\rm on}$ and $Z_{\rm off}$ are the metallicity of the gas along the jet and orthogonal to the jet, $A_{\rm Fe}$ is the atomic number of iron, and $f_{\rm Fe,\odot}$ is the iron mass fraction of the Sun. Assuming this iron came from the central region of the cluster, we can convert the iron mass values back into total uplifted mass. This is given as,

$$M_{\rm gas} = M_{\rm Fe} / (Z_\circ A_{\rm Fe} f_{\rm Fe,\odot}), \tag{5.5}$$

where $Z_\circ$ is the central metallicity value. The energy that is required to uplift this gas can be estimated by calculating the difference in gravitational potential energy at the cluster center and its current posiition. Reynolds et al. (2008) gives the energy as

$$\Delta E = \frac{c_{\rm s}^2 M_{\rm gas}}{\gamma} \ln \left(\frac{\rho_i}{\rho_f} \right), \tag{5.6}$$

where $c_{\rm s}$ is the sound speed, $\gamma = 5/3$ is the ratio of specific heats for the X-ray emitting plasma, and ρ_i and ρ_f are the initial and final gas densities.

The energy expended uplifting metal-rich gas amounts to some fraction of the total energy output by the AGN. Understanding what this value is will give us insight into the total energy history of the cluster, which we will discuss in the next section. The amount of iron lost due to an AGN outburst has been shown to be replenished on a time scale of approximately 10^8 yr (Kirkpatrick et al., 2009a). Because iron is not just accumulating around the BCG, but is being moved outward while maintaining peaked central metallicity, any given outburst must occur on approximately the same timescale. For our sample, we approximate the total output of a cluster by using the power equivalent to the iron radius given by the $P_{\rm jet} - R_{\rm Fe}$ scaling relation, and multiplying that by the outburst timescale. In

Figure 5.15, we present the fraction of energy between uplifted gas and total energy, plotted against the jet power. For any given jet power, there is much variation in $E_{\rm uplift}/E_{\rm total}$. With large uncertainties, the weighted average over the entire sample is around 14%, indicated by the dotted line.

5.4.6 Creating Broad Abundance Peaks Through AGN Activity

AGN activity has been shown here to be capable of redistributing gas at specific angles in galaxy clusters. Because this appears to be an efficient mechanism, there is reason to believe AGN could be responsible for the entire broadened abundance peak observed in cool-core clusters. We have tested the feasibility of this by calculating the amount of energy required to move the entire mass of the abundance peak from the center of the cluster to its current position using the same methods as described in section 5.4.5.

Azimuthally averaged abundance profiles have been created for the entire sample with 6 to 8 bins per profile, spanning the entire field of view of the CCD. The bin size allows for lower uncertainties and the spatial resolution to distinguish the abundance peak from the background. The profiles were fit using the method described in section 5.4.1. Only three clusters (2A 0335, A262, and A2052) were fitted using a two-temperature model in the central region. The left column of Figure 5.16 are the resulting profiles. Targets such as Persues and M87, where the field of view only covers a small part of the cluster center, have been excluded from this analysis. The dotted vertical lines indicate the effective radius of the BCG from the HyperLeda catalogue. If material was not being transported outward, this would mean the abundance peak would follow the light profile of the BCG. We first have to define what we consider a peaked abundance distribution. We start by fitting a spline to each abundance profile. Taking the derivative of the spline fit, we look for a turnover point in slope where the profile is transitioning from peaked to flat. We choose this point as the turnover in slope closest to zero, where the slope is rapidly changing interior to this point and changing more gradually exterior to this point. We refer to this turnover point as the significant abundance peak radius ($R_{\rm Z}$). The right column of Figure 5.16 is the change in slope plotted against radius. The dashed line in each panel represents $R_{\rm Z}$. The amount by which this difference between $R_{\rm Z}$ and effective radius varies appears to have a correlation with jet power. In Figure 5.17, we have plotted jet power against the ratio of $R_{\rm Z}$ and effective radius. Systems with higher jet powers have a $R_{\rm Z}$ value many times greater than the effective radius, where in lower powered systems, they are closer to being equal. The vertical dashed line highlights the point where $R_{\rm Z}$ and effective radius are the same. There are no points on or to the left of this line in our sample.

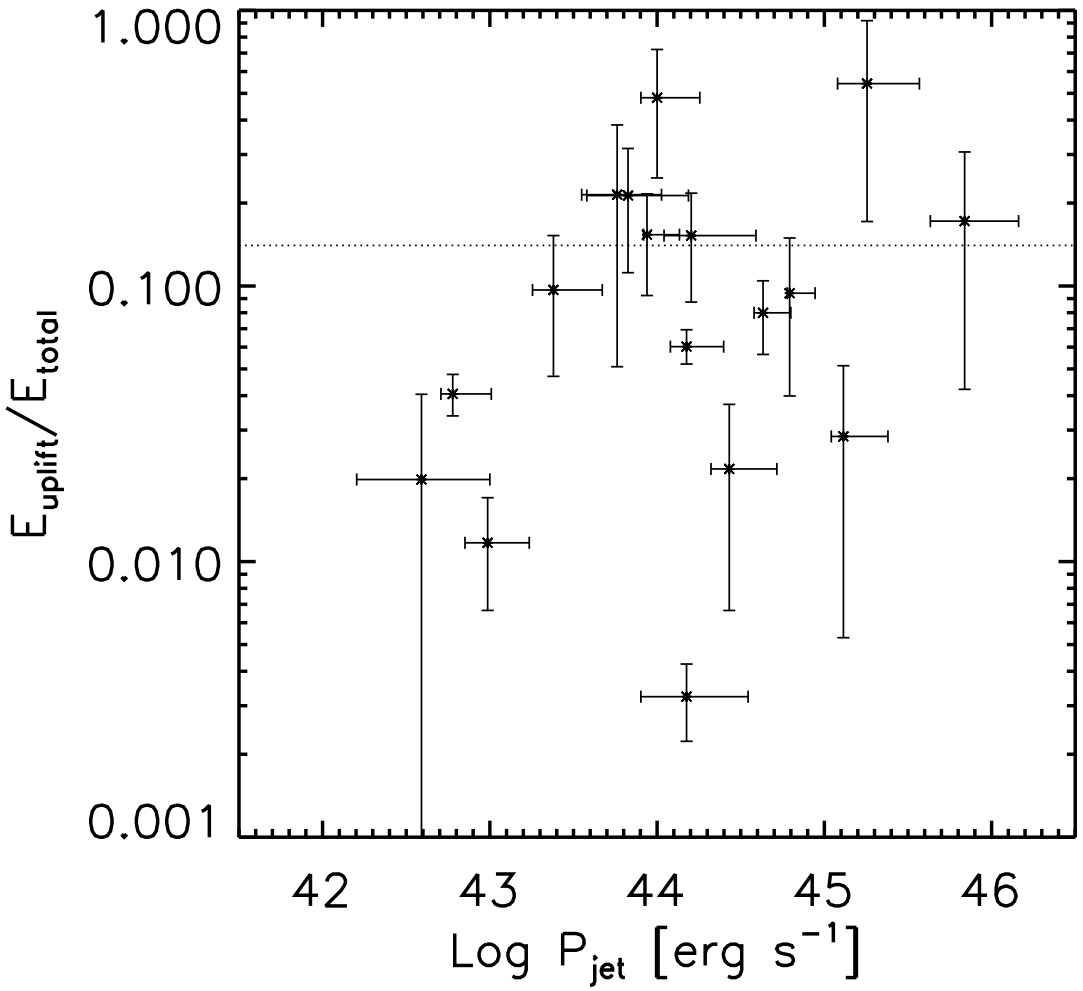

Figure 5.15: The fraction of energy used to to uplift metal-rich gas in jets to the total energy released over 10^8 yr is plotted against jet power. The dotted line is the weighted average of the entire sample.

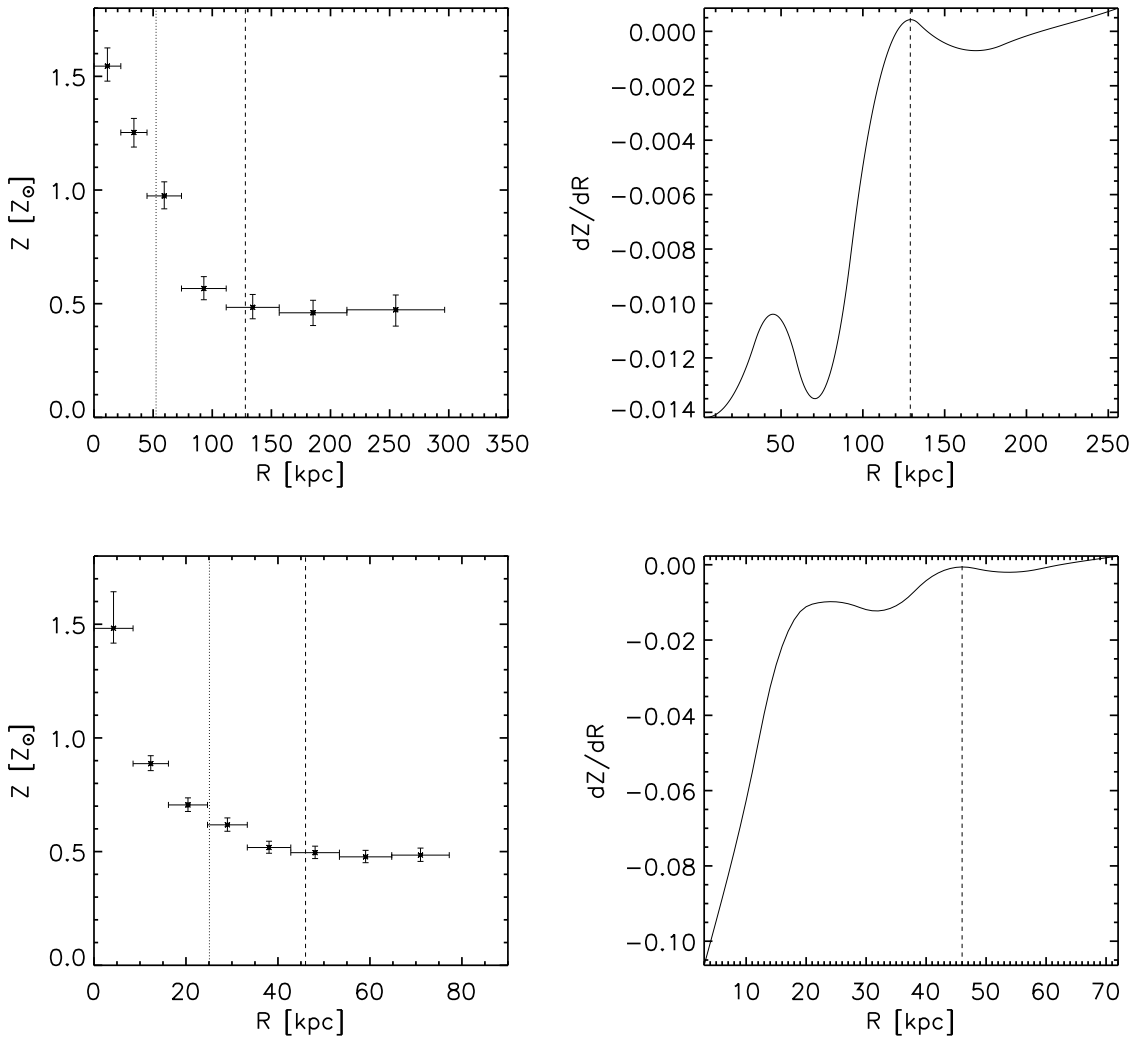

Figure 5.16: The left column of panels are the azimuthally averaged metallicity profiles for the entire sample of clusters. The dotted line represents the effective radius of the optical light. The dashed line is the radius of the entire abundance peak. This dashed line is determined by the right column of panels where the derivative of the spline fit to the metallicity profile is plotted versus radius. The top and bottom panel of this page are A133 and A262.

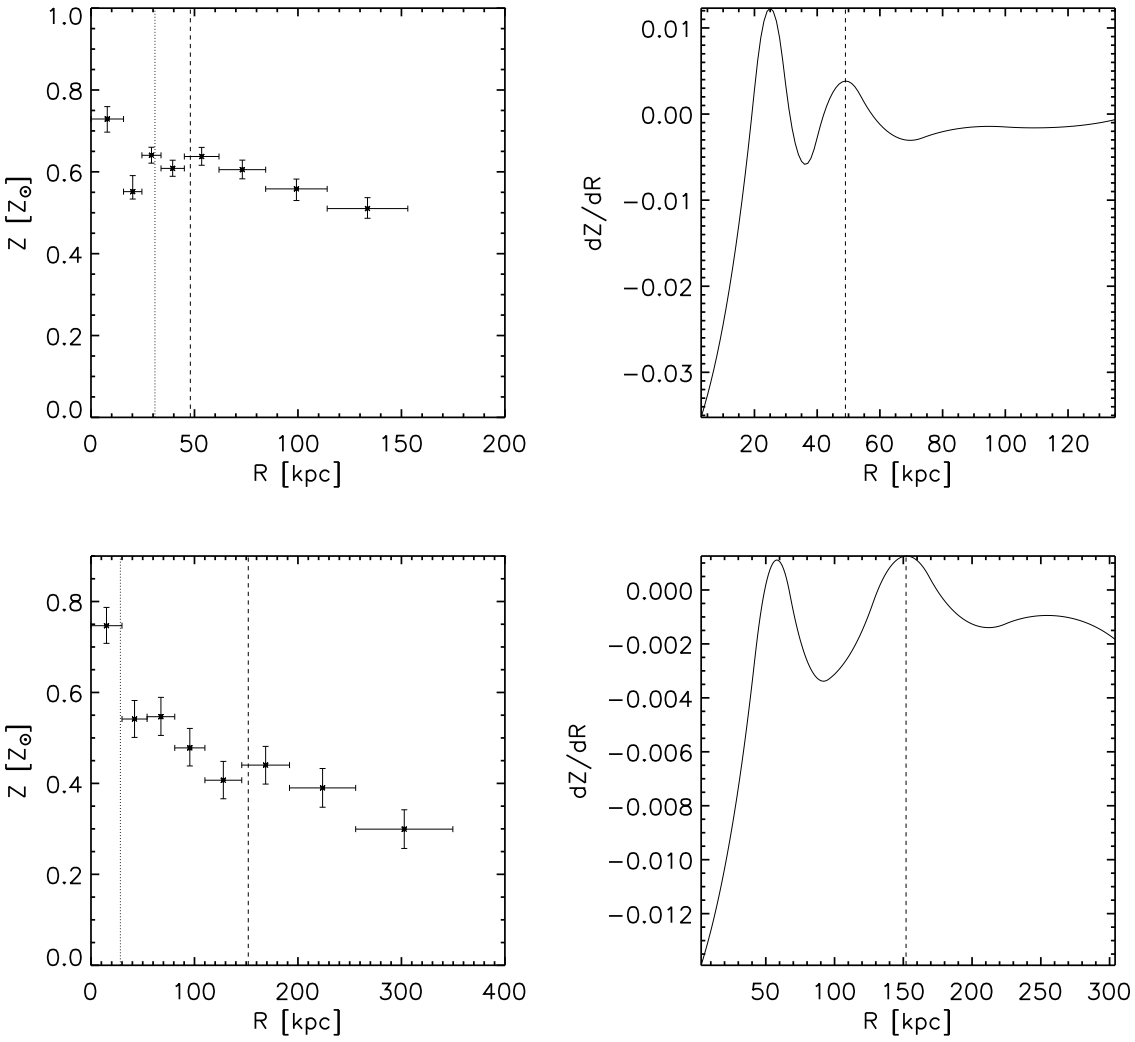

Figure 5.16: - *continued*: The top and bottom panel of this page are 2A 0335 and A478.

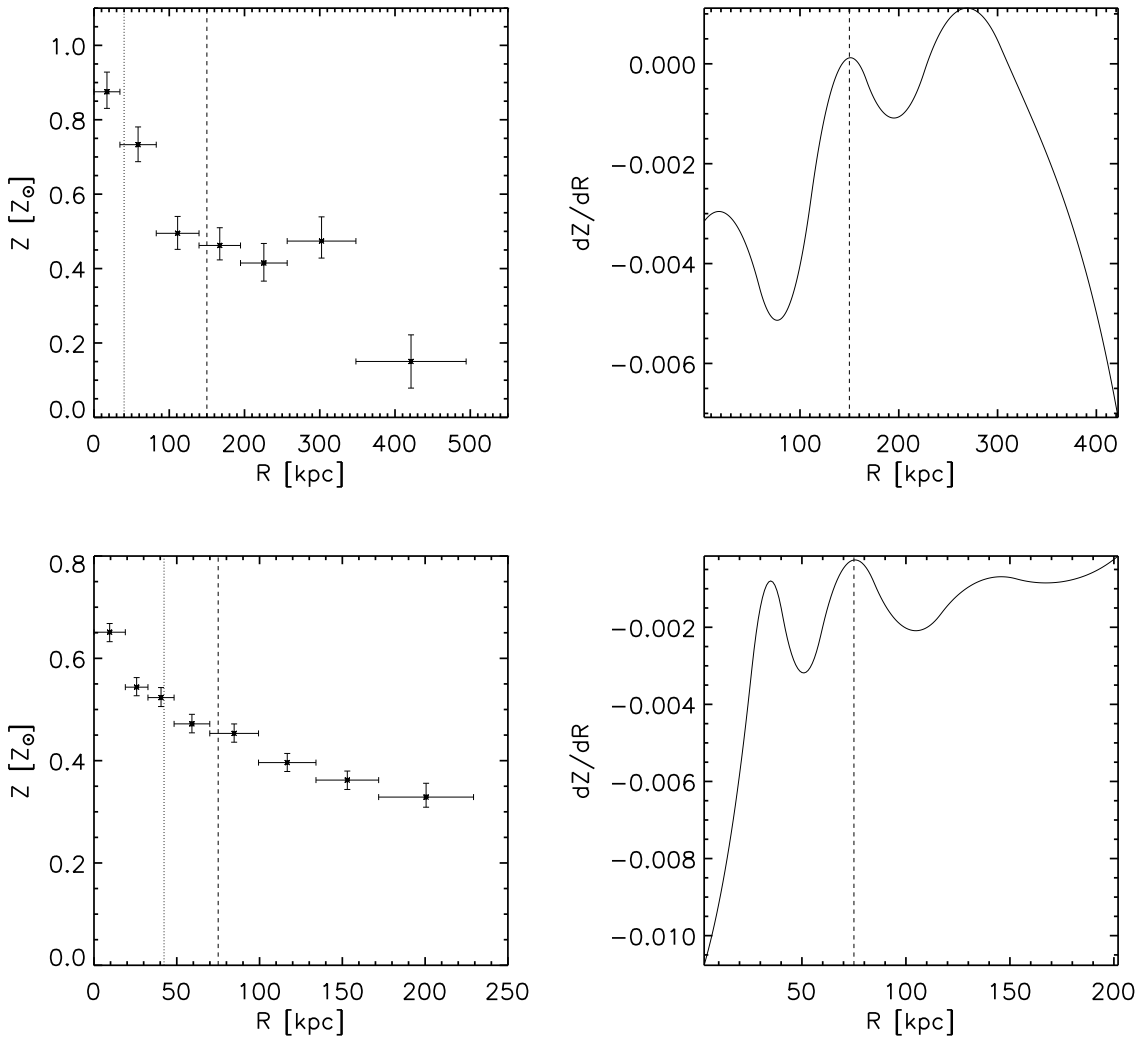

Figure 5.16: - *continued*: The top and bottom panel of this page are MS 0735 and Hydra A.

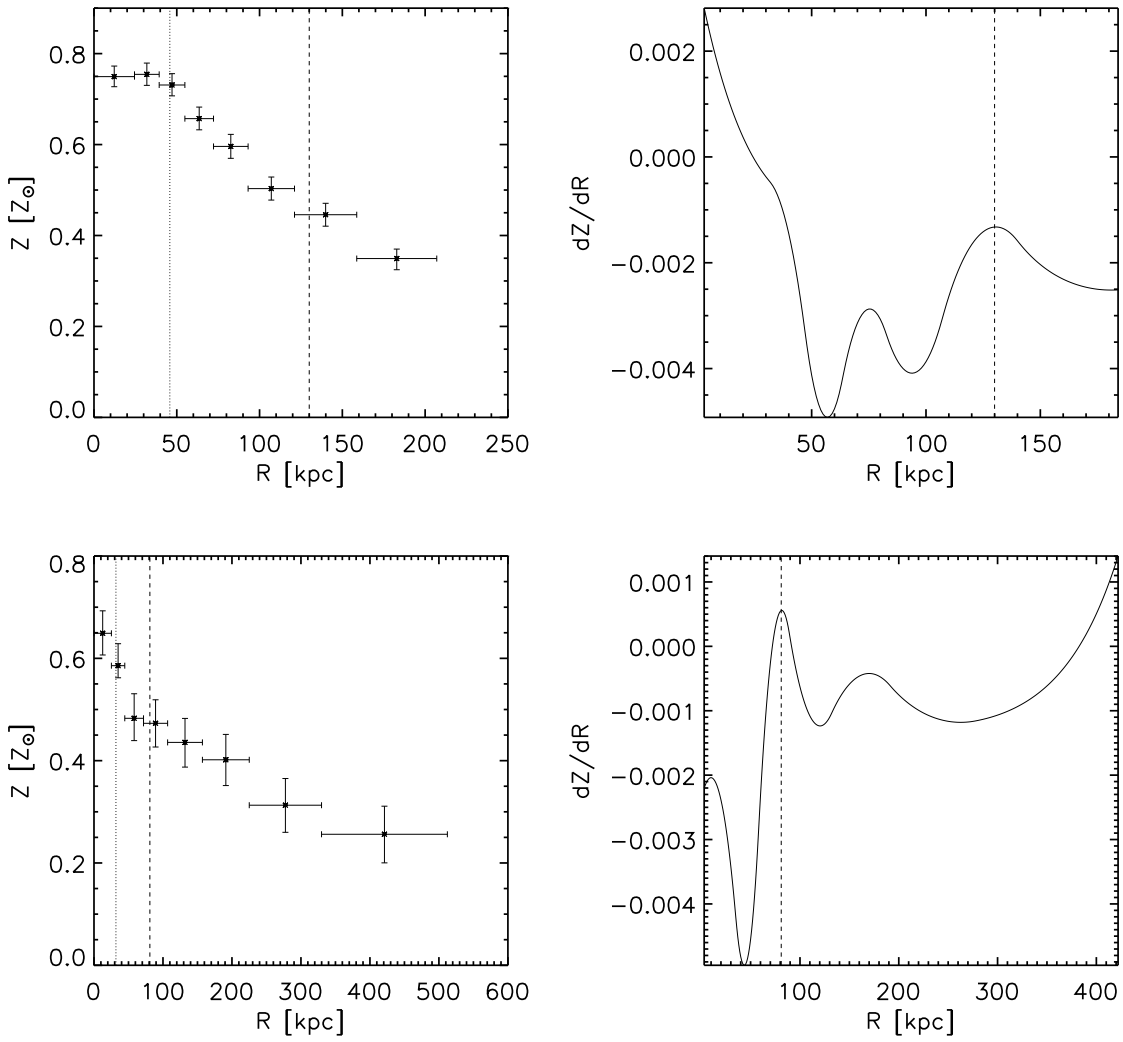

Figure 5.16: - *continued*: The top and bottom panel of this page are A1795 and A1835.

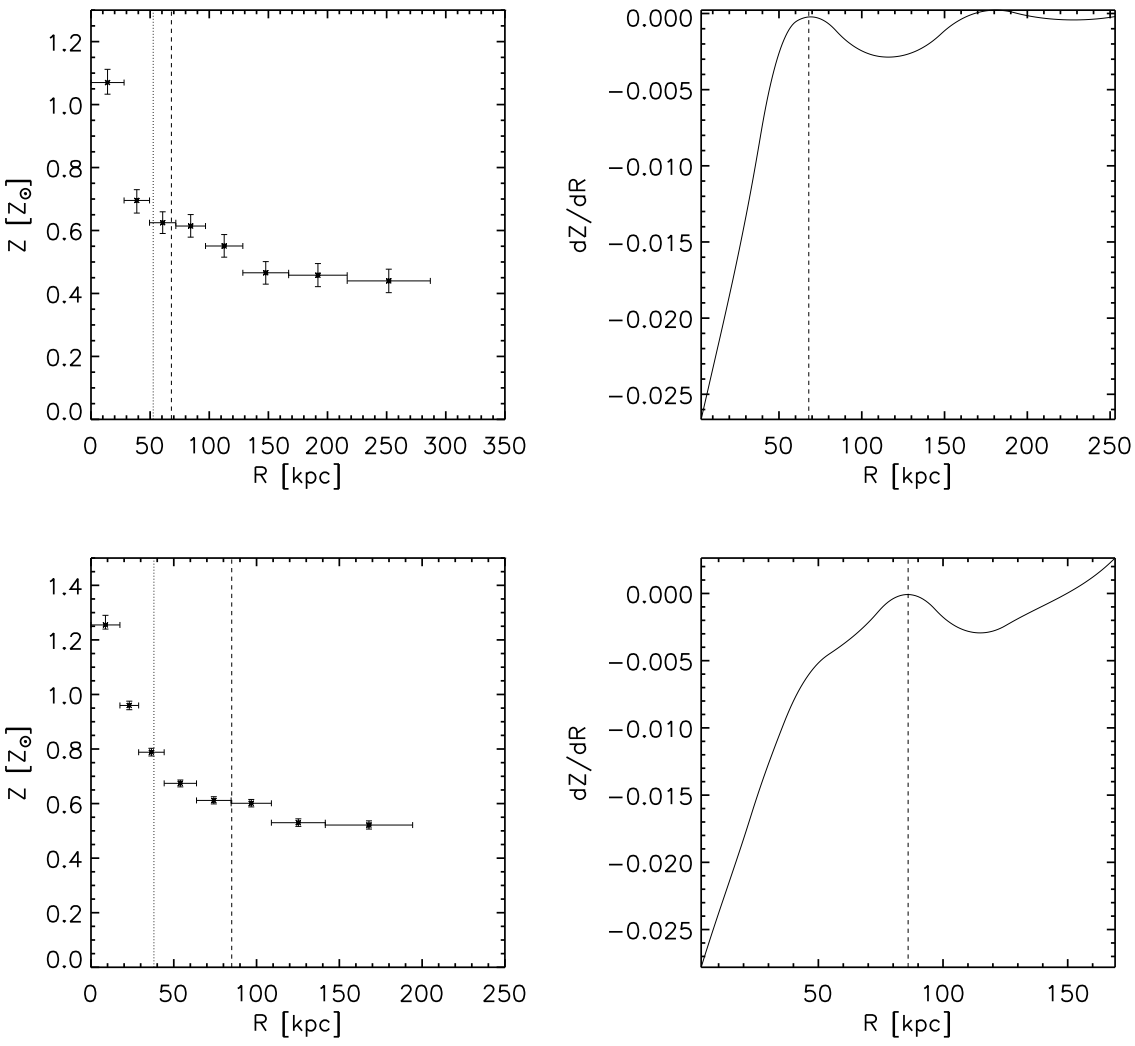

Figure 5.16: - *continued*: The top and bottom panel of this page are A2029 and A2052.

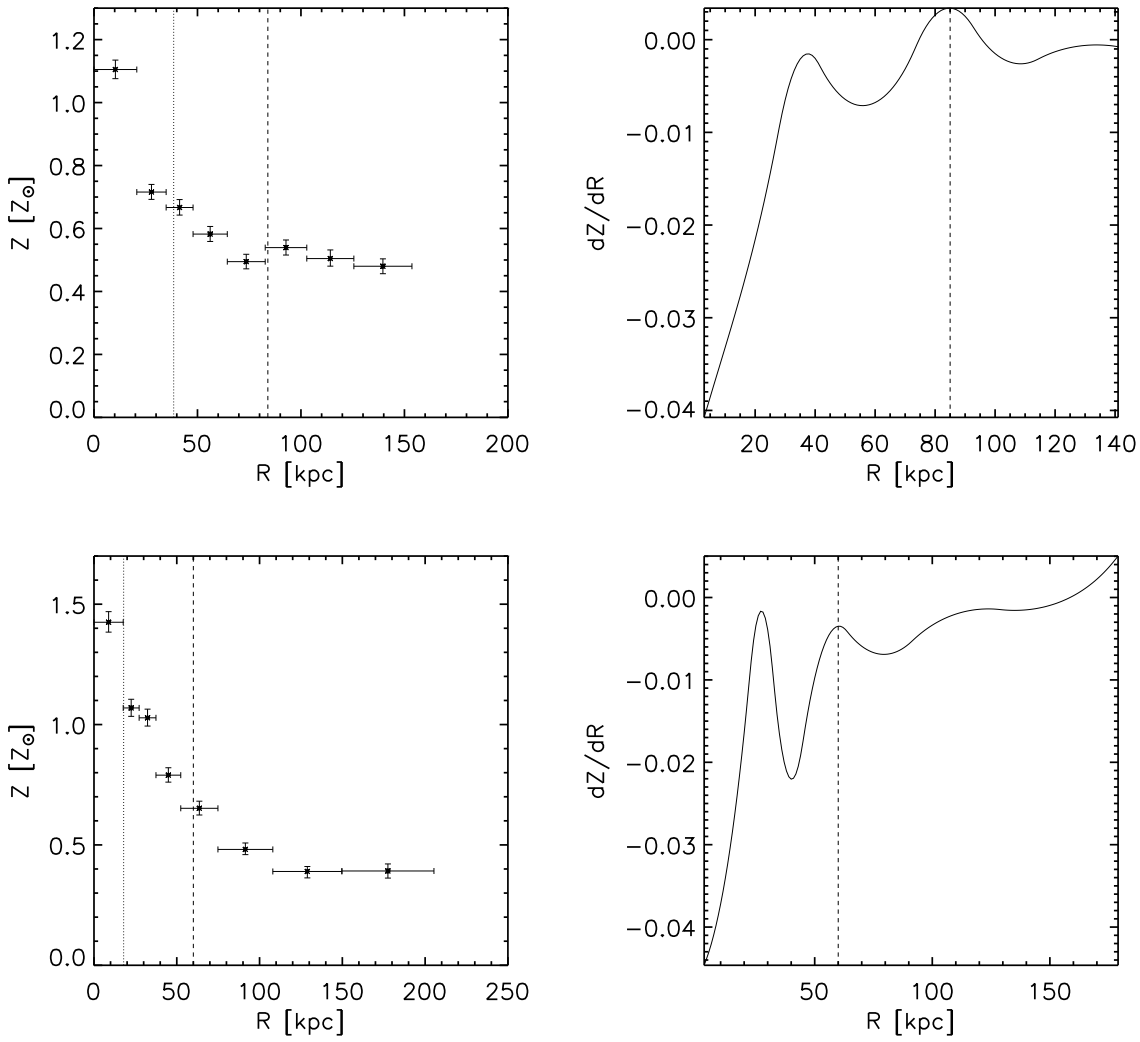

Figure 5.16: - *continued*: The top and bottom panel of this page are A2199 and Cygnus A.

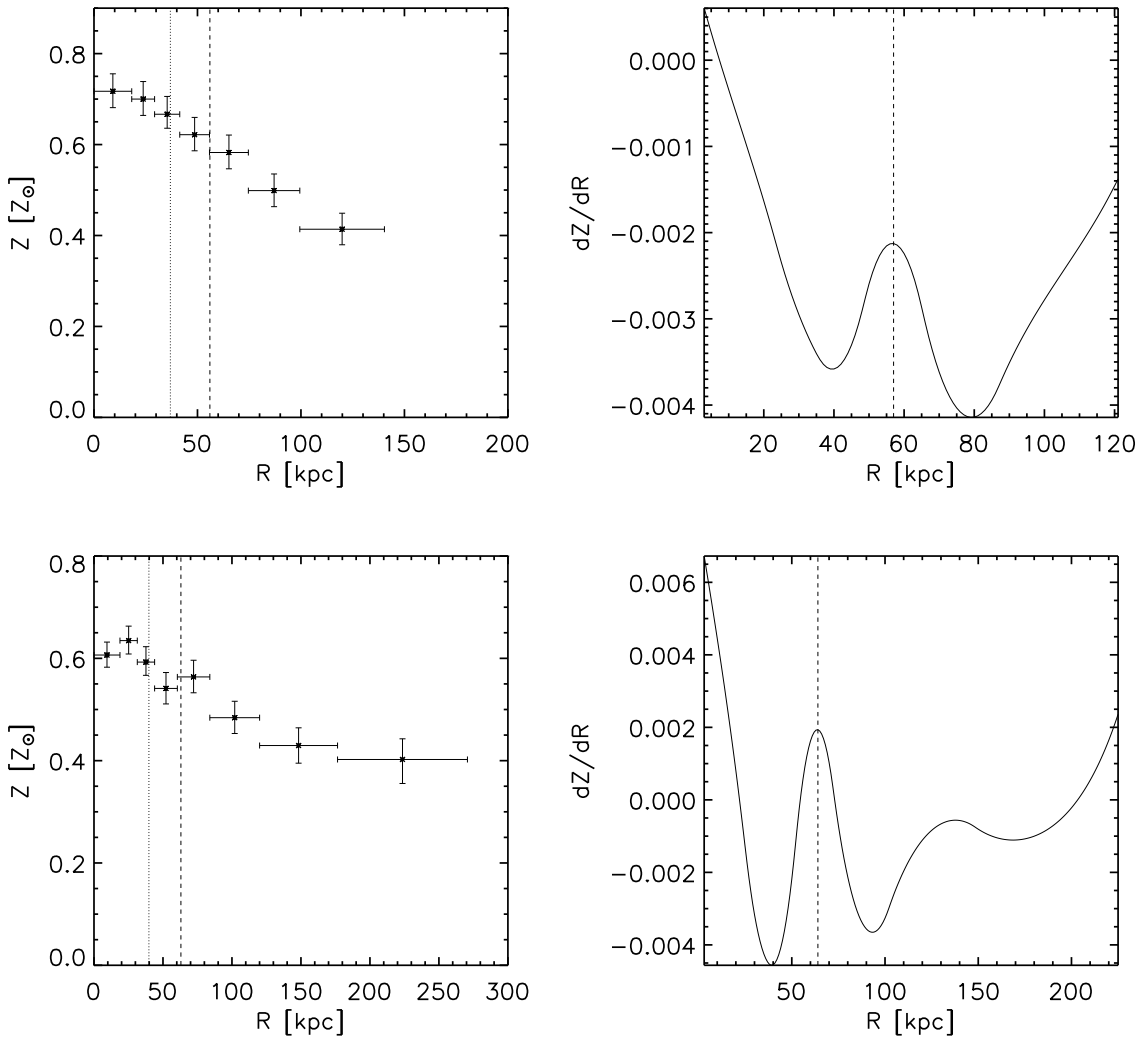

Figure 5.16: - *continued*: The top and bottom panel of this page are Sersic 159/03 and A2597.

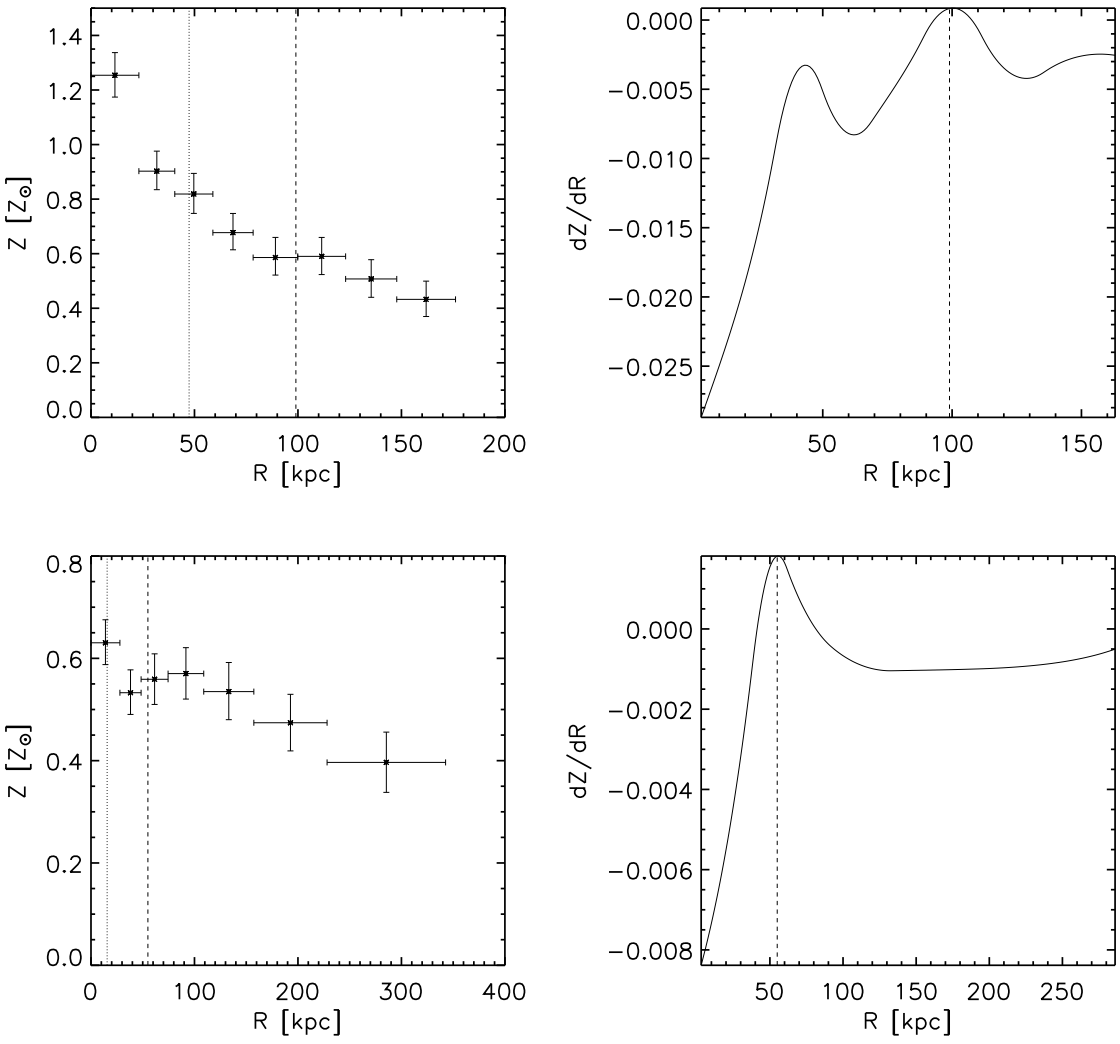

Figure 5.16: - *continued*: The top and bottom panel of this page are A85 and PKS 0745.

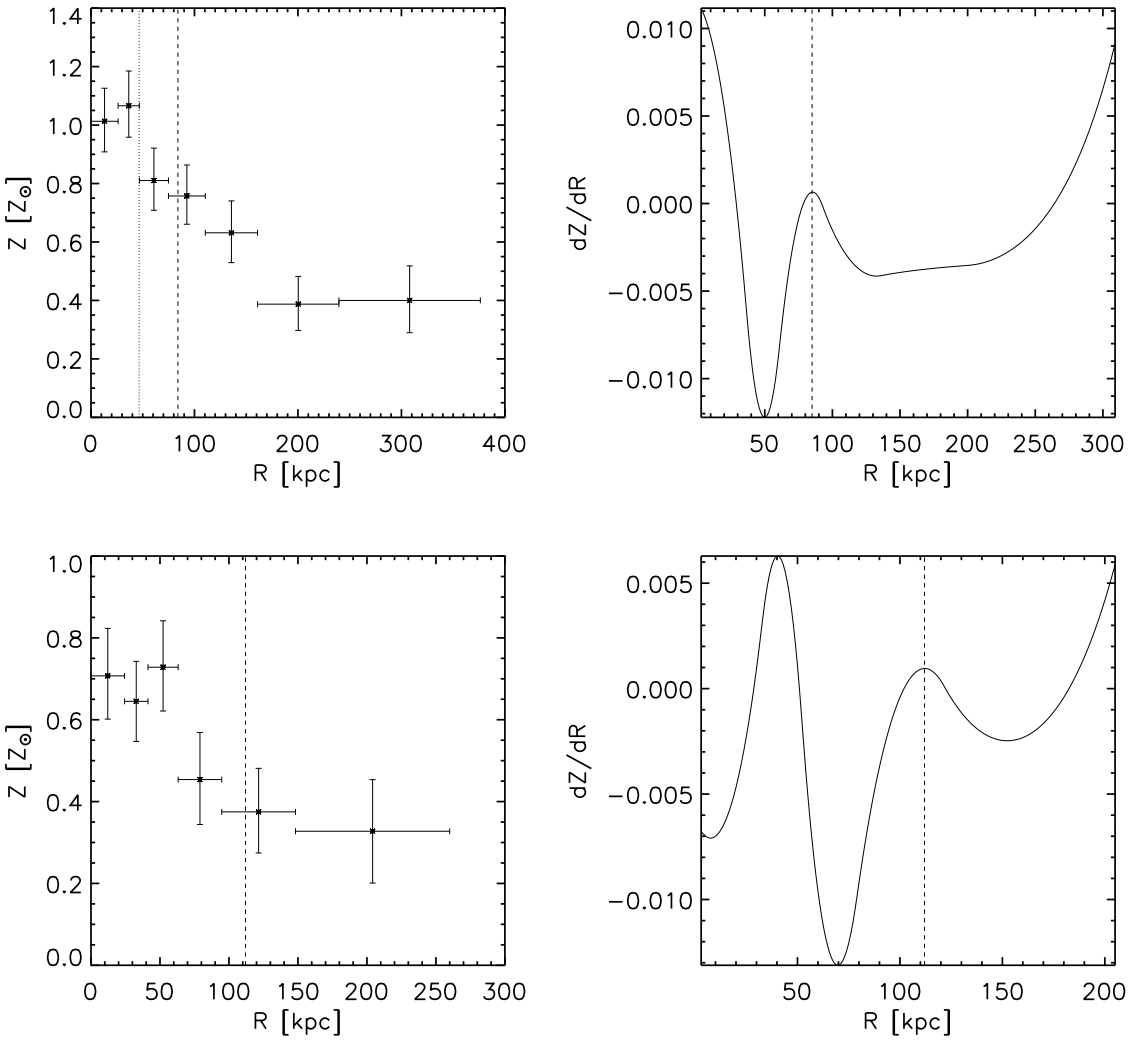

Figure 5.16: - *continued*: The top and bottom panel of this page are 4C 55.16 and RBS 797.

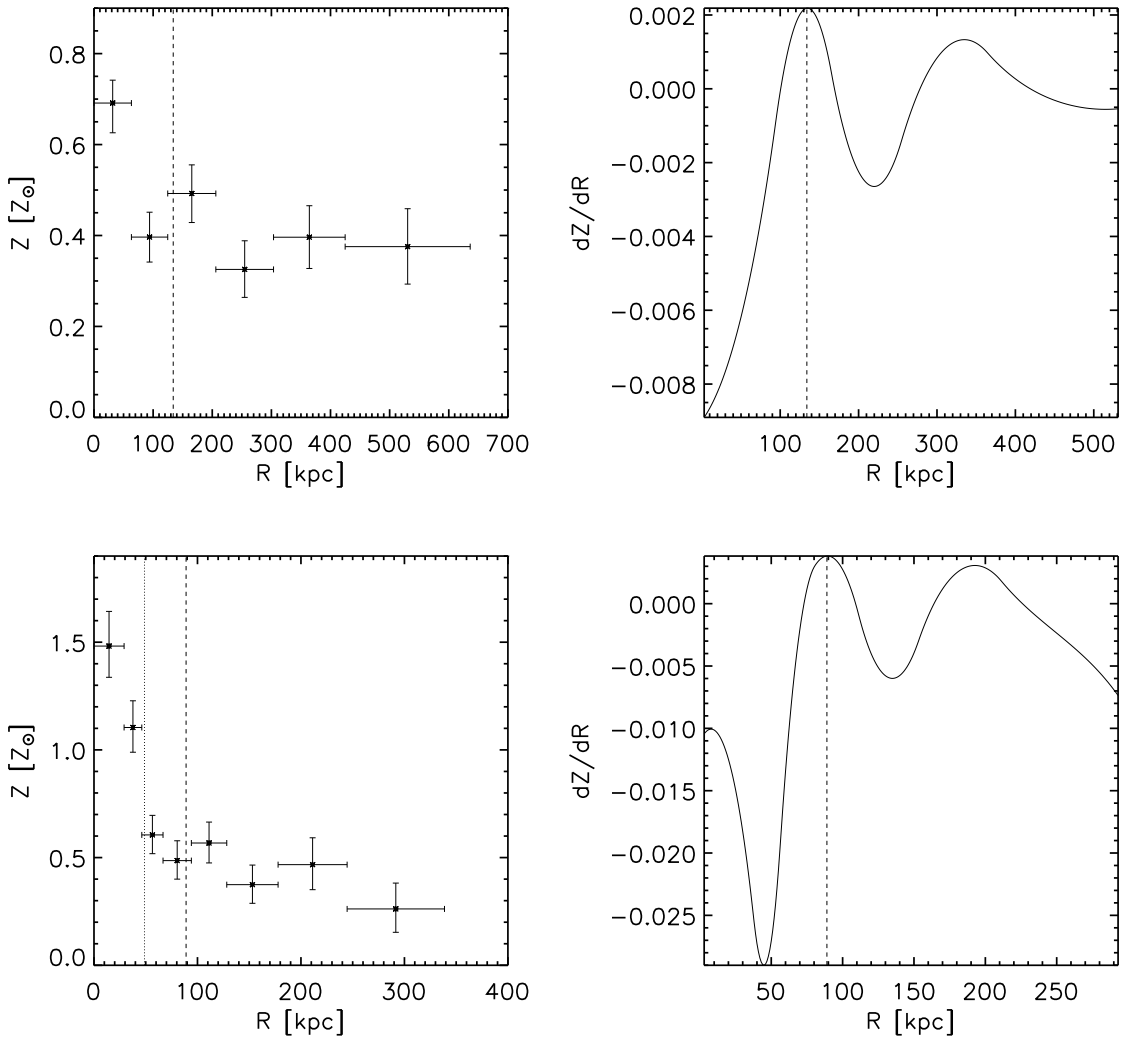

Figure 5.16: - *continued*: The top and bottom panel of this page are A2390 and Zw2701.

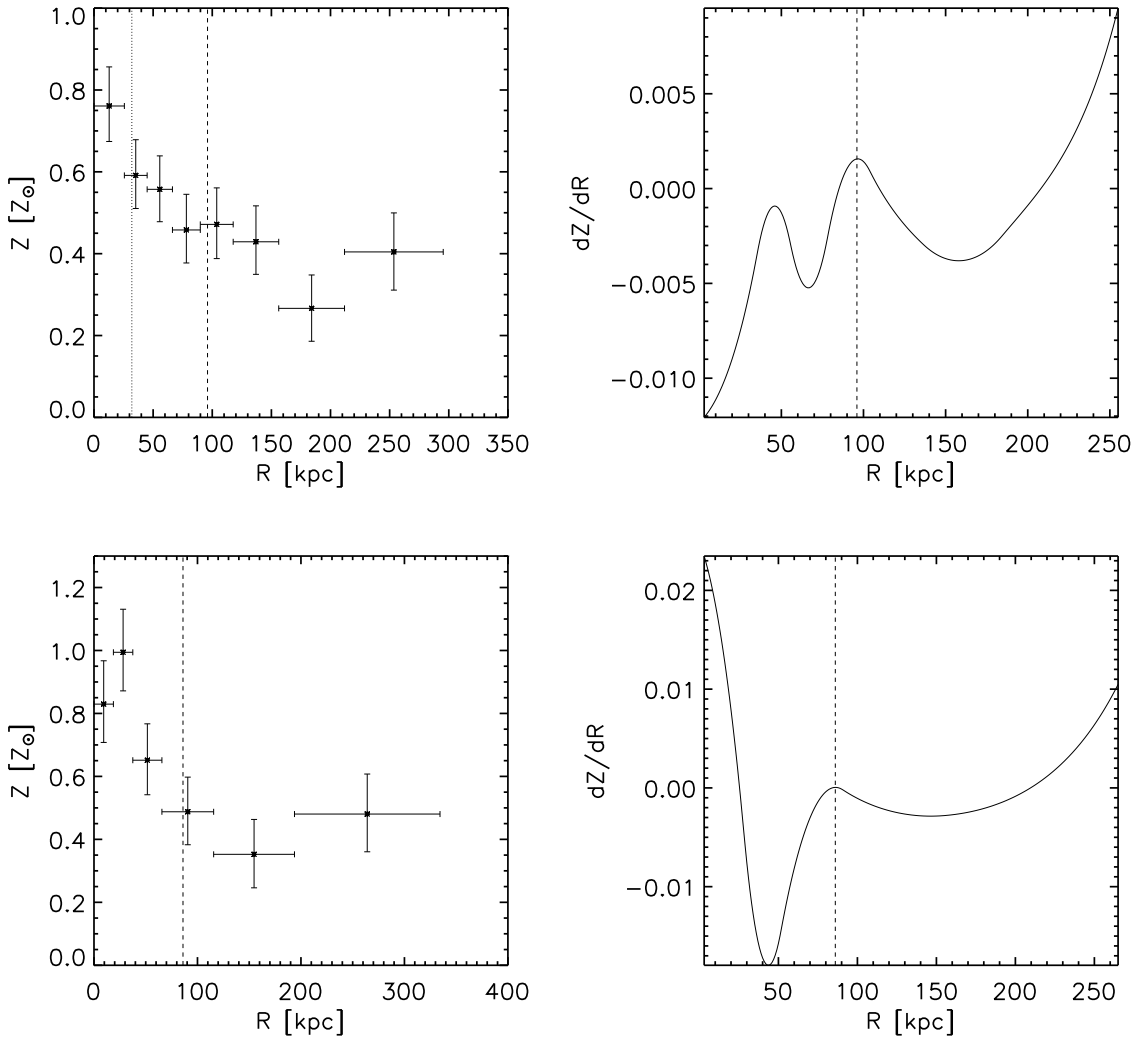

Figure 5.16: - *continued*: The top and bottom panel of this page are Zw3146 and MACS J1423.

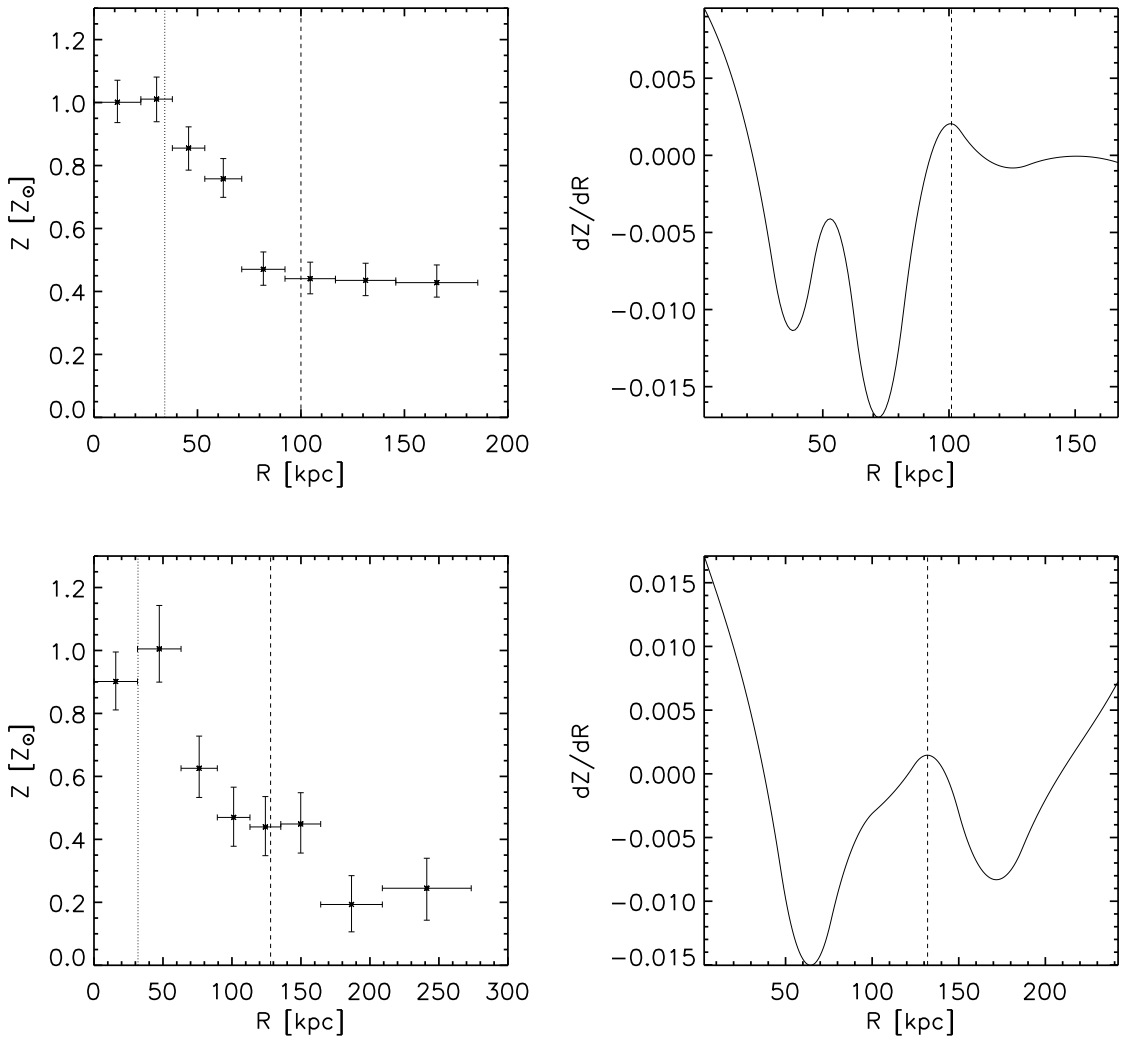

Figure 5.16: - *continued*: The top and bottom panel of this page are MKW 3S and Hercules A.

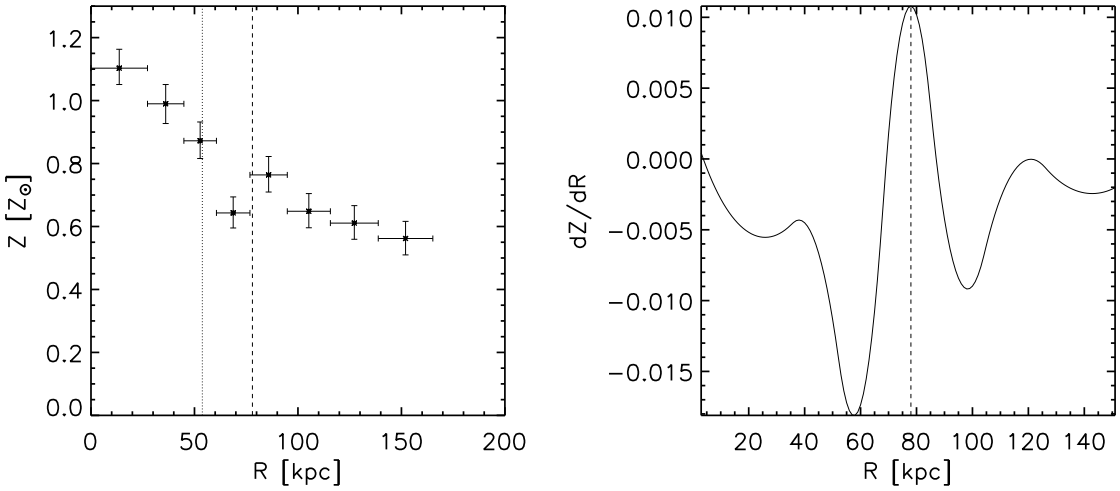

Figure 5.16: - *continued*: The top panel of this page is A4059.

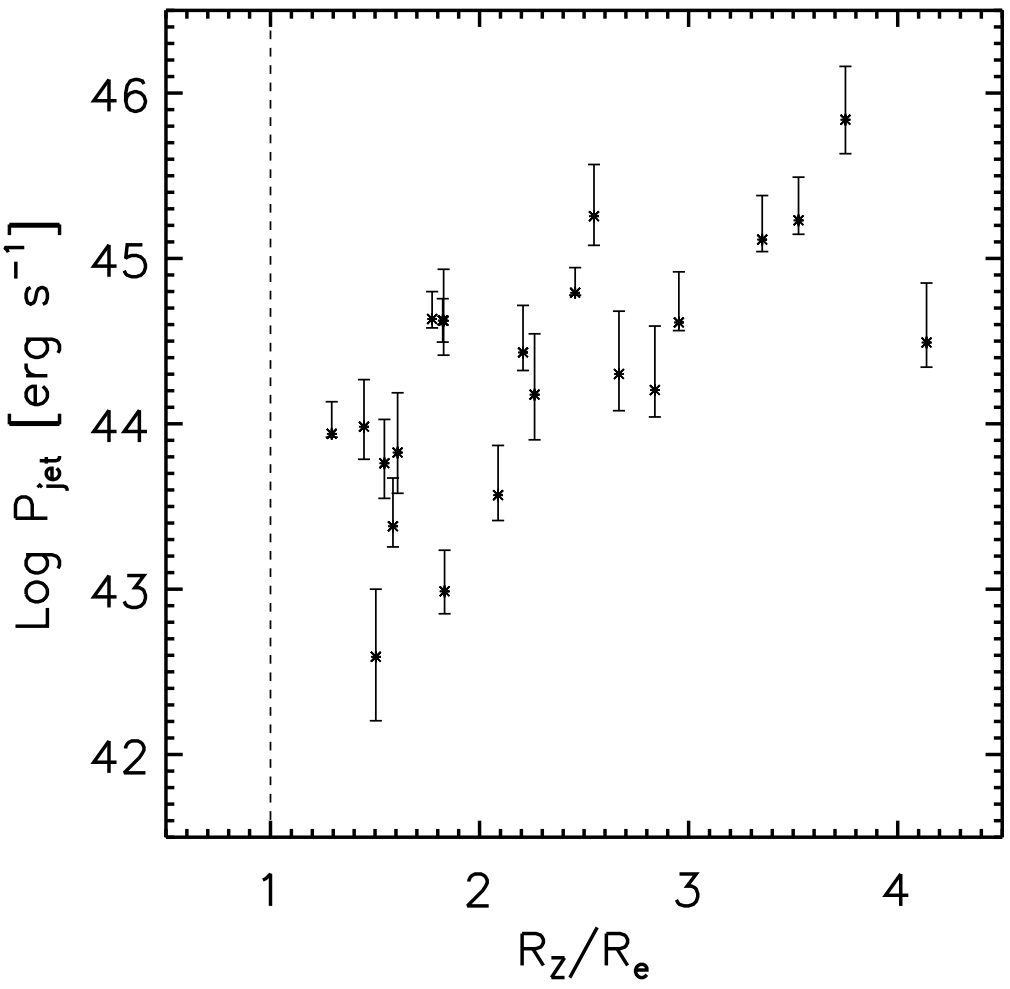

Figure 5.17: Jet power vs. the fraction of abundance peak radius to effective radius. The dashed line indicates where abundance peak and effective radius are equal. All points fall to the right of this line.

With a peak radius defined, we can now estimate the approximate metallicity background. Just as discussed in section 5.4.5, there is an expected flat abundance distribution underlying the peak. We use the average metallicity value of the profile points outside of $R_{\rm Z}$ to be the subtracted background. The modified version of equation 5.4 is now

$$M_{\rm Fe} = \rho V (Z - Z_{\rm back}) A_{\rm Fe} f_{\rm Fe,\odot}, \tag{5.7}$$

where V is the volume of the spherical shells, Z is the total metallicity, and $Z_{\rm back}$ is the background metallicity. The iron mass given here is the total iron released from SNe Ia in the BCG of each cluster. Following the same assumptions we made for the mass uplifted by a single jet, the iron mass has been converted to a total gas mass using equation 5.5. The final step is to calculate the energy to displace the total mass of gas from the center to its current observed location using equation 5.6. All values calculated here are presented in Table 5.3.

To confirm the feasibility of whether AGN are responsible for the entirety of the broadness of the abundance peak, we have determined the time scales over which the material is created by SNe Ia, and how much the SMBH must grow. If enrichment times are too long, this would indicate that some of the material is coming from another source (i.e., stripping), meaning a different mechanism besides AGN must be invoked to explain this phenomenon. Conversely, timescales that are too short would mean our abundance peak size calculations are grossly underestimated. To calculate enrichment time, the relationship used by Böhringer et al. (2004) takes into account two components, SNe Ia and stellar mass loss, that enrich the surrounding ICM with metals. The enrichment time to create all the metals in the abundance peak is given as

$$t_{\rm enr} = \left(10^{-12} S \eta_{\rm Fe} + 2.5 \times 10^{-11} \gamma_{\rm Fe}\right)^{-1} \frac{M_{\rm Fe} L_{\rm B\odot}}{L_{\rm B}}, \tag{5.8}$$

where $S = 0.15$ SNU is the supernova rate (Cappellaro et al., 1999), $\eta_{\rm Fe} = 0.7$ $\rm M_\odot$ is the SN Ia iron yield, $\gamma_{\rm Fe} = 2.8 \times 10^{-3}$ is stellar mass loss fraction of iron, and $L_{\rm B}$ is the total B-band luminosity referenced from Tables 5.1 and 5.2. Most clusters in the sample have little to no star formation in the BCG. An insignificant fraction of the total iron mass of the abundance peak is expected to originate from SN II (Kirkpatrick et al., 2009a). For most clusters in our sample, SN II only contributes at most 1% of the peak iron mass. However, A1835 stands out as exhibiting a high star formation rate between 100 and 180 $\rm M_\odot$ $\rm yr^{-1}$ (McNamara et al., 2006). At a star formation rate of over 100 $\rm M_\odot$ $\rm yr^{-1}$, the contribution of SN II would increase to over 10%. To account for this, equation 5.8 is modified to

$$t_{\rm enr} = M_{\rm Fe} \left[\left(10^{-12} S_{\rm Ia} \eta_{\rm Fe} + 2.5 \times 10^{-11} \gamma_{\rm Fe}\right) \frac{L_{\rm B}}{L_{\rm B\odot}} + {\rm SFR} \gamma_{\rm Fe,II} S_{\rm II} \right]^{-1}, \tag{5.9}$$

Table 5.3: Black hole growth and enrichment times for all clusters in the sample.

System	L_B 10^{11} $L_\odot$	Z_{back} $Z_\odot$	E 10^{58} erg	M_{Fe} 10^7 $M_\odot$	ΔM_{BH} 10^7 $M_\odot$	t_{enr} Gyr
A133	1.77	0.472	227^{+16}_{-15}	$51.3^{+1.8}_{-1.7}$	$8.16^{+0.56}_{-0.52}$	$2.66^{+0.09}_{-0.09}$
A262	0.417	0.486	$3.74^{+0.15}_{-0.14}$	$1.58^{+0.51}_{-0.35}$	$0.135^{+0.005}_{-0.005}$	$0.346^{+0.011}_{-0.008}$
2A 0335	2.56	0.558	$34.6^{+1.6}_{-1.5}$	$5.88^{+0.13}_{-0.13}$	$1.25^{+0.06}_{-0.05}$	$0.210^{+0.005}_{-0.004}$
A478	4.06	0.345	1850^{+160}_{-145}	108^{+4}_{-4}	$66.5^{+5.7}_{-5.2}$	$2.43^{+0.10}_{-0.09}$
MS 0735	1.16	0.346	1210^{+112}_{-107}	$96.5^{+4.5}_{-4.2}$	$43.5^{+4.0}_{-3.8}$	$7.63^{+0.35}_{-0.33}$
Hydra A	2.58	0.362	141^{+6}_{-6}	$17.2^{+0.4}_{-0.3}$	$5.07^{+0.22}_{-0.21}$	$0.609^{+0.013}_{-0.012}$
HCG 62	0.151	0.333	$0.858^{+0.305}_{-0.149}$	$0.455^{+0.028}_{-0.025}$	$0.0309^{+0.0110}_{-0.0054}$	$0.275^{+0.017}_{-0.015}$
A1795	1.69	0.397	900^{+36}_{-35}	$77.4^{+1.5}_{-1.5}$	$32.4^{+1.3}_{-1.3}$	$4.18^{+0.080}_{-0.079}$
A1835	3.16	0.352	588^{+69}_{-63}	$54.8^{+2.9}_{-2.4}$	$21.1^{+2.5}_{-2.3}$	$1.58^{+0.08}_{-0.07}$
A2029	1.64	0.479	207^{+13}_{-13}	$38.5^{+1.1}_{-1.1}$	$10.4^{+0.7}_{-0.7}$	$2.14^{+0.06}_{-0.06}$
A2052	0.773	0.551	$56.1^{+1.3}_{-1.3}$	$15.4^{+0.2}_{-0.1}$	$2.02^{+0.05}_{-0.05}$	$1.83^{+0.02}_{-0.02}$
A2199	2.49	0.492	$47.1^{+2.1}_{-2.1}$	$11.7^{+0.2}_{-0.2}$	$1.69^{+0.08}_{-0.08}$	$0.430^{+0.008}_{-0.009}$
Cygnus A	0.840	0.421	108^{+7}_{-7}	$41.6^{+0.9}_{-0.8}$	$3.90^{+0.24}_{-0.25}$	$4.53^{+0.10}_{-0.09}$
Sersic 159	1.34	0.498	$36.4^{+2.9}_{-2.7}$	$10.1^{+0.4}_{-0.3}$	$1.31^{+0.12}_{-0.10}$	$0.686^{+0.025}_{-0.023}$
A2597	1.57	0.439	103^{+6}_{-6}	$15.4^{+0.4}_{-0.4}$	$3.72^{+0.21}_{-0.20}$	$0.896^{+0.026}_{-0.024}$
A85	1.98	0.510	221^{+24}_{-22}	$41.1^{+1.9}_{-1.8}$	$7.94^{+0.85}_{-0.78}$	$1.90^{+0.09}_{-0.08}$
PKS 0745	0.254	0.494	$22.4^{+3.3}_{-3.1}$	$8.25^{+0.47}_{-0.45}$	$0.805^{+0.119}_{-0.112}$	$2.97^{+0.17}_{-0.16}$
4C 55.16	1.12	0.473	386^{+74}_{-67}	$71.4^{+6.0}_{-5.5}$	$13.9^{+2.7}_{-2.4}$	$5.83^{+0.49}_{-0.45}$
RBS 797	—	0.351	1660^{+409}_{-377}	122^{+13}_{-12}	$59.6^{+14.7}_{-13.5}$	—
A2390	—	0.366	251^{+54}_{-53}	$61.8^{+4.0}_{-5.0}$	$9.02^{+1.93}_{-1.89}$	—
Zw2701	1.24	0.418	$60.1^{+24.3}_{-18.1}$	$56.3^{+4.6}_{-4.1}$	$2.16^{+0.87}_{-0.65}$	$4.18^{+0.34}_{-0.30}$
Zw3146	2.07	0.367	738^{+144}_{-134}	$71.4^{+6.0}_{-5.7}$	$26.5^{+5.2}_{-4.8}$	$3.16^{+0.27}_{-0.25}$
MACSJ1423	—	0.416	855^{+206}_{-176}	$80.4^{+8.5}_{-7.9}$	$30.8^{+7.4}_{-6.3}$	—
MKW 3S	1.07	0.435	150^{+15}_{-14}	$31.8^{+1.5}_{-1.5}$	$5.39^{+0.53}_{-0.51}$	$2.73^{+0.13}_{-0.13}$
Hercules A	0.625	0.296	562^{+111}_{-103}	$69.9^{+6.6}_{-6.0}$	$28.3^{+5.6}_{-5.2}$	$10.2^{+0.9}_{-0.9}$
A4059	2.21	0.607	$40.4^{+5.0}_{-4.6}$	$14.7^{+0.7}_{-0.6}$	$2.04^{+0.25}_{-0.23}$	$0.609^{+0.029}_{-0.027}$

where SFR is the star formation rate, $\gamma_{\rm Fe,II} = 0.07$ M$_\odot$ is the SN II iron yield, and $S_{\rm II} = 0.01$ SN M$_\odot^{-1}$. The enrichment timescale for each cluster in our sample can be found in Table 5.3. The enrichment times range from a few hundred Myr to a few Gyr. This is an acceptable time scale range for all the material to have been produced within the BCGs.

For the second test of feasibility, we measure the change in SMBH mass required to output the total energy that went into uplifting all the metal-rich gas to form the abundance peak. The black hole grows by

$$\Delta M_{\rm BH} = (1 - \epsilon) M_{acc}, \tag{5.10}$$

where ϵ is the efficiency depending on the spin of the black hole and M_{acc} is the accretion mass. The black hole spin is important here because it determines the radius of the last stable orbit, which in turn determines the binding energy that can be extracted. This efficiency can range from approximately $\epsilon = 0.06$ for a non-rotating Schwarzschild black hole to as much $\epsilon = 0.4$ for a maximal spinning Kerr black hole. For this analysis we have adopted a standard value of $\epsilon = 0.1$. Accretion mass can be written in terms of the energy released, giving

$$\Delta M_{\rm BH} = (1 - \epsilon) \frac{E}{\epsilon c^2}, \tag{5.11}$$

where E is calculated using equation 5.6. The total energy that is required to uplift the gas is only a fraction of the energy a black hole will output. In section 5.4.5, in a single outburt, on average only 14% is used towards uplift. To correct for this, we add it in as another efficiency factor in our final calculations. The final changes in black hole mass are listed in Table 5.3. The range of total black hole growth in our sample are consistent with previous estimations of SMBH masses (Rafferty et al., 2006). It is likely that all of these SMBHs could have grown by the amount we are predicting. The largest outburst in our sample, MS 0735, is on the same order growth of what McNamara et al. (2009) found to be the maximum growth the SMBH must undergo to create the observed cavity system. When considering the spin of a black hole, the values reported in Table 5.3 would be reduced. Less accretion mass is needed in a spinning black hole to maintain the same output, resulting in less overall growth. At the maximal spin rate, the change in black hole mass for every cluster in our sample would be reduced by an order of magnitude.

5.5 Discussion & Summary

5.5.1 Projection Effects

Projection effects are the main unaccounted for source of error in the overall trend found in Figure 5.7. All of our pV calculations are based on the assumption that the outbursts we observe are in the plane of the sky and the line-of-sight diameter of a cavity is similar to the projected major and minor axis. It is important to understand what effect this could have on our results and final conclusion.

In all likelihood, none of the cavities in our sample are in the plane of the sky. All cavities are therefore farther from the cluster center than we measure. When calculating jet power,

$$P_{\rm jet} = \frac{4pV}{t_{\rm buoy}}, \tag{5.12}$$

this fact is a source of uncertainty in pressure and buoyancy time. Pressure is a decreasing function of radius. A cavity not in the plane of the sky would have an overestimated $P_{\rm jet}$ value. Compounding this overestimation in jet power would be an underestimated buoyancy time. Volume can either be under or overestimated, though this has been accounted for by placing reasonable upper and lower bounds for a triaxial bubble to remain stable within the ICM.

The iron radius we measure from profiles and metallicity maps suffers the same uncertainties as pressure and buoyancy times. Any angle other than directly in the plane of the sky would be cause for underestimation of the distance. Jets closer to the line of sight could potential hide any evidence of an outflow. This is a possibility for clusters in our sample such as A2052 and MKW3S. Both metallicity maps revel an asymmetric outflow. VLA imaging has reveled jets that are oriented perpendicular to one another in systems like M87 (Owen et al., 1990). With the proper orientation, an outflow could be hidden by its own counter outflow. In a case like this, both the iron radius and pV would be underestimated.

We expect this overall uncertainty to shift the $P_{\rm jet} - R_{\rm Fe}$ scaling relation to larger distances, but our overall conclusions remain the same. In Figure 5.7, most points on the trend would shift some distance down and to the left. This implies it is actually easier to move material to large distances than we have previously predicted. Cavities are also harder to detect further out in the ICM. A weak cavity depression projected onto a background of strongly peaked X-ray emission will most likely be washed out. Because the clusters in our sample were chosen due to their highly significant cavity detections, what

is likely happening are the variations in cavity alignment are small and projected cavity distances are near their true value.

5.5.2 Limits of Predicting Jet Power

As demonstrated by the $P_{\rm jet} - R_{\rm Fe}$ scaling relation, the chemical signature of the ICM can be a useful constraint in determining the mechanical power of radio jets. When cavity measurements are ambiguous, its is not always feasible to obtain longer X-ray observations or high resolution radio mapping for every cluster that may have a cavity system. The extended sample showed that a rough estimation of metallicity can indicate whether or not these extreme powered jets at high redshifts are indeed as powerful as thought. The metallicity map of Zw2701 showed signs that the jet power may be an order of magnitude lower. Follow up observations helped confirm that the cavities were smaller than originally measured using a short, single exposure observation. A85 and 4C 55 both show signs there may be unaccounted for power in those systems. Still, clusters like PKS 0745 and Zw3146 have very ambiguous metallicity maps that reveal no more insight into their thermal history. This proves the limits of our technique and that decent photon statistics are required to obtain meaningful metallicity measurements as well as cavity detections.

5.5.3 AGN Can Account for the Entire Abundance Peak Distribution

There is enough energy and production of material for AGN to be solely responsible for the broadly distributed abundance peaks in cool core clusters. Across our sample, it takes on average 2 Gyr to produce all the iron enriching the abundance peaks through the process of SN Ia explosions, stellar mass loss, and core-collapse supernovae associated with star formation. The change in black hole mass associated with the energy required to uplift gas ranges from 10^5 - 10^8 $M_\odot$. This range is less than the expected masses of SMBH in large BCGs and is consistent with previous predictions of expected growth. Adding black hole spin to the calculation lowers the threshold for the amount of accretion material need for equivalent energy output. We believe because of these easily achievable standards, AGN are the prime mechanism for redistributing all the metal enriched gas associated with the BCG.

Chapter 6

Conclusion

This thesis has attempted to answer the question of what is the mechanism responsible for the distribution of iron-rich gas throughout the ICM. It has been known for a number of years that the centers of cool-core clusters harbor large quantities of iron-rich gas, and that this gas is directly connected to the presence of a BCG. It has also been a known fact the iron-rich gas is much more widely distributed than the originating SN Ia would be cable of ejecting. Others have quantified how much distribution has taken place and have speculated about the energy source. What has not been answered until now is what phenomenon, and under what condition, directly correlate with the currently observed distribution of the ICM. Our hypothesis was that AGN are solely responsible mixing the iron-rich gas.

We have addressed this problem by assembling a sample of 29 cool-core galaxy clusters all exhibiting AGN activity in the form of cavities and radio emission. This sample was based on a subset of clusters from Rafferty et al. (2006), where they have measured the jet power of every object using the total energy of the cavity, or the enthalpy $E = 4pV$, output over the buoyancy time of the cavity. All X-ray data have been drawn from the *Chandra X-ray Observatory* archive. The clusters studied range in redshift from nearby to $z = 0.54$. They also display a wide range of power from 10^{42} - 10^{46} erg s^{-1}. Our methods of analysis included the spectral fitting of metallicity profiles at various sectors along the radio jets, and sectors with no radio jets, which are usually orthogonal. Two-dimensional metallicity maps were also created as a tool for identifying interesting features.

6.1 Summary

Below is the summary of our results.

- Poor fitting single-temperature models in the central, coolest region of the ICM require multi-temperature components. In the course of fitting thousands of individual spectra, when a region was found to fit poorly at spectral energies above 3 keV, it correlated with the spectrum's location in either the very center of a cluster, or a cold outflow region. Spectra exhibiting this quality would underestimate the metallicity. The Fe-L complex will have a broader spectral shape if being excited by a range of temperatures above and below 1 keV. If force fitting this feature with a single temperature model, the model will assume the Fe-L complex is depressed, resulting in an underestimated abundance measure. This is an important problem to fix when attempting to make subtle comparisons in metallicity between adjacent regions. We have taken care to employ two temperature models where we have demonstrated single temperature spectral fitting has failed, and not haphazardly applying it in any situation to suit our own needs.

- It is possible to distinguish significant variations in metallicity between radio jet and undisturbed regions. We started our analysis with Hydra A because being one of the most powerful known outburst in the Universe, as well as being at a nearby redshift and having deep *Chandra* data, it was the most likely target to exhibit measurable differences in metallicity along the radio jet outflow, and regions undisturbed by the AGN. By isolating six separate profile sectors, two containing the north and south jets respectively, and four sectors adjacent to both jet sectors, the resulting metallicity profiles not only showed a distinguishable difference between a jet and its surrounding area, but the effect was large. Not only that, but we demonstrated an AGN outburst could move material over 100 kpc.

- Jet power is correlated with iron radius. We reproduced the Hydra A analysis with 10, and then 17 total clusters. Over a range of 4 orders of magnitude in power and hundreds of kiloparsecs in displacement, a tight correlation between the jet power and iron radius was found. Iron radius is defined as the farthest point from the cluster center on a metallicity profile containing a radio jet is significantly higher in metallicity than the back ground metallicity. The P_{jet} - R_{Fe} scaling relation is given as

$$R_{\rm Fe} = (61 \pm 6) \times P_{\rm jet}^{(0.43\pm0.01)} \text{ (kpc)},$$

with $P_{\rm jet}$ in units of 10^{44} erg s^{-1}. Unaccounted for uncertainties due to projection effects cause an underestimation of the iron radius.

- AGN are capable of redistributing the SN Ia ejecta from the BCG to its current observed location. We have shown when considering all the gas mass associated with the BCG, the timescale necessary to produce that much material, and energy released by the SMBH to uplift it all, are on reasonable scales. We first had to quantify what constitutes an abundance peak. We achieved this by taking the point on the derivative of the metallicity profile where the slope transitions from rapidly decreasing slope to zero slope. The metallicity outside the abundance peak is considered background from core-collapse supernovae ejecta from early in the cluster formation. With iron masses for just the material from SN Ia originating in the BCG, we calculated enrichment times based on B-band luminosities. These times ranged on average between hundreds of Myr to a few Gyr, similar to the lifespan of the cluster. Using the same method used in the jet profile analysis for calculating uplift energy, we related that energy to black hole growth. The SMBHs in our sample grew between 10^5 - 10^8 $M_\odot$ in order to transport all the peaked iron-rich gas to its current position. These are well within what is expected for the amount by which a SMBH will grow over its lifetime in a galaxy cluster.

6.2 Future Work

This thesis did not look at the effects of AGN and metallicity in giant elliptical galaxies. This is interesting because the $P_{\rm jet}$ - $R_{\rm Fe}$ scaling relation may differ for these types of systems due to their much smaller gravitational potential wells. One difficulty in need of surpassing is our method of spectral modeling. Our current method does not work for these systems. We assume the metallicities are tied to the same ratios as the sun; when applying this to the spectral fitting of an elliptical galaxy X-ray halo, the fit fails. In order to get accurate metallicities, α-elements must be allowed to be fit independently from iron and nickel. The challenge then is understanding the internal ratios between α-elements in this new method of fitting.

APPENDICES

Appendix A

IDL Pipeline Routine for Preparing *Chandra* Data

A.1 Pipeline

In this appendix we describe the entire pipeline procedure all data used in this analysis was processed by. All IDL routines assume you are operating within the unzipped ObsID directory downloaded from the *Chandra X-ray Observatory* archive unless otherwise noted. Processing was carried out on a G5 PowerPC running OS X 10.4.11 with CIAO version 4.1.2 and CALDB version 4.1.2. This pipeline has not been tested and may not work on any other platform or CIAO version.

The only required routines outside of what is listed in this appendix include the standard IDL library and the IDL Astronomy User's Library. Files can be downloaded at http://idlastro.gsfc.nasa.gov. Xspec 11 is also required for spectral fitting.

- **pipeline.pro** [, *chipid*1, *chipid*2]

  Runs the entire pipeline from start to finish.

  > *chipid*1, *chipid*2 - Chip ID variables represent the ACIS chip range intended for use in analysis. Inputs accepts (0,3) for ACIS-I obsersvations and (7,7) for ACIS-S observations. *Notes*: not tested for different aimpoint.

  Routines called within *pipeline.pro*.

- **file_prep.pro**

  Unzips all files and sets up folder structure within ObsID folder. Cluster and CCD regions are created manually in DS9. Cluster region (cluster.reg) masks the central bright region during background normalization. CCD region (ccd.reg) is used to crop out unused CCDs in event 2 file.

- **data_prep.pro**

  Follows CIAO thread for creating new level=2 event file.

- **blanksky_bg.pro** [, *chipid*1, *chipid*2]

  Follows CIAO thread for creating ACIS Blank-Sky background files.

- **create_exposure_map.pro** [, *chipid*1, *chipid*2, *spectra_dir* = *spectra_dir*]

  Creates exposure maps for specified CCD range. CIAO tools used within this routine include *asphist*, *mkinstmap*, and *mkexpmap*.

- **remove_ptsrc.pro** [, *obsid*]

  Points sources are removed after all observations for a single target have been run through *pipeline.pro*. The final cleaned event 2 files for each ObsID are merged into one combined image.

  obsid - String array of all working directories for each observation. All event 2 files are reprojected to the coordinates of the first observation in the string.

  Routines called within *remove_ptsrc.pro*.

  - **merge.pro** [, *obsid*, */ptsrc*]

    Merges event 2 files using the CIAO tool *merge_all*. /ptsrc flag is required when merging files within *remove_ptsrc.pro*.

- **create_annuli.pro** [, *xc*, *yc*, *mincnts*]

  Circular annuli are automatically generated with the specified minimum amount of counts per annuli.

  xc - X-coordinate for X-ray center.

  yc - Y-coordinate for X-ray center.

  mincnts - Minimum desired counts per annuli.

- **autoext.pro** [, *a*, *b*, *dir*, */deprojected*]

  Automatically extracts spectra from CIAO regions that follow the naming convention regX.reg, where X begins at 1 and ascends in numerical order.

  a - Total number of regions to be extracted.

  b - Multi-spec sequence number. This should be a unique integer identifying each individual observation for a single target.

  dir - Name of the directory within /spectra directory where region files are located.

  /deprojected - Set this flag if the series of regions will be used in a deprojected X-ray analysis.

  Routines called within *autoext.pro*.

  - **mextract.pro** [, reg_file, $file\_name$, *dir*, */deprojected*, $rad = rad$, $sang = sang$, $eang = eang$]

    Sets up and runs the main spectra extraction routine (*wextract.pro*). PI pectrum files are renamed to follow the standard naming convention of the pipeline. If a deprojected fit is required, radius, staring angle, and ending angle keywords are adding to the PI spectrum file. The spectrum is also grouped using *grppha* into bins of 20 counts.

  - **wextract.pro** [, *region*, $evt2\_file$, bg_file, *root*, $ciao\_path = ciao\_path$, $mask\_file = mask\_file$]

    Responsible for generating the PI spectrum and the associated weighted ARF and RMF files. The ciao routines used in this process are *dmextract*, $mkacisrmf$ and $mkwarf$.

- **fit_mult_inst.pro** [, $spectra\_dir = spectra\_dir$, */deprojected*, */projected*, */twotemp*, */vmekal*]

  $spectra\_dir = spectra\_dir$ - String variable of entire path to spectra files starting at the working directory.

  /deprojected - Set flag for Xspec model PROJCT×WABS×MEKAL.

  /projected - Set flag for Xspec model WABS×MEKAL.

  /twotemp - Set flag for Xspec model WABS(MEKAL+MEKAL).

/vmekal - Set flag for Xspec model WABS×VMEKAL.

Routines called within *fit_mult_inst.pro*.

- **make_deproj_script.pro**
  Routine called when */deprojected* flag set. Outputs script file projct_wabs_mekal.xcm to be read into Xspec.
- **make_aciscomb_script.pro**
  Routine called when */projected* flag set. Outputs script files wabmekal_aciscomb − ∗.xcm to be read into Xspec. The asterisk represents the multi-spec sequence number.
- **make_twotemp_script.pro**
  Routine called when */twotemp* flag set. Outputs script files wabmekal_tt−∗.xcm to be read into Xspec.
- **make_vmekal_script.pro**
  Routine called when */vmekal* flag set. Outputs script files wabvmekal_aciscomb − ∗.xcm to be read into Xspec.

- Ploting
  - **ab_plot.pro** [, *dir*, */projected*, */deprojected*, */twotemp*]
  - **den_plot.pro** [, *dir*, */projected*, */deprojected*, */twotemp*]
    This routine requires *emiss.pro* be run first.
  - **emiss.pro** [, *nrad*, *spectra_dir* = *spectra_dir*]
    This routine calls the FORTRAN program *deconv.f*.

    nrad - Number of annuli fit.
  - **nh_plot.pro** [, *dir*, */projected*, */deprojected*, */twotemp*]
  - **sb_plot.pro** [, *xc*, *yc*, *ellip*, *pa*, *back*, *backerr*
    This routine calls the routine *calc_sb_image.pro*.

    xc - X-coordinate for X-ray center.
    yc - Y-coordinate for X-ray center.
    ellip - Ellipticity of surface brightness annuli.
    pa - Position angle of surface brightness annuli.

back - Background surface brightness.

backerr - Error on background surface brightness.

- **temp_plot.pro** [, *dir*, */projected*, */deprojected*, */twotemp*]

- **mkmap.pro** [, *cluster*, *obsid*, *dir*, *signo*, */no_merge*, *auto_fit*, */no_reproject*, *fit_param* = *fit_param*]

  cluster - String variable name appended to output files.

  obsid - String array of all working directories for each observation.

  dir - String variable name of directory to be created within the /spectra directory.

  signo - Signal-to-noise target value.

  /no_merge - Set flag if merged event files already exist.

  /auto_fit - Set flag for all map regions to be fit automatically after spectra are extracted. *fit_param* keyword must be set when using this flag.

  /no_reproject - Set flag is event 2 files have already been reprojected to same image coordinates.

  fit_param - String of parameters for Xspec single-temperature fit (WABS × MEKAL). The parameters include column density (nh), temperature (kt), abundance (ab), redshift (z), spectral fit range in keV (lo, hi), and spectral binning (binning).

  Routines called within *mkmap.pro*.

  - WVT routines

    The weighted-Voronoi tessellation (WVT) routine package was developed by Diehl & Statler (2006). The package can be downloaded at Steven Diehl's website.

  - **merge.pro** [, *obsid*, */ptsrc*]

    Must be run if there is no merged level=2 event file. The */ptsrc* flag is not used in *mkmap.pro*.

  - **extract_map.pro**

    The same as *autoext.pro*, but uses the file naming convention required by *mkmap.pro*.

– **mextract_map.pro**
  The *mkmap.pro* version of *mextract.pro*.
– **wextract_map.pro**
  The *mkmap.pro* version of *wextract.pro*.
– **map_fit.pro**
  The *mkmap.pro* version of *fit_mult_inst.pro*.

Appendix B

Co-authored Publications and Future Publications

B.1 MS0735.6+7421

I am one of the co-authors on McNamara et al. (2009). My contribution to this publication was the X-ray analysis of the central cluster emission. My goal was to determine the upper limit on the point source luminosity if one exists.

Future work on MS 0735 include an X-ray analysis of new 500 ks observation of the cluster take by the *Chandra X-ray Observatory*.

B.2 Zwicky 2701

Work presented here in section 5.4.4 is intended for future publication as a part of a project based on a new 100 ks observation of Zw2701 by the *Chandra X-ray Observatory*.

Bibliography

Aalto, S., & Hüttemeister, S. 2000, A&A, 362, 42 38

Abell, G. O., Corwin, H. G., Jr., & Olowin, R. P. 1989, ApJS, 70, 1 8

Allen, S. W., & Fabian, A. C. 1998, MNRAS, 297, L63 4, 51, 63

Allen, S. W., Edge, A. C., Fabian, A. C., Böhringer, H., Crawford, C. S., Ebeling, H., Johnstone, R. M., Naylor, T., & Schwarz, R. A. 1992, MNRAS, 259, 67 8

Allen, S. W., Fabian, A. C., Edge, A. C., Böhringer, H., & White, D. A. 1995, MNRAS, 275, 741 8, 12, 38

Arnaud, K. A. 1996, Astronomical Data Analysis Software and Systems V, 101, 17 42

Ascasibar, Y., & Markevitch, M. 2006, ApJ, 650, 102 16

Barai, P., Martel, H., & Germain, J. 2011, ApJ, 727, 54 62

Benson, A. J. 2005, MNRAS, 358, 551 38

Bildfell, C., Hoekstra, H., Babul, A., & Mahdavi, A. 2008, MNRAS, 389, 1637 7, 63

Bîrzan, L., McNamara, B. R., Nulsen, P. E. J., Carilli, C. L. & Wise, M. W. 2008, ApJ, 686, 859 iii, 3, 32, 35, 36

Bîrzan, L., Rafferty, D. A., McNamara, B. R., Wise, M. W., & Nulsen, P. E. J. 2004, ApJ, 607, 800 3, 6, 32, 52, 93

Böhringer, H., et al. 2001, A&A, 365, L181 22

Böhringer, H., Matsushita, K., Churazov, E., Finoguenov, A., & Ikebe, Y. 2004, A&A, 416, L21 49, 117

Bourdin, H., & Mazzotta, P. 2008, A&A, 479, 307 73

Bower, R. G., Benson, A. J., Malbon, R., Helly, J. C., Frenk, C. S., Baugh, C. M., Cole, S., & Lacey, C. G. 2006, MNRAS, 370, 645 8

Bregman, J. N., Novicki, M. C., Krick, J. E., & Arabadjis, J. S. 2003, ApJ, 597, 399 73

Brüggen, M. 2002, ApJL, 571, L13 41

Brüggen, M., & Kaiser, C. R. 2002, Nature, 418, 301 7, 52, 64

Brüggen, M., Ruszkowski, M., & Hallman, E. 2005, ApJ, 630, 740 7

Buote, D. A. 2000, MNRAS, 311, 176 22, 24, 71

Buote, D. A. 2001, ApJ, 548, 652 22

Burns, J. O., Hallman, E. J., Gantner, B., Motl, P. M., & Norman, M. L. 2008, ApJ, 675, 1125 62

Cappellari, M., & Copin, Y. 2003, MNRAS, 342, 345 44, 53, 73

Cappellaro, E., Evans, R., & Turatto, M. 1999, A&A, 351, 459 49, 117

Cardelli, J. A., Clayton, G. C., & Mathis, J. S. 1989, ApJ, 345, 245 29

Cardiel, N., Gorgas, J., & Aragon-Salamanca, A. 1998, MNRAS, 298, 977 7, 63

Cavagnolo, K. W., Donahue, M., Voit, G. M., & Sun, M. 2008, ApJL, 683, L107 7, 36, 63

Cavagnolo, K. W., McNamara, B. R., Nulsen, P. E. J., et al. 2010, ApJ, 720, 1066 3

Churazov, E., Brüggen, M., Kaiser, C. R., Böhringer, H., & Forman, W. 2001, ApJ, 554, 261 93

Churazov, E., Sunyaev, R., Forman, W., & Böhringer, H. 2002, MNRAS, 332, 729 3, 6

Clarke, T. E., Blanton, E. L., & Sarazin, C. L. 2004, ApJ, 616, 178 12

Clowe, D., Bradač, M., Gonzalez, A. H., et al. 2006, ApJL, 648, L109 1

Crawford, C. S., Edge, A. C., Fabian, A. C., Allen, S. W., Bohringer, H., Ebeling, H., McMahon, R. G., & Voges, W. 1995, MNRAS, 274, 75 7, 63

Crawford, C. S., Allen, S. W., Ebeling, H., Edge, A. C., & Fabian, A. C. 1999, MNRAS, 306, 857 7, 36, 63

Crosthwaite, L. P., Turner, J. L., Hurt, R. L., Levine, D. A., Martin, R. N., & Ho, P. T. P. 2001, AJ, 122, 797 38

Crosthwaite, L. P., Turner, J. L., Buchholz, L., Ho, P. T. P., & Martin, R. N. 2002, AJ, 123, 1892 38

Croton, D. J., Springel, V., White, S. D. M., De Lucia, G., Frenk, C. S., Gao, L., Jenkins, A., Kauffmann, G., Navarro, J. F., & Yoshida, N. 2006, MNRAS, 365, 11 8

Dalla Vecchia, C., Bower, R. G., Theuns, T., Balogh, M. L., Mazzotta, P., & Frenk, C. S. 2004, MNRAS, 355, 995 7

David, L. P., Nulsen, P. E. J., McNamara, B. R., Forman, W., Jones, C., Ponman, T., Robertson, B., & Wise, M. 2001, ApJ, 557, 546 42, 49

David, L. P., & Nulsen, P. E. J. 2008, ApJ, 689, 837 3, 4, 41, 51, 64

Dennis, T. J., & Chandran, B. D. G. 2005, ApJ, 622, 205 7

De Breuck, C., Tang, Y., de Bruyn, A. G., Rottgering, H., & van Breugel, W. 2002, VizieR Online Data Catalog, 8069, 0 35

De Grandi, S., & Molendi, S. 2001, ApJ, 551, 153 4, 22, 41, 51, 63

De Grandi, S., Ettori, S., Longhetti, M., & Molendi, S. 2004, A&A, 419, 7 41, 51, 64

Dickey, J. M., & Lockman, F. J. 1990, ARA&A, 28, 215 16, 44, 53, 71

Diehl, S., & Statler, T. S. 2006, MNRAS, 368, 497 44, 53, 73, 130

Diehl, S., Li, H., Fryer, C. L., & Rafferty, D. 2008, ApJ, 687, 173 52

Dolag, K., Jubelgas, M., Springel, V., Borgani, S., & Rasia, E. 2004, ApJL, 606, L97 7

Donahue, M., Sun, M., O'Dea, C. P., Voit, G. M., & Cavagnolo, K. W. 2007, AJ, 134, 14 7, 63

Dong, R., Rasmussen, J., & Mulchaey, J. S. 2010, ApJ, 712, 883 90

Dunn, R. J. H., Fabian, A. C., & Taylor, G. B. 2005, MNRAS, 364, 1343 40

Dunn, R. J. H., & Fabian, A. C. 2006, MNRAS, 373, 959 3, 6, 32

Dupke, R. A., & White, R. E., III 2000, ApJ, 537, 123 4, 51, 63

Dupke, R., White, R. E., III, & Bregman, J. N. 2007, ApJ, 671, 181 12

Edge, A. C. 2001, MNRAS, 328, 762 2, 22

Edge, A. C., Wilman, R. J., Johnstone, R. M., Crawford, C. S., Fabian, A. C., & Allen, S. W. 2002, MNRAS, 337, 49 7, 63

Edwards, L. O. V., Hudson, M. J., Balogh, M. L., & Smith, R. J. 2007, MNRAS, 379, 100 7, 63

Enßlin, T. A., Biermann, P. L., Klein, U., & Kohle, S. 1998, A&A, 332, 395 29

Enßlin, T. A., & Brüggen, M. 2002, MNRAS, 331, 1011 29

Fabian, A. C. 1994, ARA&A, 32, 277 2, 6, 63

Fabian, A. C., Sanders, J. S., Taylor, G. B., Allen, S. W., Crawford, C. S., Johnstone, R. M., & Iwasawa, K. 2006, MNRAS, 366, 417 26

Fabjan, D., Borgani, S., Tornatore, L., Saro, A., Murante, G., & Dolag, K. 2010, MNRAS, 401, 1670 62

Ferrarese, L., & Merritt, D. 2000, ApJL, 539, L9 8

Frank, J., King, A., & Raine, D. J. 2002, Accretion Power in Astrophysics (Cambridge, UK: Cambridge University Press)

Gaspari, M., Melioli, C., Brighenti, F., & D'Ercole, A. 2011, MNRAS, 411, 349 60

Gebhardt, K., et al. 2000, ApJL, 539, L13 8

Gilfanov, M. R., Syunyaev, R. A., & Churazov, E. M. 1987, Soviet Astronomy Letters, 13, 3 22

Giovannini, G., Tordi, M., & Feretti, L. 1999, New Astronomy, 4, 141 29

Gitti, M., Nulsen, P. E. J., David, L. P., McNamara, B. R., & Wise, M. W. 2011, ApJ, 732, 13 64

Gopal-Krishna, & Wiita, P. J. 2001, ApJL, 560, L115 41, 52, 64

Gopal-Krishna, & Wiita, P. J. 2003, Radio Astronomy at the Fringe, 300, 293 41, 52, 64

Govoni, F., Feretti, L., Giovannini, G., Böhringer, H., Reiprich, T. H., & Murgia, M. 2001, A&A, 376, 803 29

Grevesse, N., & Sauval, A. J. 1998, Space Science Reviews, 85, 161 22, 44, 53, 71

Gu, J., Xu, H., Gu, L., An, T., Wang, Y., Zhang, Z., & Wu, X.-P. 2007, ApJ, 659, 275 41

Häring, N., & Rix, H.-W. 2004, ApJL, 604, L89 8

Heath, D., Krause, M., & Alexander, P. 2007, MNRAS, 374, 787 41

Heinz, S., Brüggen, M., Young, A., & Levesque, E. 2006, MNRAS, 373, L65 7

Hicks, A. K., & Mushotzky, R. 2005, ApJL, 635, L9 3, 7

Holtzman, J. A., et al. 1996, AJ, 112, 416 7

Hu, E. M., Cowie, L. L., & Wang, Z. 1985, ApJS, 59, 447 7

Johnstone, R. M., Fabian, A. C., & Nulsen, P. E. J. 1987, MNRAS, 224, 75 7, 63

Kay, S. T., Thomas, P. A., Jenkins, A., & Pearce, F. R. 2004, MNRAS, 355, 1091 26

Kenney, J. D. P., & Koopmann, R. A. 1999, AJ, 117, 181 37

Kirkpatrick, C. C., Gitti, M., Cavagnolo, K. W., McNamara, B. R., David, L. P., Nulsen, P. E. J., & Wise, M. W. 2009a, ApJL, 707, L69 3, 5, 52, 64, 100, 117

Kirkpatrick, C. C., et al. 2009b, ApJ, 697, 867 5, 53, 71

Kirkpatrick, C. C., McNamara, B. R., & Cavagnolo, K. W. 2011, ApJL, 731, L23 3, 5, 64, 65, 76, 83

Markevitch, M., & Vikhlinin, A. 2007, Phys. Rep., 443, 1 12

McNamara, B. R. 1995, ApJ, 443, 77 49

McNamara, B. R. 1997, Galactic Cluster Cooling Flows, 115, 109 2

McNamara, B. R. 2002, The High Energy Universe at Sharp Focus: Chandra Science, 262, 351 3, 7

McNamara, B. R., Kazemzadeh, F., Rafferty, D. A., et al. 2009, ApJ, 698, 594 119, 132

McNamara, B. R., & Nulsen, P. E. J. 2007, ARA&A, 45, 117 3, 6, 40, 50, 52, 64

McNamara, B. R., & O'Connell, R. W. 1989, AJ, 98, 2018 7, 63

McNamara, B. R., & O'Connell, R. W. 1992, ApJ, 393, 579 32

McNamara, B. R., Rafferty, D. A., Bîrzan, L., et al. 2006, ApJ, 648, 164 117

McNamara, B. R., et al. 2000, ApJL, 534, L135 3, 6, 42

Molendi, S., & Gastaldello, F. 2001, A&A, 375, L14 24, 71

Moll, R., et al. 2007, A&A, 463, 513 52, 64

Morris, R. G., & Fabian, A. C. 2003, MNRAS, 338, 824 22

Morsony, B. J., Heinz, S., Brüggen, M., & Ruszkowski, M. 2010, MNRAS, 407, 1277 60

Mushotzky, R. F., & Loewenstein, M. 1997, ApJL, 481, L63 4, 51, 63

Mushotzky, R., Loewenstein, M., Arnaud, K. A., Tamura, T., Fukazawa, Y., Matsushita, K., Kikuchi, K., & Hatsukade, I. 1996, ApJ, 466, 686 4, 51, 63

Narayan, R., & McClintock, J. E. 2008, New Astron. Rev., 51, 733 62

Navarro, J. F., Frenk, C. S., & White, S. D. M. 1997, ApJ, 490, 493 37

Nulsen, P. E. J., David, L. P., McNamara, B. R., Jones, C., Forman, W. R., & Wise, M. 2002, ApJ, 568, 163 42

Nulsen, P. E. J., McNamara, B. R., Wise, M. W., & David, L. P. 2005, ApJ, 628, 629 42

O'Dea, C. P., et al. 2008, ApJ, 681, 1035 3, 7, 8, 63

Omma, H., Binney, J., Bryan, G., & Slyz, A. 2004, MNRAS, 348, 1105 41, 52, 64

O'Sullivan, E., Giacintucci, S., David, L. P., Vrtilek, J. M., & Raychaudhury, S. 2010, MNRAS, 407, 321 60

O'Sullivan, E., Giacintucci, S., David, L. P., Vrtilek, J. M., & Raychaudhury, S. 2011, MNRAS, 411, 1833 52, 60

Owen, F. N., Eilek, J. A., & Keel, W. C. 1990, ApJ, 362, 449 120

Peletier, R. F., Davies, R. L., Illingworth, G. D., Davis, L. E., & Cawson, M. 1990, AJ, 100, 1091 32

Peterson, J. R., Kahn, S. M., Paerels, F. B. S., Kaastra, J. S., Tamura, T., Bleeker, J. A. M., Ferrigno, C., & Jernigan, J. G. 2003, ApJ, 590, 207 2, 6

Peterson, J. R., & Fabian, A. C. 2006, Phys. Rep., 427, 1 2, 6

Poggianti, B. M. 1997, A&AS, 122, 399 29

Poole, G. B., Babul, A., McCarthy, I. G., Sanderson, A. J. R., & Fardal, M. A. 2008, MNRAS, 391, 1163 7

Pope, E. C. D., Babul, A., Pavlovski, G., Bower, R. G., & Dotter, A. 2010, MNRAS, 406, 2023 52, 60, 64

Rafferty, D. A., McNamara, B. R., Nulsen, P. E. J., & Wise, M. W. 2006, ApJ, 652, 216 3, 6, 7, 32, 36, 52, 55, 63, 65, 69, 83, 90, 95, 119, 122

Rafferty, D. A., McNamara, B. R., & Nulsen, P. E. J. 2008, ApJ, 687, 899 3, 7, 29, 35, 36, 40, 63

Rasera, Y., Lynch, B., Srivastava, K., & Chandran, B. 2008, ApJ, 689, 825 41, 51, 64

Rebusco, P., Churazov, E., Böhringer, H., & Forman, W. 2005, MNRAS, 359, 1041 3, 4, 41, 51, 64

Rebusco, P., Churazov, E., Böhringer, H., & Forman, W. 2006, MNRAS, 372, 1840 3, 4, 41, 51, 64

Reynolds, C. S., Casper, E. A., & Heinz, S. 2008, ApJ, 679, 1181 49, 100

Reynolds, C. S., Heinz, S., & Begelman, M. C. 2002, MNRAS, 332, 271 7

Roediger, E., Brüggen, M., Rebusco, P., Böhringer, H., & Churazov, E. 2007, MNRAS, 375, 15 41, 52, 64

Roediger, E., Brüggen, M., Simionescu, A., Böhringer, H., Churazov, E., & Forman, W. R. 2010, arXiv:1007.4209 62

Russell, H. R., Fabian, A. C., Sanders, J. S., Johnstone, R. M., Blundell, K. M., Brandt, W. N., & Crawford, C. S. 2010, MNRAS, 402, 1561 62

Ruszkowski, M., Brüggen, M., & Begelman, M. C. 2004, ApJ, 611, 158 7

Ruszkowski, M., Brüggen, M., & Begelman, M. C. 2004, ApJ, 615, 675 7

Salomé, P., & Combes, F. 2003, A&A, 412, 657 7, 63

Sanders, J. S., & Fabian, A. C. 2002, MNRAS, 331, 273 12, 22

Sanders, J. S., Fabian, A. C., Allen, S. W., Morris, R. G., Graham, J., & Johnstone, R. M. 2008, MNRAS, 385, 1186 6

Sanders, J. S., Fabian, A. C., Allen, S. W., & Schmidt, R. W. 2004, MNRAS, 349, 952 41

Sarazin, C. L. 1988, X-ray Emissions from Clusters of Galaxies (Cambridge: Cambridge University Press) 1

Sarazin, C. L. 2003, Physics of Plasmas, 10, 1992 2

Schmidt, R. W., Fabian, A. C., & Sanders, J. S. 2002, MNRAS, 337, 71 22

Scoville, N. Z., & Sanders, D. B. 1987, Interstellar Processes, 134, 21 38

Sharma, P., Chandran, B. D. G., Quataert, E., & Parrish, I. J. 2009, ApJ, 699, 348 52

Simionescu, A., Werner, N., Böhringer, H., Kaastra, J. S., Finoguenov, A., Brüggen, M., & Nulsen, P. E. J. 2009, A&A, 493, 409 3, 41, 47, 49, 52, 64

Simionescu, A., Werner, N., Finoguenov, A., Böhringer, H., & Brüggen, M. 2008, A&A, 482, 97 3, 41, 52, 64

Soker, N. 2008, ApJL, 684, L5 7, 63

Tamura, T., Kaastra, J. S., den Herder, J. W. A., Bleeker, J. A. M., & Peterson, J. R. 2004, A&A, 420, 135 41, 51, 64

Tittley, E. R., & Henriksen, M. 2005, ApJ, 618, 227 12

Vernaleo, J. C., & Reynolds, C. S. 2006, ApJ, 645, 83 7

Voigt, L. M., & Fabian, A. C. 2004, MNRAS, 347, 1130 3, 7

Voit, G. M., Bryan, G. L., Balogh, M. L., & Bower, R. G. 2002, ApJ, 576, 601 26

Voit, G. M., & Donahue, M. 2005, ApJ, 634, 955 26

Voit, G. M., Cavagnolo, K. W., Donahue, M., Rafferty, D. A., McNamara, B. R., & Nulsen, P. E. J. 2008, ApJL, 681, L5 7, 36, 63

Vollmer, B., Braine, J., Balkowski, C., Cayatte, V., & Duschl, W. J. 2001, A&A, 374, 824 37

Wilman, R. J., Edge, A. C., & Swinbank, A. M. 2006, MNRAS, 371, 93 8, 9, 22, 37

Wilman, R. J., Edge, A. C., & Swinbank, A. M. 2009, arXiv:0902.4720 36

Wise, M. W., McNamara, B. R., & Murray, S. S. 2004, ApJ, 601, 184 12, 16

Wise, M. W., McNamara, B. R., Nulsen, P. E. J., Houck, J. C., & David, L. P. 2007, ApJ, 659, 1153 xiii, 42, 43, 45, 50, 58

Zakamska, N. L., & Narayan, R. 2003, ApJ, 582, 162

3, 7